HYDROTHERMAL SYNTHESIS OF RARE EARTH IONS DOPED $LaBO_3$ and $GdBO_3$ ORTHOBORATES AND THEIR PHOTOLUMINESCENCE PROPERTIES

A THESIS SUBMITTED TO

THE GRADUATE SCHOOL OF NATURAL AND APPLIED SCIENCES

OF

MIDDLE EAST TECHNICAL UNIVERSITY

BY

SAEED VAHED QARAMALEKI

IN PARTIAL FULFILLMENT OF THE REQUIREMENTS

FOR

THE DEGREE OF MASTER OF SCIENCE

IN

CHEMICAL ENGINEERING

AUGUST 2016

Approval of the thesis:

HYDROTHERMAL SYNTHESIS OF RARE EARTH IONS DOPED *$LaBO_3$* and *$GdBO_3$* ORTHOBORATES AND THEIR PHOTOLUMINESCENCE PROPERTIES

Submitted by **SAEED VAHED QARAMALEKI** in partial fulfillment of the requirements for the degree of **Master of Science in Chemical Engineering Department, Middle East Technical University** by,

Prof. Dr. Gülbin Dural Ünver
Dean, Graduate School of **Natural and Applied Sciences** _____

Prof. Dr. Halil Kalıpçılar
Head of Department, **Chemical Engineering** _____

Prof. Dr. Deniz Üner
Supervisor, **Chemical Engineering Dept., METU** _____

Prof. Dr. Ayşen Yılmaz
Co-supervisor, **Chemistry Dept., METU** _____

Examining Committee Members:

Prof. Dr. Göknur Bayram
Chemical Engineering Dept., METU _____

Prof. Dr. Deniz Üner
Chemical Engineering Dept., METU _____

Prof. Dr. Ayşen Yılmaz
Chemistry Dept., METU _____

Assoc. Prof. Dr. Fatih Danışman
Chemistry Dept., METU _____

Prof. Dr. Leyla Tatar Yıldırım
Physics Engineering Dept., Hacettepe Uni. _____

Date: 12.08.2016

I hereby declare that all information in this document has been obtained and presented in accordance with academic rules and ethical conduct. I also declare that, as required by these rules and conduct, I have fully cited and referenced all material and results that are not original to this work.

Name, Last name: Saeed Vahed Qaramaleki

Signature:

ABSTRACT

HYDROTHERMAL SYNTHESIS OF RARE EARTH IONS DOPED *$LaBO_3$* and *$GdBO_3$* ORTHOBORATES AND THEIR PHOTOLUMINESCENCE PROPERTIES

Saeed Vahed Qaramaleki

M. Sc., Department of Chemical Engineering

Supervisor: Prof. Deniz Üner

Co-supervisor: Prof. Ayşen Yılmaz

August 2016, 108 pages

Within the scope of this research project three different rare earth elements such as Dysprosium (Dy), Terbium (Tb) and Samarium (Sm) have been doped inside two different host material namely $LaBO_3$ and $GdBO_3$ orthoborates. The preparation of materials were conducted at low temperature by hydrothermal synthesis method. After preparing the solution of precursors it has been placed into a well-sealed Teflon lined autoclave and maintained in 200 ˚C inside a furnace for 24 hours. The obtained powder was then washed with deionized water and dried at 80 ˚C.

Structural and optical properties of as-prepared materials were investigated by using various characterization techniques. In order to study the phase composition and crystal structure of materials X-ray diffraction (XRD) method was applied. IR spectroscopy of produced materials has been implemented in an effort to investigate the vibrational modes of anionic groups. Moreover, by conducting FAR-IR spectroscopy low frequency vibrational modes such as metal-metal bonds and metal-oxygen bonds have been studied. Morphology and homogeneity of powder samples were analyzed by using scanning electronic microscopy (SEM) method. Luminescent properties of produced materials were scrutinized by fluorescence spectroscopy.

Based on the results obtained through various characterization analysis, it has been found that after certain concentration, doping of rare Earth elements inside the $LaBO_3$ orthoborates would cause serious disruption to the crystal structure of the host material .This concentrations for Dy, Tb and Sm doping are 5%, 7% and 10 % respectively. Nonetheless, when the $GdBO_3$ was used as host material, doping with different amount of rare earth elements in the range of 2.5-15% has not resulted in remarkable change on the structure of host material. The IR analysis of synthesized materials revealed the different vibrational modes of anionic structure. Samples with $LaBO_3$ as the host material exhibit vibrational modes which could have been assigned to trigonal planar borate structure (BO_3^{3-}). On the other hand, when the $GdBO_3$ were used as the host, IR spectroscopy has shown the characteristic absorption bands of tetrahedral ring structure of borate ($B_3O_9^{9-}$). The fluorescence spectroscopy has revealed the optimum concentration of doping for each of $LaBO_3$ and $GdBO_3$ doped with Dy, Tb and Sm, respectively. The optimum concentration for $LaBO_3$ doped with Dy, Tb and Sm are 5, 7 and 5%, respectively. In the case of Dy, Tb and Sm doped $GdBO_3$ samples the best PL performance was obtinaed with 7.5, 10 and 5% concentrations, respectively. In order to specify the perceived color of prepared materials color chromaticity coordinates of each sample have been calculated by a MATLAB coded program and photoluminescence data obtained from fluorescence spectroscopy. It has been observed that Dy doped samples give yellow color, Tb doped samples give green color and Sm doped samples give orange color.

Keywords: Hydrothermal synthesis, Lanthanide orthoborate, photoluminescence, phosphor, color chromaticity diagram

ÖZ

NADİR TOPRAK İYONLARI İLE KATKILI *$LaBO_3$* VE *$GdBO_3$* ORTOBORATLARIN HİDROTERMAL SENTEZİ, KARAKTERİZASYONU VE LÜMİNESANS ÖZELLİKLERİNİN ARAŞTIRILMASI

Vahed Qaramaleki Saeed

Yüksek lisans kimya mühendisliği

Tez yöneticisi: Prof. Dr. Deniz Üner

Ortak tez yöneticisi: Prof. Dr. Ayşen Yılmaz

Ağustos 2016, 108 sayfa

Bu araştırma kapsamında çeşitli nadir toprak elementleri (Dy, Tb ve Sm) $LaBO_3$ ve $GdBO_3$ ana yapıları içine katkılanmış ve onların yapısal ve lüminesans özellikleri incelenmiştir. Bu çalışmada malzemelerin hazırlanmasında hidrotermal snetez tekniği kullanılmıştır. Hidrotermal yöntem daha düşük sıcaklıkta sentez yapma imkânı sunmuştur. Ayrıca hidrotermal sentez kullanılarak parçacıkların daha homojen ve düzgün şekilli morfolojiye sahip olmaları sağlanmıştır. Sentez sürecinde başlangıç maddelerden hazırlanan çözelti iç yüzü Teflonla kaplı ve çok dikkatlice yalıtılmış bir otoklavın içine aktarılmış ve 200˚C de 24 saat boyunca ısıtılmıştır. Elde edilen toz hâlindeki ürün daha sonra deiyonize suyla yıkanmış ve 80˚C de kurutulmuştur.

Hazırlanan örnekler daha sonra çeşitli yöntemler kullanılarak karakterize edilmiştir. Üretilen maddelerin yapısal ve kristal faz bileşimi X-Işını toz kırınımı tekniği kullanılarak belirlenmiştir. IR analizi üretilen malzemelerin anyonik gruplarının bağ yapısı ve bantlarını aydınlatmak amacıyla gerçekleştirilmiştir. Sentezlenen numunelerin morfolojik yapısı taramalı elektron mikroskopu (SEM) kullanılarak

irdelenmiştir. Düşük frekanslara sahip bağları tanımlayabilmek için FAR-IR yöntemi kullanılmıştır. Ayrıca örneklerin fotolüminesans özellikleri floresan spektroskopi aracılığı ile tespit edilmeye çalışılmıştır.

Çeşitli karakterizasyon süreçlerinden elde edilen bilgilere dayanarak $LaBO_3$ ana yapısının belli bir miktar katkılamadan sonra kristal yapısının bozulduğu anlaşılmıştır. Bu miktar Dy katkılı $LaBO_3$ için %5, Tb katkılı $LaBO_3$ için %7, Sm katkılı $LaBO_3$ için %10 olarak belirlenmiştir. Ancak katkılama işlemi $GdBO_3$ ana yapısında gerçekleştiği zaman malzemenin kristal yapısı korunmuş ve belirgin bir değişim gözlemlenmemiştir. IR analizi hazırlanan numunelerin anyonik borat yapılarının farklı olduğu gerçeğini ortaya koymuştur. Dy, Tb ve Sm elementleriyle katkılanan $LaBO_3$ ana yapıların borat bileşiği düzlemsel BO_3^{3-} gruplarından oluştuğu IR analizi yardımı ile tespit edilmiştir. Diğer yandan Dy, Tb ve Sm katkılı $GdBO_3$ örneklerinde borat yapısı $B_3O_9^{9-}$ gruplarından oluştuğu tespit edilmiştir. FAR-IR tekniği sayesinde sentezlenen örneklerin metal-oksijen bağları ve yapıları incelenmiştir. Yapılan analizler sonucu $LaBO_3$ ve $GdBO_3$ ana yapılı malzemelerin metal-oksijen yapıları farklı olduğu gerçeği ortaya çıkmıştır. Ayrıca bu yöntemle katkılanan elementin boşluklara mı yerleştiği yoksa La ve Gd ile yer mi değiştirdiği irdelenmeğe çalışılmıştır. Taramalı elektron mikroskopu (SEM) üretilen malzemelerin morfolojik özelliklerini ve parçacıkların şeklini ortaya koymuştur. Üretilen $LaBO_3$ örnekler bir araya toplanmış eğirtmeç halinde gözlemlenmektedirler. $GdBO_3$ örnekler ise karnıbahar gibi şekle sahiptirler. Çeşitli miktarlarla katkılanan $LaBO_3$ ve $GdBO_3$ örneklerin en uygun katkılama miktarları foto lüminesans ölçümleri ile belirlenmiştir. Bu bağlamda Dy katkılı $LaBO_3$ için %5, Tb katkılı $LaBO_3$ için %7, Sm katkılı $LaBO_3$ için %5, Dy katkılı $GdBO_3$ için %7.5, Tb katkılı $GdBO_3$ için %10 ve Sm katkılı $GdBO_3$ için %5 en iyi katkılama oranları olarak tesbit edilmiştir. Son olarak elde edilen numunelerin renk tespiti amacıyla MATLAB ile kodlanmış program kullanılarak CIE hesapları yapılmıştır. Bu hesaplar yola çıkarak Dy katkılı örneklerin sarı, Tb katkılı örneklerin yeşil ve Sm katkılı örneklerin turuncu renge sahip oldukları anlaşılmıştır.

This thesis is devoted to my parents,

Maryam and Akbar Vahed Qaramaleki

For their endless love, patience and encouragement.

ACKNOWLEDGEMENTS

I would first like to thank my thesis advisors Prof. Dr. Ayşen Yılmaz and Prof. Dr. Deniz Üner. The door to Prof. Yılmaz and Prof. Üner office was always open whenever I ran into a trouble spot or had a question about my research or writing.

I would like to express my sincere thanks to Prof. Okan Esentürk and Prof. Ahmet M. Önal for their assistance by letting me operate their laboratory equipment during the experimental stages of the thesis.

I wish to express my thanks to my colleagues; Gencay Çelik, Metehan Severoğlu, Zeynep Seda Eren, Ali Farid and Ceren Abacı for their assistance and guidance during this research.

Finally, I must express my very profound gratitude to my parents for providing me with unfailing support and continuous encouragement throughout my years of study and through the process of researching and writing this thesis. This accomplishment would not have been possible without them. Thank you.

TABLE OF CONTENTS

ABSTRACT v

ÖZ vii

ACKNOWLEDGEMENTS x

TABLE OF CONTENTS xi

LIST OF TABLES xv

LIST OF FIGURES xvii

CHAPTERS 1

1. INTRODUCTION 1

1.1 Phosphors Terminology 1

1.2 Past and present of phosphor research 2

1.3 Application of phosphors 3

1.4 Fundamental Mechanisms of Photoluminescence 5

1.4.1 Radiative Transition 6

1.4.2 Nonradiative Transition 8

1.4.3 Cross-relaxation 9

1.4.4 Features of Rare Earth (RE) Ions with regards to Luminescence 10

1.4.5 Discrete $\boldsymbol{f-f}$ Transition 11

1.4.6 Electronic Configuration 12

1.4.7 Selection Rule 15

1.4.8 Photoluminescence properties of Dysprosium (Dy) 15

1.4.9 Photoluminescence properties of Terbium (Tb) 16
1.4.10 Photoluminescence properties of Samarium (Sm) 17
1.5 Crystal structure of Rare-Earth Orthoborates 18
1.5.1 $LaBO_3$ 20
1.5.2 $GdBO_3$ 22
1.6 Synthesis Method 24
1.6.1 Hydrothermal Synthesis 26
1.7 Objective 28
2. MATERIALS AND METHODS 29
2.1 Materials 29
2.2 Instrumentation 30
2.2.1 Powder X-Ray Diffraction (XRD) 30
2.2.2 Fourier - Transform Infra - Red Spectroscopy (FTIR) 30
2.2.3 Far-IR Spectroscopy 30
2.2.4 Scanning Electron Microscope (SEM) 31
2.2.5 Photoluminescence measurement 31
2.3 Synthesis of Dy, Tb and Sm doped $LaBO_3$ and $GdBO_3$ 31
2.3.1 Synthesis and assembly mechanism of Lanthanum Orthoborates 36
2.4 CIE colorimetric system 37
3. RESULT AND DISCUSSION 39
3.1 Powder X-Ray diffraction 39
3.1.1 XRD results of Dy, Tb and Sm doped LaBO3 39
3.1.2 XRD results of Dy, Tb and Sm doped $GdBO_3$ 42
3.2 FT-IR 45
3.2.1 FT-IR results of Dy, Tb and Sm doped $LaBO_3$ 45

3.2.2 FT-IR results of Dy, Tb and Sm doped $GdBO_3$ 48
3.3 FAR-IR 51
3.3.1 FAR-IR results of Dy, Tb and Sm doped $LaBO_3$ 51
3.3.2 FAR-IR results of Dy, Tb and Sm doped $GdBO_3$ 54
3.4 Scanning Electron Microscopy (SEM) and EDX analysis 57
3.4.1 SEM and EDX results of Dy, Tb and Sm doped $LaBO_3$ 57
3.4.2 SEM and EDX results of Dy, Tb and Sm doped $GdBO_3$ 63
3.5- Photoluminescence analysis 69
3.5.1 Photoluminescence results of Dy, Tb and Sm doped $LaBO_3$ 69
3.5.2 Photoluminescence results of Dy, Tb and Sm doped $GdBO_3$ 76
4. CONCLUSION 83
REFERENCES 87
APPENDICES 97
APPENDIX A 97
Far infrared spectroscopy of La_2O_3 and Gd_2O_3 97
APPENDIX B 99
XRD results of samples doped with Dy, Tb and Sm in high concentration 99
APPENDIX C 103
Dy doped $LaBO_3$ 103
Tb doped $LaBO_3$ 104
Sm doped $LaBO_3$ 105
Dy doped $GdBO_3$ 106
Tb doped $GdBO_3$ 107
Sm doped $GdBO_3$ 108

LIST OF TABLES

TABLES

Table 1: Electronic Configurations of Rare-Earth Ions in the Ground State [2]. 14
Table 2: Global B_2O_3 stockpile. 19
Table 3: List of the materials, their application and labels 29
Table 4: Calculation results of Dy doped $LaBO_3$ 34
Table 5: Calculation results of Dy doped $GdBO_3$ 34
Table 6: Calculation results of Tb doped $LaBO_3$ 34
Table 7: Calculation results of Tb doped $GdBO_3$ 35
Table 8: Calculation results of Sm doped $LaBO_3$ 35
Table 9: Calculation results of Sm doped $GdBO_3$ 35

LIST OF FIGURES

FIGURES

Figure 1. Different applications of phosphorous materials [2]. 4
Figure 2. Schematic diagram showing (a) direct excitation of the activator and (b) indirect excitation followed by energy transfer from the sensitizer or host to the activator [4]. 5
Figure 3. Radiative transition of a luminescent center based on the configurational coordinate model [6]. 7
Figure 4. Different type of non-radiative transition of luminescent center based on the configurational coordinate model [6]. 8
Figure 5. Illustration of cross-relaxation between same or different ions [8]. 10
Figure 6. Dieke Diagram of rare Earth ions [9]. 12
Figure 7. Energy level Diagram of Dy^{3+} ion [11]. 16
Figure 8. Energy level Diagram of Tb^{3+} ion [17]. 17
Figure 9. Energy level Diagram of Sm^{3+} ion [18]. 18
Figure 10. The crystal structure of $LaBO_3$ (Blacks: La atoms, Blues: B atoms, ... 21
Figure 11. Planar BO_3 [38]. 22
Figure 12. Crystal structure of $GdBO_3$ (Blacks: Gd atoms, Blues: B atoms, Reds: O atoms) [38]. 23
Figure 13. Structural sketch map of $B_3O_9^{9-}$ ion [42]. 23
Figure 14. sketch of an autoclave [69]. 27
Figure 15. Synthesis route of Dy, Tb and Sm doped $LaBO_3$ and $GdBO_3$ 33
Figure 16. Self-assembly mechanism of growing crystals [46]. 37
Figure 17. CIE Chromaticity Diagram [72]. 38

Figure 18. X-ray Diffraction pattern of undoped and Dy doped $LaBO_3$ orthoborates. 40
Figure 19. X-ray Diffraction pattern of undoped and Tb doped $LaBO_3$ orthoborates. 41
Figure 20. X-ray Diffraction pattern of undoped and Sm doped $LaBO_3$ orthoborates. 42
Figure 21. X-ray Diffraction pattern of undoped and Dy doped $GdBO_3$ orthoborates. 43
Figure 22. X-ray Diffraction pattern of undoped and Tb doped $GdBO_3$ orthoborates. 44
Figure 23. X-ray Diffraction pattern of undoped and Sm doped $GdBO_3$ orthoborates. 45
Figure 24. ATR-IR spectra of undoped and Dy doped $LaBO_3$ orthoborates. 46
Figure 25. ATR-IR spectra of undoped and Tb doped LaBO3 orthoborates. 47
Figure 26. ATR-IR spectra of undoped and Sm doped LaBO3 orthoborates 48
Figure 27. ATR-IR spectra of undoped and Dy doped $GdBO_3$ orthoborates. 49
Figure 28. ATR-IR spectra of undoped and Tb doped $GdBO_3$ orthoborates. 50
Figure 29. ATR-IR spectra of undoped and Sm doped $GdBO_3$ orthoborates. 51
Figure 30. FAR-IR spectra of undoped and Dy doped $LaBO_3$ orthoborates. 52
Figure 31. FAR-IR spectra of undoped and Tb doped LaBO3 orthoborates. 53
Figure 32. FAR-IR spectra of undoped and Sm doped $LaBO_3$ orthoborates. 54
Figure 33. FAR-IR spectra of undoped and Dy doped $GdBO_3$ orthoborates. 55
Figure 34. FAR-IR spectra of undoped and Tb doped $GdBO_3$ orthoborates. 56
Figure 35. FAR-IR spectra of undoped and Sm doped $GdBO_3$ orthoborates. 57
Figure 36. SEM images of a) undoped $LaBO_3$, b) 5% Dy doped $LaBO_3$, c) 10% Dy doped $LaBO_3$. 58
Figure 37. EDX spectra of a) undoped $LaBO_3$, b) 5% Dy doped $LaBO_3$, c) 10% Dy doped $LaBO_3$. 59
Figure 38. SEM images of a) 5% Tb doped $LaBO_3$, b) 7.5% Tb doped $LaBO_3$,c) 15% Tb doped $LaBO_3$ 60

Figure 39. EDX spectra of a) 5% Tb doped $LaBO_3$, b) 7.5% Tb doped $LaBO_3$, c) 15% Tb doped $LaBO_3$. 61
Figure 40. SEM images of a) 5% Sm doped $LaBO_3$, b) 7.5% Sm doped $LaBO_3$, c) 10% Sm doped $LaBO_3$. 62
Figure 41. EDX spectra of a) 5% Sm doped $LaBO_3$, b) 7.5% Sm doped $LaBO_3$, c) 10% Sm doped $LaBO_3$. 63
Figure 42. SEM images of a) undoped $GdBO_3$, b) 5% Dy doped $GdBO_3$, c) 7.5% Dy doped $GdBO_3$. 64
Figure 43. EDX spectra of a) undoped $GdBO_3$, b) 5% Dy doped $GdBO_3$, c) 7.5% Dy doped $GdBO_3$. 65
Figure 44. SEM images of a) 7.5% Tb doped $GdBO_3$, b) 10% Tb doped $GdBO_3$, c) 12.5% Tb doped $GdBO_3$. 66
Figure 45. EDX spectra of a) 7.5% Tb doped $GdBO_3$, b) 10% Tb doped $GdBO_3$, c) 12.5% Tb doped $GdBO_3$. 67
Figure 46. SEM images of a) 2.5% Sm doped $GdBO_3$, b) 5% Sm doped $GdBO_3$, c) 7.5% Sm doped $GdBO_3$. 68
Figure 47. EDX spectra of a) 2.5% Sm doped $GdBO_3$, b) 5% Sm doped $GdBO_3$, c) 7.5% Sm doped $GdBO_3$. 69
Figure 48. Photoluminescnce measurment of Dy doped $LaBO_3$ samples. 71
Figure 49. CIE calculation of 5% Dy doped $LaBO_3$ sample. 72
Figure 50. Photoluminescnce measurment of Tb doped $LaBO_3$ samples. 73
Figure 51. CIE calculation of 7% Tb doped $LaBO_3$ sample. 74
Figure 52. Photoluminescnce measurment of Sm doped $LaBO_3$ samples. 75
Figure 53. CIE calculation of 5% Sm doped $LaBO_3$ sample. 76
Figure 54. Photoluminescnce measurment of Dy doped $GdBO_3$ samples. 77
Figure 55. CIE calculation of 7.5% Dy doped $GdBO_3$ sample. 78
Figure 56. Photoluminescnce measurment of Tb doped $GdBO_3$ samples. 79
Figure 57. CIE calculation of 10% Tb doped $GdBO_3$ sample 80
Figure 58. Photoluminescnce measurment of Sm doped $GdBO_3$ samples. 81
Figure 59. CIE calculation of 5% Sm doped $GdBO_3$ sample. 82

CHAPTER 1

INTRODUCTION

1.1 Phosphors Terminology

At the beginning it would be helpful to elucidate the origin and meaning of the term "phosphor", which from its' first invention in early 17^{th} century, has retained its meaning. According to an anecdote, Vincentinus Casciarolo of Bologna, who was an alchemist desperately struggling to convert stones to valuable metals, one day found a shiny and heavy crystal rock in a volcano. He heated the stone with the hope that it would be turned into a precious material. Although his efforts floundered to do so, he ended up with a stone which emitted a red light after being exposed to sunlight. Today we know that that stone must have been Barite ($BaSO_4$) which after sintering produces BaS. This material nowadays is used as host matrix for novel phosphors [1].

Subsequent to this finding, lots of similar reports related to those light-emitting rocks started to come from across the Europe. The stones called "phosphors", the Greek equivalent for "light bearer", traced back to Greek mythology of embodiment of Venus. The term phosphorescence is a derivative of phosphor. It means a continuous flux of light coming from a material after stopping the exciting light source.

Fluorescence and phosphorescence are two words which raised lots of controversial debates over first half of 20^{th} century. Most of the arguments were focused on the duration of light emission after excitation termination and on the effect of temperature on light emission. However later researches have proved that those discussions were baseless.

Today, fluorescence is used to refer to light emission which is concurrent with excitation radiation. On the other hand, phosphorescence is used to denote a human-eye detectable emission which occurs after cessation of exciting radiation source. It is worthy of attention that these definitions are only employed to inorganic materials.

The term luminescence which is a derivative of Latin word for light, lumen, is comprised of both phosphorescence and fluorescence. Presently, it can be defined as the light which is given off as a result of energy relaxation of substance that is excited by any external energy source. This light subsumes visible range of electromagnetic wave spectrum of 400 to 700 nm. In addition, near-ultraviolet and near-infrared region could be included.

There is no a rigid and clear definition for word phosphor and it varies according to user will. Specifically, it could be used to refer to inorganic phosphors synthesized in powder form intended to be used in practical applications. Therefore, thin films, single crystals and organic materials with luminescence properties are rarely considered as phosphors [2].

1.2 Past and present of phosphor research

The history of scientific research and synthesis of phosphors can be traced back to more than 150 years ago, when a French chemist, Theodore Sidot, produced a Zinc Sulfide-type phosphor for the first time, in 1866. Pervasive efforts on phosphor research of German scientist and Nobel Prize winner of physics in 1905, Philip E.A. Lenard, led to striking achievements. Lenard and his colleagues produced various kind of phosphor and studied their luminescence properties including phosphors based on sulfides, selenides.

Lenard research group is known for development of a synthesis method which features inserting metallic luminescent activators into the host material by firing. They used both heavy metal ions and rare earth ions in those compounds to bring in luminescent feature. Alkaline chalcogenide phosphors produced by this group are called Lenard phosphors.

The research conducted by R. W. Pohl and colleagues in Germany during 1920's and 1930's, helped to form the pillars of modern-day luminescence physics. By preparing single-crystals of Tl^+ activated alkali halide phosphors and comprehensive study of their spectroscopy, Pohl in corporation with F. Seitz from USA, finally could acquaint coordinate model of luminescent centers which is used to explain the mechanism of luminescence [3].

Two significant developments paved the way for dramatic evolution in phosphor research after World War II. The First was progresses in solid-state physics and semiconductors, in particular. The Second was the interpretation of solids' optical spectroscopy, especially those of rare earth ions and transition metal ions.

Studies related to the phosphors is a complex field which make it a necessity to combine several fields of science and technology. Preparation and mass production of commercial phosphors require deep knowledge of inorganic chemistry and chemical engineering. Solid-state physics is crucial in explaining luminescence mechanism. Electronics, illuminating and imaging engineering are also involved in this field due to vast usage of produced phosphors in lighting, display screens and detector sensors. Therefore, as mentioned above the research on phosphors could be referred to as a fusion of different disciplinary methods and techniques [2].

Currenty, most of the efforts in this field has been directed toward developing phosphors with better optical and chemical properties such as low energy consumption, high chemical stability, low toxcicity and high color quality in the term of color rendering index (CRI), correlated color temperature (CCT) and Commission Internationale de l'Eclairage (CIE) chromaticity coordinates.

1.3 Application of phosphors

Phosphors have a wide range of usage encompassing large and relatively new area of electronic display screens such as plasma displays and field emission displays, lighting in the form of white light emitting diodes and other classic fluorescent lamps and finally detector systems including scintillators and X-ray screens. **Figure 1** presents

the list of phosphors based on the way they are exited. This table recapitulates the phosphordevices according to their application method of phosphor materials.

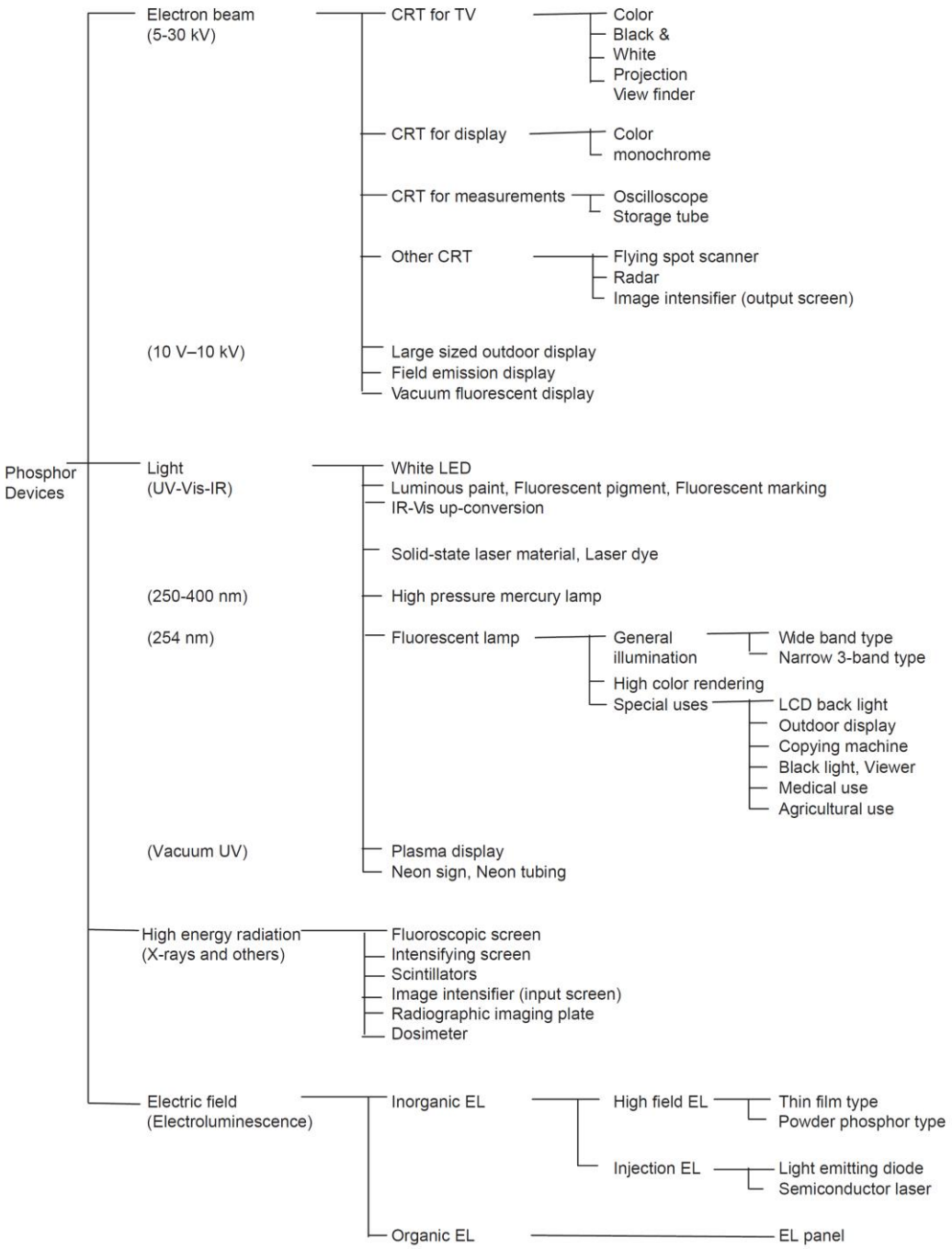

Figure 1. Different applications of phosphorous materials [2].

1.4 Fundamental Mechanisms of Photoluminescence

Luminescence phenomena of phosphors typically comprise of two reverse processes: Excitation and Emission. There are various types of energies which can be used in excitation procedure of phosphors and depending on these energy types, there are different names assigned. In Photoluminescence (PL) photons (often UV and near UV) are used to excite the phosphor. In Cathodoluminescence (CL), excitation occurs by means of highly energetic electrons. In Electroluminescence (EL), electronic voltage is used. When chemical reaction produces the energy needed for exciting the material, it is called Chemiluminescence. Emission is the process of releasing energy in the form of photons. **Figure 2** shows a schematic explanation of processes involved in the Photoluminescence procedure of a typical inorganic phosphor.

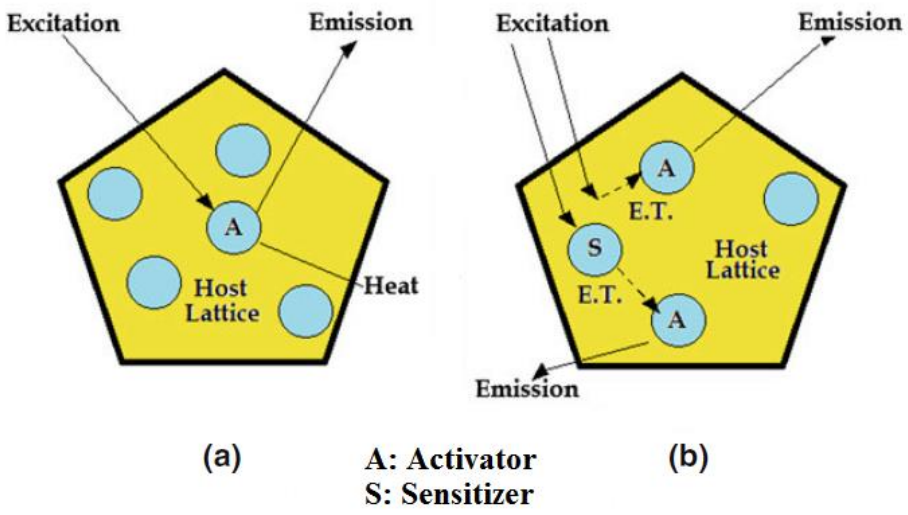

Figure 2. Schematic diagram showing (a) direct excitation of the activator and (b) indirect excitation followed by energy transfer from the sensitizer or host to the activator [4].

Generally, phosphors are constituted of two parts: the first is host or matrix which is a transparent microcrystalline with respect to UV light. The Second part is a deliberately dispersed impurity atoms inside the host material which is called the activator.

Commonly the color of emitted light is tunable by using an appropriate activator without any need to change the host. Nonetheless spectral position of emission of activator ions is deeply influenced by their chemical environment. This is especially the case with rare earth ions.

Although it is possible to excite an activator (luminescent center) inside the bulk material directly by the means of its' own optical absorption (**Figure 2**, a), in most cases due to forbidden optical transitions, activators exhibit poor optical energy absorption. There are two ways to tackle this problem. The energy required to excite luminescence effect could be absorbed by the host lattice (band absorption) and transferred to the impurity ions (**Figure 2**, b) which in the case of delivering desired emission are called activators. This energy transfer mechanism is an effective way of producing highly enhanced phosphors. Another method to overcome the weak absorption, is to introduce a second kind of impurity, capable of absorbing external energy and passing it on to the activator. This kind of atoms are called sensitizers. Transition metals are among the highly utilized metals in order to improve the luminescent properties of phosphors and research aimed at their usage in nanoscale inorganic phosphors have yielded promising results [5].

The incoming energy conveyed to activator atoms through either host lattice or sensitizer ions, makes the electrons of the activator to rise to an excited state. Returning to the ground state occurs in various forms which will be elucidated in upcoming sections.

1.4.1 Radiative Transition

Radiative transition from excited state to the ground state is one of the probabilities which is responsible of visible light emission of luminescent center. The luminescent efficiency of a phosphor can be measured by its' quantum yield which can be defined as the ratio of number of emitted photons to the number of absorbed photons. Alongside radiative transitions there are several parallel processes such as radiative transfer to another ion, multiphonon relaxation and energy transfer among the ions of same kind (cross-relaxation) or different ions, which contend with radiative transition.

Figure 3 illustrates the proess of radiative transition based on the configurational coordinate model. The offset between the parabolas of excited and ground state is based on assumption. The parabolas represent the potential energy as function of distance between to ions. Following the excitation the electron of the activator atoms ends up in a higher energy level composed of a wide optical band. In the excited state the electron resides in the high vibrational level. Subsequently the electron releases its surplus energy to the environment and reaches the lowest level of exited state. This process involves nonradiative relaxation of energy.

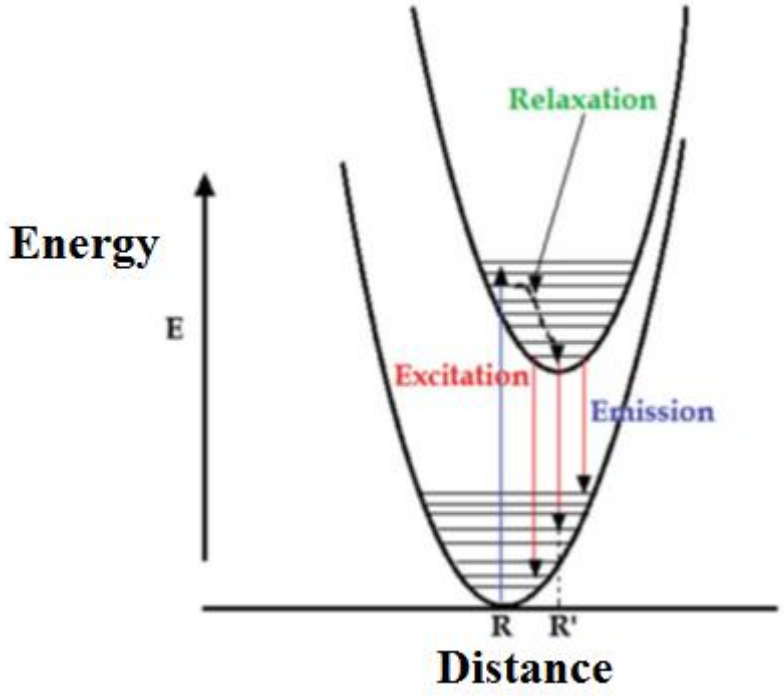

Figure 3. Radiative transition of a luminescent center based on the configurational coordinate model [6].

Electrons from the lowest level of excited state revert to the ground state through photon emission. Energy difference amidst the excited band peak and that of emission band is called Stokes shift [7]. The radiative transfer consists of absorption of the emitted light from a donor molecule or ion by the acceptor species. In order that such

a transfer takes place, the emission of the donor has to coincide with the absorption of the acceptor. The radiative transfer can be increased considerably by designing a proper geometry.

1.4.2 Nonradiative Transition

Some part of external energy, which is used to excite the luminescent material, depletes in the form of energies vanished to the crystal lattice rather than radiative emission of photons. In order to increase desired process of radiative relaxation, restraining of those nonradiative process bears extremely high importance. **Figure 4** shows the configurational coordinate diagram of localized luminescent center which provides a viable explanation of physical phenomena involved in the nonradiative transitions. **Figure 4**a represents one of nonradiative emission types where the energy squanders in the form of heat ceased to the host crystal lattice.

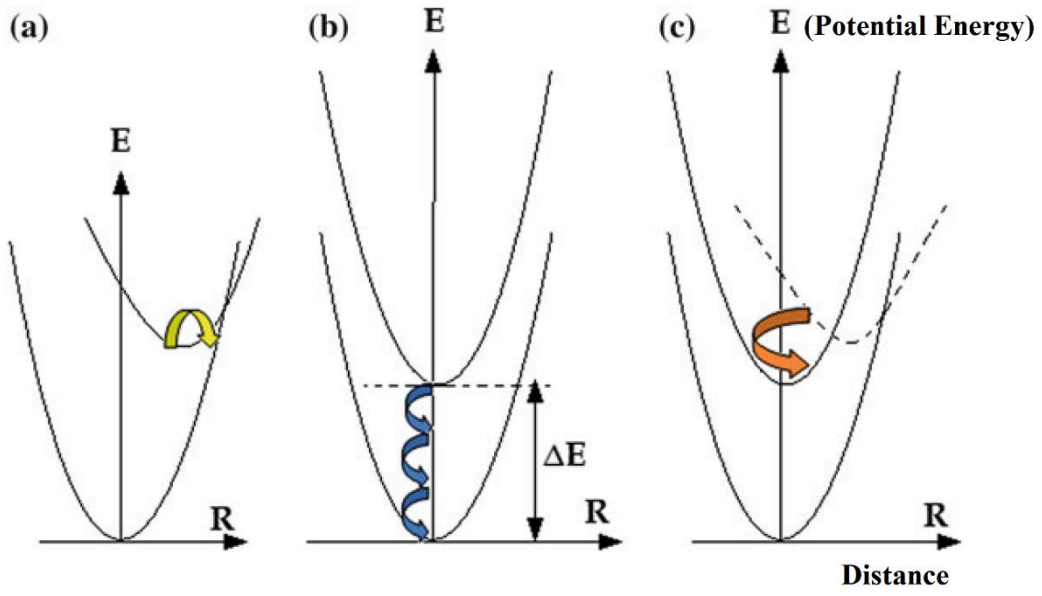

Figure 4. Different type of non-radiative transition of luminescent center based on the configurational coordinate model [6].

In this case, especially at high temperatures, there is a possibility for parabolas of excited and ground state, to intersect at some point. Excited electrons could pass

through this crossing and return to base energy level in nonradiative way. In **Figure 4**b, the parabolas of ground state and excited state are parallel. If the energy difference is equal to or less than four to five times the higher vibrational frequency of the surrounding, it can simultaneously excite a few high-energy vibrations, and therefore the energy dissipates for the radiation of phonons. This is called multiphonon emission. There are situations where radiative and nonradiative transition can happen simultaneously. Configuration coordinate diagram corresponding to this condition is presented in **Figure 4**c where solid lines, belonging to the same configuration, are intersected by dashed line which comes from a different configuration. While transition to the excited state with lower energy (solid line) is not allowed optically, it is allowed to higher excited state (dashed line). Electrons could be excited through allowed transition. From there electron can release their energy nonradiatively and arrive at second excited state where emission occurs from it.

The nonradiative transition is an undesirableprocess which involves energy losses in two forms: local vibrations of surrounding atoms which is called phonons in solids and the energy transferred to electronic states of atoms in vicinity, such as energy transfer. Cross-relaxation is a particular form of energy transfer which can take place between atoms of either same kind or different elements. Energy transfer is the mechanism which causes quenching of luminescent emission of rare earth elements in higher concentrations. Quenching refers to any process which decreases the fluorescence intensity of a given substance. A variety of processes can result in quenching, such as excited state reactions, energy transfer, complex-formation and collisional quenching.

1.4.3 Cross-relaxation

Cross-relaxation is an important form of nonradiative transition which has been responsible for quenching of luminescence emission at high concentration of activator, dispersed inside the host matrix. Cross-relaxation takes place between two adjacent localized luminescent centers. **Figure 5** illustrates this process happening among a pair of rare earth ions where one of the ions losses the energy (E_3-E_2) with relaxing to the lower energy level E_2 (which also can be ground level E_1) and the released energy has been captured by another ion to acquire higher energy level E'_2. The energy differences

may be either the same or matched by two or three phonons. Cross-relaxation can also occur between two differing elements, which happen to have two pairs of energy levels separated by the same amount [8].

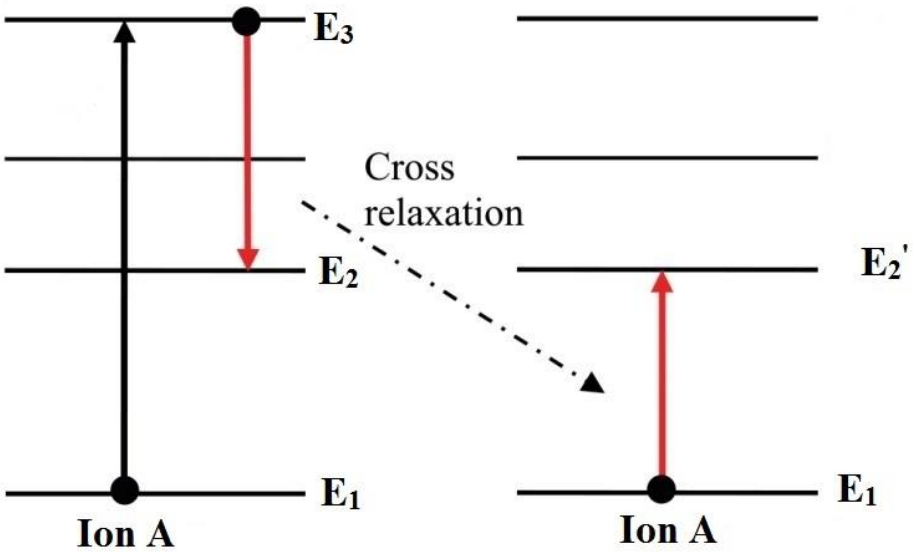

Figure 5. Illustration of cross-relaxation between same or different ions [8].

1.4.4 Features of Rare Earth (RE) Ions with regards to Luminescence

Due to wide utilization of Rare Earth ion doped inorganic solids in display application of luminescence, it bears prominent importance to understand the mechanism behind this phenomenon. There are four fundamental factors which should be considered in this context. Those parameters could be listed as excitation type and spectrum, transition to emitting level and decay time, emission intensity and emission spectrum. Host materials have high influence on these factors.

Luminescence properties of Rare Earth (RE) ions is related to the existence of partly filled and deep-lying $4f$ shell. Because of presence of outer electron shells (screening effect), $4f$ electron levels discrete to numerous energy levels. It has been well understood that these energy levels are hardly effected by crystal lattice of host

material therefore energy diagram of free ions is very similar to those incorporated inside a solid.

Despite the fact that energy levels of the free rare earth ions and those inside the solid are close to each other, emission properties of them are slightly differ from each other. RE ions absorbs energy and emits it in different wavelength. This effect, which has been called "Stokes Shift", stems from the fact that absorption and emission occurs between different energy levels of $4f$ electron shell. Usually, absorption corresponds to the transition from ground state to higher excited states. Electron in the higher excited state then loses energy to lattice till the states lying just below the previous excited states are available. When the difference between the adjacent states is large, then the energy corresponding to this transition cannot be transferred to lattice and it is given out in the form of emission. The emission thus corresponds to the transition from the intermediate state to the ground state.

Generally RE ions have three oxidation states. Ions with electronic configuration of $4f^0$ (La^{3+}), $4f^7$ (Gd^{3+}), are stable, however other lanthanide elements such as Tb^{3+}, Dy^{3+} and Sm^{3+} are inclined to reach this stable electronic configuration by losing electrons. Understanding the energy level of RE ions is crucially important in order to study their luminescent features. The energy level of RE ions could be classified into three groups.

Energy levels related to $4f^n$ configuration, those matching with $4f^{n-1}5d$ configuration and energy levels which are analogous to charge transfer between neighboring atoms [6].

1.4.5 Discrete $f - f$ Transition

There are numerous discrete $4f$ energy levels in RE ions. Moreover, their number grows as a result of crystal field splitting. For example Gd^{3+} ion has 327 levels of $4f$configuration. In most of the cases energy levels with photoluminescence features could be excited by UV light and usually other levels are neglected.

Although according to Selection Rule which determines if a transition between two states are allowed or not, transition inside the $4f$ shell is utterly restricted - due to unchanged parity, interaction of RE ion with host lattice vibration could lead to introduction of different parities into $4f$ states. Vibrionic transitions of RE ions are due to coupling of state $4f^n$ with the vibrational mode of the lattice. The characteristic energy levels of 4f electrons of trivalent lanthanide ions have been precisely investigated by Dieke et. al. The results are shown in **Figure 6**, which is known as a Dieke diagram [9].

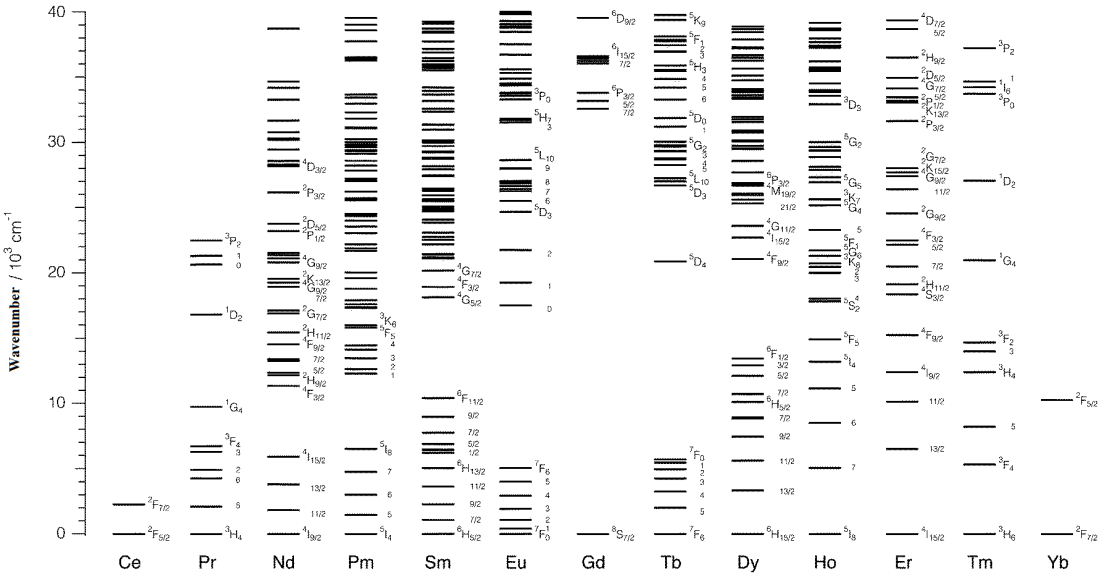

Figure 6. Dieke Diagram of rare Earth ions [9].

1.4.6 Electronic Configuration

Generally, RE elements are composed of 17 elements, including all 15 lanthanides plus Sc and Y. **Table 1** presents the electronic configuration of RE^{3+} ions in their ground state. According to the table, Sc^{3+} corresponding element is Ar, for the Y^{3+} is Kr and for ions from La^{3+} to Lu^{3+} it is Xe. There are one to fourteen electrons, filling the 4f orbitals of ions from Ce^{3+} to Lu^{3+}, in addition to their fully occupied inner shells which correspond to Xe. Ions such as Sc^{3+}, Y^{3+}, La^{3+} and Lu^{3+} do not exhibit luminescence features because they cannot be excited in or near visible region due to

lack of 4f electrons. However, ions from Ce^{3+} to Yb^{3+} with partly filled 4f orbitals present various luminescent capabilities originated from their characteristic energy levels. Therefore they can be utilized as luminescent centers in inorganic phosphors by substituting Y^{3+}, Gd^{3+}, La^{3+} and Lu^{3+} in different crystal compounds [2].

4f orbitals have azimuthal quantum number (l) of 3 which leads to 7 ($=2l+1$) orbitals, each capable of holding 2 electrons. In the ground state all the available electrons should be distributed in such a way that combined spin angular momentum (S) reaches its' maximum value. Total angular momentum (J), which can be defined as a combination of spin angular momentum and orbital angular momentum (L), is as follows;

$$J = |L - S|, \quad Number\ of\ 4f\ electrons\ < 7$$

$$J = |L + S|, \quad Number\ of\ 4f\ electrons\ > 7$$

Term symbol, which is used commonly in order to indicate an electronic state, is in the form of ${}^{2S+1}L_J$, where L symbolize $S, P, D, F, G, H, I, K, L, M, \ldots,$ equivalent to L = 0, 1, 2, 3, 4, 5, 6, 7, 8, 9,… respectively [2].

Table 1: Electronic Configurations of Rare-Earth Ions in the Ground State [2].

Atomic number	Ions	Corresponding element	$4f$ electros	S $\sum s$	L $\sum l$	J $\sum(l+s)$
21	Sc^{3+}	Ar		0	0	0
39	Y^{3+}	Kr		0	0	0
57	La^{3+}			0	0	0
58	Ce^{3+}	Xe	↑	1/2	3	5/2
59	Pr^{3+}	Xe	↑ ↑	1	5	4
60	Nd^{3+}	Xe	↑ ↑ ↑	3/2	6	9/2
61	Pm^{3+}	Xe	↑ ↑ ↑ ↑	2	6	4
62	Sm^{3+}	Xe	↑ ↑ ↑ ↑ ↑	5/2	5	5/2
63	Eu^{3+}	Xe	↑ ↑ ↑ ↑ ↑ ↑	3	3	0
64	Gd^{3+}	Xe	↑ ↑ ↑ ↑ ↑ ↑ ↑	7/2	0	7/2
65	Tb^{3+}	Xe	↑↓ ↑ ↑ ↑ ↑ ↑ ↑	3	3	6
66	Dy^{3+}	Xe	↑↓ ↑↓ ↑ ↑ ↑ ↑ ↑	5/2	5	15/2
67	Ho^{3+}	Xe	↑↓ ↑↓ ↑↓ ↑ ↑ ↑ ↑	2	6	8
68	Er^{3+}	Xe	↑↓ ↑↓ ↑↓ ↑↓ ↑ ↑ ↑	3/2	6	15/2
69	Tm^{3+}	Xe	↑↓ ↑↓ ↑↓ ↑↓ ↑↓ ↑ ↑	1	5	6
70	Yb^{3+}	Xe	↑↓ ↑↓ ↑↓ ↑↓ ↑↓ ↑↓ ↑	1/2	3	7/2
71	Lu^{3+}	Xe	↑↓ ↑↓ ↑↓ ↑↓ ↑↓ ↑↓ ↑↓	0	0	0

1.4.7 Selection Rule

The selection rule determines if a transition between two states are allowed or not. The electronic state of a free atom in LS-coupling system could be presented by its Spin (S), Orbital (L) and total angular momentum (J), and ΔS, for instance, represents the difference between spin momentums of two states. The selection rules for electric dipole and magnetic dipole transition in LS-coupling system are as follows:

$$\Delta S = 0,\ \ \Delta L = 0 \quad or \quad \pm 1$$

$$\Delta J = 0 \quad or \quad \pm 1 \ \ (J = 0 \rightarrow J = 0 \quad not \ \ allowed)$$

Despite the fact that transition between electronic states with same parity are not allowed - as it applies for f-f transitions of free rare earth ions - however, when they incorporate in crystals they can become partly allowed as a result of crystal field influence. The selection rule which controls the partially allowed f-f transitions can be expressed as follows:

$$|\Delta J| \leq 6 \ (j = 0 - 0, 1, 3, 5 \ are \ forbidden)$$

1.4.8 Photoluminescence properties of Dysprosium (Dy)

Photoluminescence properties of Dysprosium has been investigated recently by Lemański et al. [10]. They found that excited Dy can emit light in different color ranges at the same time. This unique feature of Dy makes it a promising option to be used in producing white LEDs. Reddy et al. [11] have presented the energy level diagram of Dy. As **Figure 7** indicates there are three main visible emissions from the $^4F_{9/2}$ level at 484, 576 and 664 nm. These three emissions which respectively corresponds to blue, yellow and red colors can be attributed to $^4F_{9/2} \rightarrow {}^6H_{15/2}$, $^4F_{9/2} \rightarrow {}^6H_{13/2}$ and $^4F_{9/2} \rightarrow {}^6H_{11/2}$ transitions. Sahu et al. [12] have studied the luminescence properties of Dy doped inside a silicate base host material. They found that $^4F_{9/2} \rightarrow {}^6H_{13/2}$ transition is highly effected by the Dy^{3+} environment inside the host lattice.

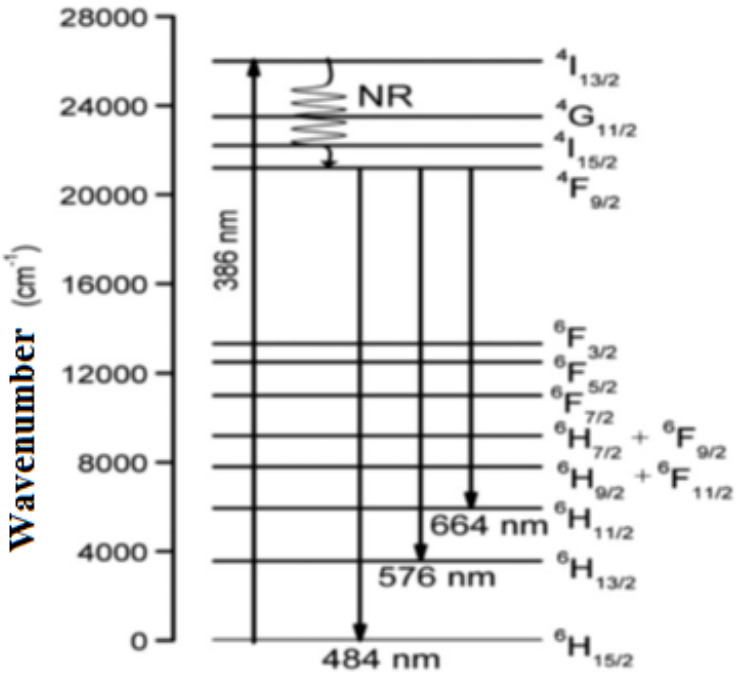

Figure 7. Energy level Diagram of Dy^{3+} ion [11].

1.4.9 Photoluminescence properties of Terbium (Tb)

Terbium is one of the most utilized rare earth elements in luminescence applications such as flat displays, mercury free fluorescent tubes and plasma panels [13]. Most recently, Rakov et al. [14] have investigated the Terbium luminescent properties and presented the energy diagram of the Tb^{3+} ion as it is shown in **Figure 8**. It can be seen that the emissions largely take place from the $^5D_4$ level. It has been observed that $^5D_4 \rightarrow {}^7F_5$ transition which corresponds to 549 nm (green color) has the strongest intensity of luminescent emission [15]. Velchuri et al. have studied the synthesis and photoluminescence of several rare earth orthoborate. They have investigated the photoluminescence properties of Tb doped samples and found that by recording the excitation spectra under wave length of 543 nm the maximum absorption occurs at 378 nm [16].

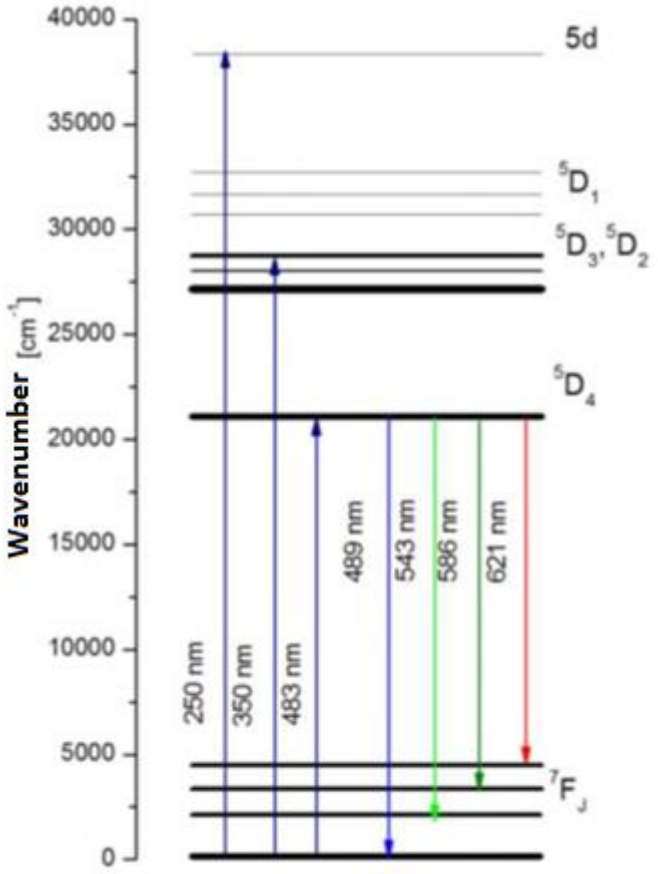

Figure 8. Energy level Diagram of Tb^{3+} ion [17].

1.4.10 Photoluminescence properties of Samarium (Sm)

Luminescent properties of Sm have been researched by Bedyal et al. [18]. They have doped different amount of Sm inside the $NaCaBO_3$ host material by using combustion method. They found that Sm have three emission in the visible range in the 568, 601 and 668 nm wavelength. The most intense emission was coming from the $^4G_{5/2} \rightarrow {}^6H_{7/2}$ transition which corresponds to orange color with 601 nm wavelength. **Figure 9** represents the energy level of Sm^{3+} ion. As it can be seen Sm^{3+} ions can absorb the UV light in different wavelengths. Photoluminescence of Sm have also been studied in other host materials. For example Cao et al. have tried TiO_2 as host material doped with Sm in order to produce red-orange color phosphor [19]. Huang et al. have used $Na_5Eu(WO_4)_4$ as host material for investigation of photoluminescence features of Sm [20].

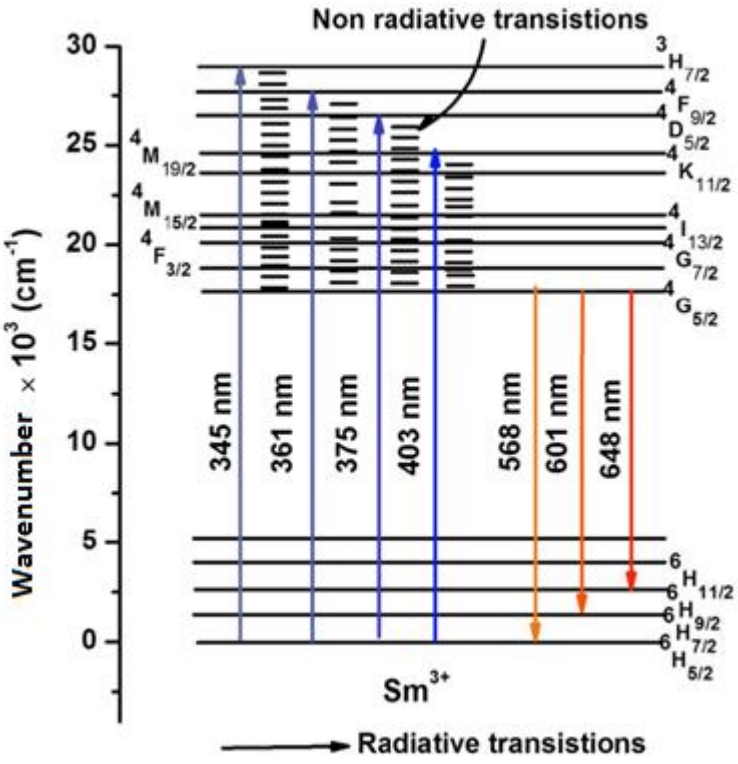

Figure 9. Energy level Diagram of Sm^{3+} ion [18].

1.5 Crystal structure of Rare-Earth Orthoborates

Boron is a semi-metallic element with 5 atomic number which is placed on the third group and second period of periodic table of chemical elements. Boron is a scarce element in the whole solar system including the Earth crust. Due to high reactivity of Boron, it cannot be found as a free element in the nature however it forms chemical compounds with other elements which is called borate minerals. There are large number of borate minerals in the nature which most of them are formed from different amount of boroxide (B_2O_3) such as Tincal ($Na_2B_4O_7.10H_2O$), Colemanite ($Ca_2B_6O_{11}.5H_2O$), Kernite ($Na_2B_4O_7.4H_2O$) and Ulexite ($NaCaB_5O_9.8H_2O$) [21]. The known total deposit of world Boron minerals based on the B_2O_3 is about 1.3 billion tons. The world major boron deposits are in Turkey. The world total production of B_2O_3 is 1.96

million tons. Turkey is the main supplier of borate minerals with the market share of 48% of total production. Other main producers are North America (USA, 29%), South America (Argentina, Chile, Peru, Bolivia, 12%) and Asia (Russia, China, India, 11%). **Table 2** summarizes the share of main borate reserves by each country [22]. Borates have vast range of application in several industries such as glass production, agriculture, Ceramic and semi-conductor [23], [24][25]. Today the 52% of the produced boron is used in the glass fabrication such as isolation type fiberglass, textile type fiberglass and borosilicate glasses.

Table 2: Global B_2O_3 stockpile.

Country	**B_2O_3 Total Reserve (million tons)**	**Distribution (%)**
Turkey	955.3	72.8
Russia	100	7.6
USA	80	6.1
Chile	41	3.2
China	47	3.6
Peru	22	1.7
Bolivia	19	1.4
Kazakhstan	15	1.2
Argentina	9	0.7
Serbia	24	1.7
Total	1312.3	100

Rare-earth orthoborates were investigated by Levin et al. for the first time in 1961. They found that rare-earth orthoborates are family of polymorphous materials which their crystal structure are corresponding to three different crystalline form of Calcium Carbonate ($CaCO_3$). These polymorphous were named as aragonite, vaterite and calcite types [26]. The size of cation (RE^{3+}) determines whether the compound is

aragonite, vaterite or calcite type [27]. According to Velchuri et al., radius ratio of lanthanum and oxygen ions (Ln^{3+}/O^{2-}), is the most effective factor in formation of different types of lanthanum orthoborates. When the ratio is equal to or larger than 0.71, it results in aragonite structure in the final lanthanide borate compound [28]. With the radius ratio laying between 0.71 and 0.61, vaterite structure of lanthanum borates is prevailing [29]. Finally radius ratio of less than 0.607, leads to either calcite or vaterite type of structure based on synthesis temperature [30]. For example while La^{3+} due to its large size forms an orthorhombic aragonite crystal structure, smaller ions like Y^{3+} and Gd^{3+}, produces vaterite type orthoborates which exhibit semi-hexagonal symmetry. When the smallest rare earth ion (Sc^{3+}) occupies the single site for the cation with S6 point symmetry, the final compound turns out as a rhombohedral calcite structure. Nevertheless, today five crystal structures (based on previously described crystalline forms) of the RE orthoborates are known: the hexagonal vaterite type (space group P63/m, No. 176), the orthorhombic aragonite type (Pnam, No. 62)[31], the rhombohedral vaterite type (R32, No. 155), and the rhombohedral calcite type (R3c, No. 161) and monoclinic pseudowollatonite type (C2/c, No.15). It is very important to notice that BO_3 triangles are different from the standard $CaCO_3$ vaterite [32,33].

1.5.1 $LaBO_3$

Lanthanum borate, $LaBO_3$, has aragonite orthorhombic structure with *Pnma* space group. $LaBO_3$ has pseudo-hexagonal structure, which means that c-axis is parallel to the orthorhombic b-axis. $LaBO_3$ unit cell parameters are: a = 5.115 Å , b = 8.269 Å , and c = 5.881 Å , volume, V = 248.76(9) $Å^3$ and Z = 4 molecular units per unit cell [34,35]. The $LaBO_3$ structure is comprised of trigonal planar borate anions, which form an infinite net that lies perpendicular to the c-axis, with the lanthanide ions residing between the layers. Each lanthanum cation is coordinated to nine oxygen atoms (LaO_9) from six different borates. Each LaO_9 polyhedron shares edges with six other LaO_9 polyhedra and three BO_3 triangles, whereas each BO_3 triangle shares edges with three LaO_9 polyhedra [35]. Three of the six borates are bidentate and three are monodentate having single coordination to La^{3+} [36]. Infrared spectroscopy is the most

effective technique to identify borate anionic structures based on the stretching and bending vibrational modes. It has been reported that symmetric and asymmetric stretching modes and in-plane and out-of-plane bending modes gave rise to absorption bands centered at around 1250, 940, 700, 610 and 590 cm^{-1} [37].

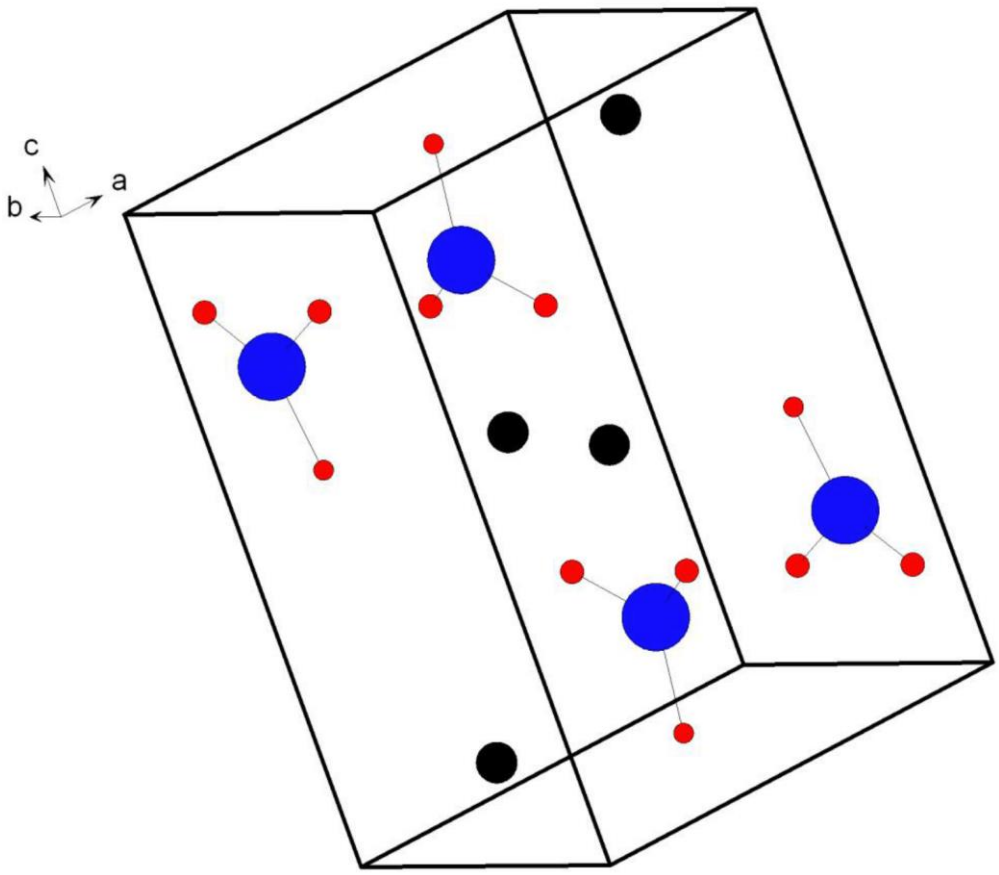

Figure 10. The crystal structure of $LaBO_3$ (Blacks: La atoms, Blues: B atoms, Reds: O atoms) [38].

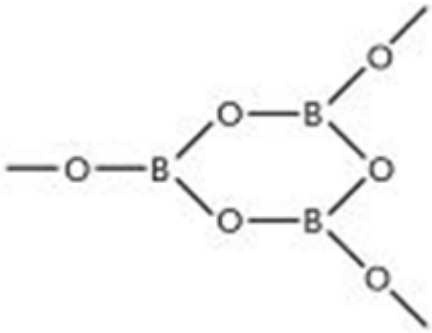

Figure 11. Planar BO_3 [38].

1.5.2 $GdBO_3$

Gadolinium borate, $GdBO_3$ adopts vaterite structure type, and is categorized in the space group R32 with hexagonal crystal system. The Lattice parameters of $GdBO_3$ are: a = 6.6357 Å, c = 26.706 Å, unit cell volume: 1018.44 $Å^3$ and Z = 2 molecular units per unit cell [39]. $GdBO_3$ structure is composed of tetrahedral polyborates (BO_4) that form $B_3O_9^{9-}$ rings. These polyborate rings develop as layers between which the gadolinium ions stay. The gadolinium ions in the crystal structure is surrounded by eight oxygen atoms [40].

The infrared studies of borate in vaterite structures like $GdBO_3$ indicates that there are several absorption bands which can be attributed to the stretching and bending modes of $B_3O_9^{9-}$ rings. Weir et al. have specified that bands at around 1105, 970, 900, 810 cm^{-1} are originated from stretching mode of $B_3O_9^{9-}$ rings and the bands center around 690 and 565 cm^{-1} are due to bending modes of $B_3O_9^{9-}$ rings [41]. **Figure 13** shows structural sketch map of $B_3O_9^{9-}$ ion.

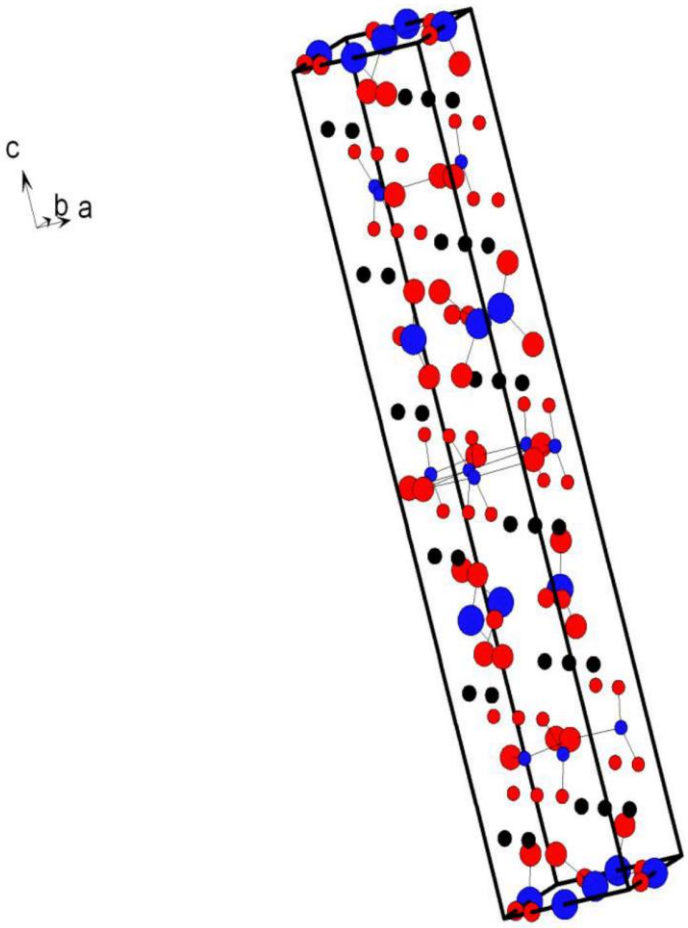

Figure 12. Crystal structure of $GdBO_3$ (Blacks: Gd atoms, Blues: B atoms, Reds: O atoms) [38].

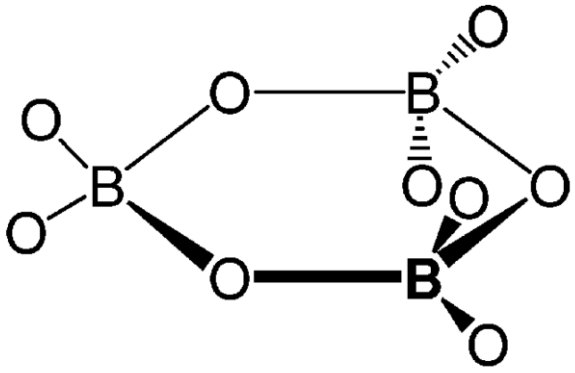

Figure 13. Structural sketch map of $B_3O_9^{9-}$ ion [42].

1.6 Synthesis Method

There are several synthesis methods which have been used over long period of time to produce inorganic powder materials. These methods include solid state or ceramic method, combustion method, sol-gel method, microwave assisted method and high pressure methods like hydrothermal technique. Each of those mentioned synthesis techniques have their own advantages and disadvantages. There are number of factors which should be considered in the process of selecting appropriate synthesis method such as energy and time utilization, the quality of final compounds in terms of impurities and homogeneousness. The stability of compounds under reaction conditions is also highly important because for instance some substances decompose at high temperatures.

Solid-state or ceramic method is the most simple and primitive method in order to produce wide range of solid compounds. In this technique two or more reactants are mixed and ground together and then heated at high temperature to produce required product. Since the reaction takes place at the surface of the solid reactants, grinding process should be implemented diligently. In spite of its common utilization, ceramic method has some critical drawbacks. For example the high temperature which is applied in the procedure inevitably requires larger energy inputs. Moreover there is a risk of losing desired compounds due to the high temperature.

Combustion method or with its other name self-propagating high-temperature synthesis has been developed as an alternative to ceramic pathway. In combustion technique a highly exothermic or even explosive redox reaction usually employees to produce desired products. Compared with ceramic method, combustion method is more cost effective due to lower energy demand. It also can be used to prepare materials in industrial scale [43]. The major handicap of combustion method is that it causes high porosity in the final product. Although some solutions have been suggested to address this problem, however, those solutions have led to some difficulties in sustaining a stable propagation of the combustion reaction [43].

Sol-gel method is another promising method in order to fabricate different materials. In this method first the reactants are mixed together to form a concentrated solution which is called sol. Then the obtained sol goes through the aging procedure to form a homogenous gel which then heated to form the final product. Sol-gel synthesis offers some advantages over conventional ceramic synthesis. It requires less temperature compared to ceramic synthesis. It also can be used to prepare very fine powders. Moreover, sol-gel synthesis can be used to produce materials with organic-inorganic composition which is not feasible in ceramic synthesis.

Nonetheless Sol-gel synthesis have some disadvantages such as high cost of raw materials especially for the alkoxides [44]. Another limitation of sol-gel method is that in the drying stage there is a high amount of volume shrinkage thus high risk of cracking of the final product.

Microwave assisted synthesis method is one the most recent approaches in the field of producing solid materials. In this method dielectric heating is used to heat up the reactants and accelerate the reaction between them. Microwave synthesis is superior in some aspects over other conventional synthesis method especially ceramic method. It requires less energy so it's much more economical than ceramic method. Moreover it's fast and clean. However there are some restrictions about microwave synthesis usage. One of the limitations is that in order to apply this method in synthesis, at least one of the reactants should absorb microwave strongly. Although this problem can be resolved with using a fuel, however, the procedure of finding appropriate fuel is complicated and based on trial and error [45].

Nowadays, much efforts have been devoted to develop nano or micro structures with well-defined shapes and geometries due to their unique chemical and physical properties which are deeply related to their geometrical features such as morphology, size, orientation and dimensionality. [46-49] For instance materials with hollow and porous structures show effective performance on drug delivery and catalysis due to their large surface area and high adsorption capabilities [50,51] or 1-D metal nanowires which can be used in electronic devices [52].

According to recent researches with focus on rare earth orthoborates it has been well understood that shape, size and orientation of crystals have vital impact on the luminescent property of these materials. [27][53,58] Therefore there is a growing inclination among researchers toward better understanding and control of structure of available materials, instead of, efforts toward developing novel phases and materials. Nevertheless, the traditional methods derived for preparation of rare earth orthoborates are mainly include solid-state reaction [59,60] method, sol-gel technology [61,62] and the ammonium nitrate melt method [63,64]. Although these methods are successful in synthesis of rare earth orthoborates however due to high synthesis temperature or iterative grinding process, the resulting material inevitably possess bad morphology. Therefore, it is highly desired to synthesize phosphor with homogeneous and regular morphology by a controllable approach toward durable structures. The hydrothermal (HT) approach is a good choice due to its convenience, exemption from pollution, and the possibility of achieving satisfying crystallinity at a relatively low temperature, without further calcination.

Self-assembly of nano crystals during their growth period is a promising method in order to prepare materials with sophisticated architecture. [46][65,67] In this method by devising appropriate synthesis route, tiny growing crystal centers (primary building blocks) can be joined together and pave the way for different types of shapes. However, because of divers growing habits, crystalline phase and composition of each material, synthesis condition for aimed geometry are varied from one material to another.

1.6.1 Hydrothermal Synthesis

Hydrothermal method is one of the most popular approach to grow crystals. In this method reactants are dissolved in water and put inside a closed vessel or bomb which is called autoclave. After sealing the autoclave properly, it is heated inside a furnace. The autoclave should be made of thick stainless steel in order to resist the hight pressure. In addition, in order to prevent any explosion a safety valve should be mounted to the vessel. Inner side of an autoclave is usually lined with an inert or nonreactive material such as Teflon, quartz or noble metals. A typical hydrothermal

procedure involves the heating of a water solution inside an autoclave, as a result of heating, temperature increases, meanwhile, because the system is closed, pressure also goes up. The water remains liquid even when the temperature is above its' normal boiling point at 100˚C, so-called "superheated water". This condition, which is known as hydrothermal condition, is also observed in nature and large number of minerals such as natural zeolites and gemstones are produced through this procedure [68].

Hydrothermal method has some advantages over other methods such as solid-state (ceramic) and sol-gel synthesis. Lower synthesis temperature is one of them. Hydrothermal synthesis is also favorable when the reactants are in unusual oxidation states and phases, however become stable at high temperature and pressure. For example, metal oxides which are not soluble in water in atmospheric pressure can be dissolved in hydrothermal condition.

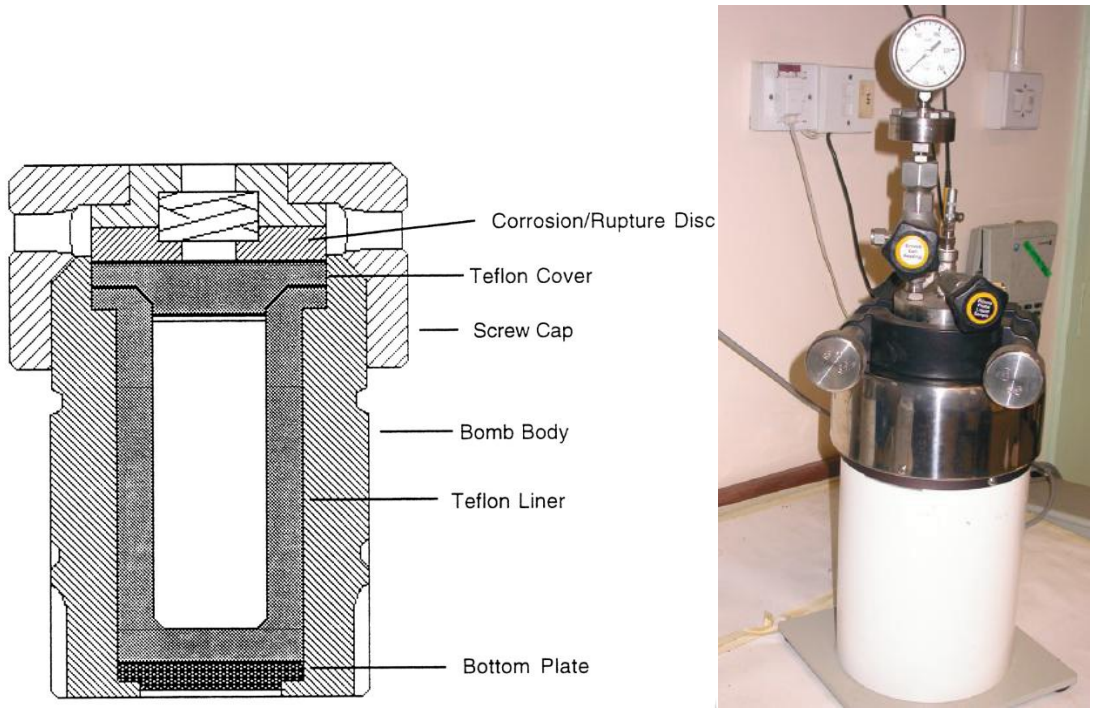

Figure 14. Sketch of an autoclave [69].

1.7 Objective

In this thesis a hydrothermal technique will be presented to produce $LaBO_3$ and $GdBO_3$ orthoborates nanocrystals which are self-assembled into a three dimensional microstructure geometry. After doping with rare earth ions Dy^{3+}, Tb^{3+} and Sm^{3+} in various concentrations, the effect of host material and doping concentration on the photoluminescence properties of samples will be investigated through wide range of characterization techniques.

CHAPTER 2

MATERIALS AND METHODS

2.1 Materials

Table 3 lists the number of materials which were used for preparing samples in this study. All the materials, except deionized water, were in powder form.

Table 3: List of the materials, their application and labels

Used material	Applied as	Label
$LaCl_3.6H_2O$	Precursor of $LaBO_3$	Merck ≥98%
$GdCl_3.6H_2O$	Precursor of $GdBO_3$	abcr 99.9%
$DyCl_3.6H_2O$	Dopant agent of Dy^{3+}	abcr 99.9%
$TbCl_3.6H_2O$	Dopant agent of Tb^{3+}	Acros Organics 99.9%
Sm_2O_3	Dopant agent of Sm^{3+}	Aldrich 99.9%
H_3BO_3	Source of borate	Merck
La_2O_3	Precursor of $LaBO_3$	Aldrich 99.9%
Dy_2O_3	Dopant agent of Dy^{3+}	Aldrich 99.9%
B_2O_3	Source of borate	Aldrich 99

2.2 Instrumentation

2.2.1 Powder X-Ray Diffraction (XRD)

X-ray diffraction is a well-known method in investigating crystal structure of materials. Its versatility and nondestructive feature makes it an indispensable method in order to study the phase composition, grain size, lattice constants and degree of crystallinity. X-ray diffraction, also can be used for both qualitative and quantitative analysis. Qualitative identification is carried out by comparing the x-ray diffraction pattern known as a diffractogram, of the unknown sample with the internationally recognized JCPDS data base which contains the reference patterns for more than 75,000 phases.

Powder XRD analysis of prepared samples were conducted under ambient conditions by using Rigaku X-ray Diffractometer (Model: Miniflex) which was operated at 30 kV and 15 mA. The source of the X-ray radiation was Cu Kα (λ =1.54Å). The range of analysis (2θ) was between 3˚ and 90˚ degrees and the speed of scanning was adjusted to 1 ˚ /min. scanning resolution had been set to 0.01.

2.2.2 Fourier - Transform Infra - Red Spectroscopy (FTIR)

Infra-red analysis of prepared samples have been carried out using a Bruker IFS 66/S spectrometer in conjunction with Attenuated Total Reflectance (ATR) sampling technique which was supplied with a ZnSe crystal and the beam incident at an angle of 45°. ATR-IR analysis has been conducted over 500-4000 cm^{-1} range and the resolution of measurement was set to 4 cm^{-1}.

2.2.3 Far-IR Spectroscopy

Far-IR analysis of synthesized samples were performed using a Nicolet™ 6700 FT-IR spectrometer. The samples used in analysis were prepared as pellets. Each pellet consists of 100 mg high density polyethylene (HDPE), as window, and 3 mg of sample material. The pressure applied in the pressing procedure was 5 ton for 5 minutes. FAR-IR analysis was conducted over 50-1200 cm^{-1} range and the resolution of measurement was set to 4 cm^{-1}.

2.2.4 Scanning Electron Microscope (SEM)

The morphology and geometrical shape of produced samples have been studied using a scanning electron microscope (SEM) at the Middle East Technical University central laboratory (MerLab). The equipment used for this analysis was QUANTA 400F Field Emission SEM instrument with operational conditions as follows: SEM analysis was conducted under the high vacuum condition with (Everhart Thornley Detector) ETD sdcondary electron detector and a beam gun with 20 kV voltage.

2.2.5 Photoluminescence measurement

Photoluminescence features of produced materials have been studied by Varian Cary Eclipse Fluorescence Spectrometer. The samples were analyzed in powder form inside the solid sample holder accessory. The positon of sample holder were adjusted in the way that optimum signal had been obtained. Both excitation and emission slits had been optimized to 5 mm. Scanning speed of PL record was set to 100 nm/min. In order to prevent scattered lights from the sample surface to enter into the detector and interfere with emitted light from the sample, filtration was applied. First filter was used in the excitation side with 240-395 nm band pass range. Second filter was applied in the emission side with 430-1100 nm band pass range. The voltage of detector was set to default for all measurements.

2.3 Synthesis of Dy, Tb and Sm doped $LaBO_3$ and $GdBO_3$

In this study $LaBO_3$ and $GdBO_3$ have been synthesized as two different host lattice and each of them has been doped with three rare earth including Dysprosium, Terbium and Samarium. Synthesis procedure as described in the introduction part was hydrothermal method. RE doped samples were prepared in different concentrations in the range of 2.5 to 15 mol %. Each experiment has been repeated at leat twice.

The synthesis route can be described as follows:

2 mmol of $LaCl_3.8H_2O$ was dissolved inside 35 mL of deionized water and stirred for 5 minutes. Following that, 10 mL of 0.5M NaOH solution was added to the mixture

and continued to stir for another 5 minutes which led to formation of $La(OH)_3$ colloids. Finally, 390 mg of H_3BO_3 was added into the solution and whole mixture was stirred for 30 minutes at room temperature. After 30 minutes, resulting solution was moved into a 100 mL Teflon lined autoclave and sealed vigilantly. Subsequently, the autoclave was put inside a furnace and heated at 200˚C for 24 hours. After 24 hours of heating, the autoclave cooled to room temperature naturally and the products, which were solid powders precipitated at the bottom of the Teflon container, were collected. Then, produced solid powder was washed several times with deionized water and dried at 80˚C for 24 hours inside an owen [46]. Other Lanthanum orthoborate compounds were synthesized through the same route except $LaCl_3.8H_2O$ was replaced with different Lanthanum chlorides in the first stage of the synthesis. Doped lanthanum orthoborate samples were prepared in the form of $D_xH_{1-x}BO_3$, Where D=Dy, Tb and Sm and H= La and Gd. All doped samples were also produced with the same synthesis method by adding stoichiometric amount of dopant into the solution in the first step of the synthesis. Schematic illustration of synthesis route has been presented in **Figure 15**.

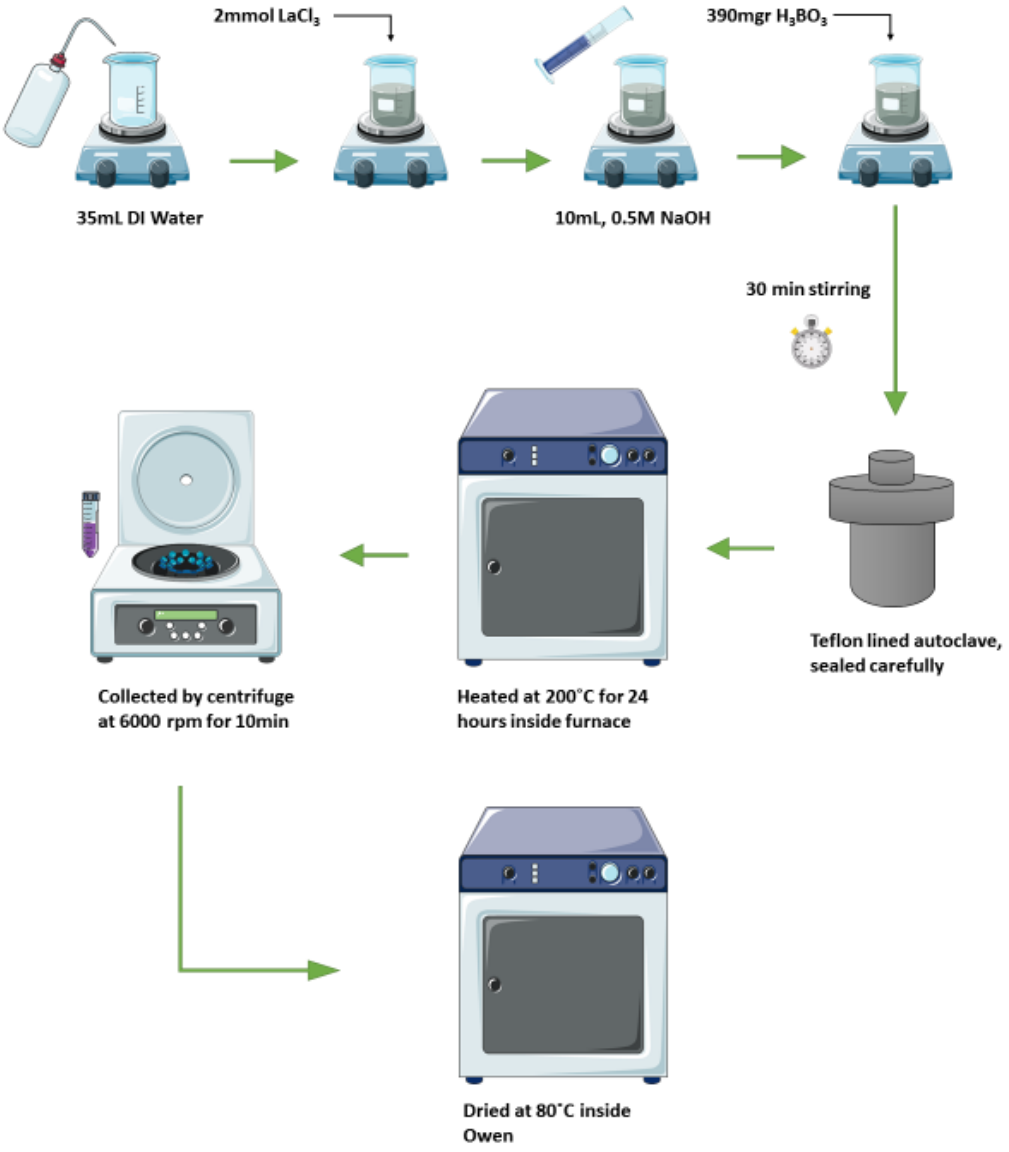

Figure 15. Synthesis route of Dy, Tb and Sm doped $LaBO_3$ and $GdBO_3$

Tables 4 to 9 show the amount of materials used in the synthesis of each sample. The values have been obtained by stoichiometric calculation. Here calculations for the 2.5% Dysprosium doped $LaBO_3$ has been provided as an example:

$$DyCl_3.8H_2O\ Molecular\ weight = 376.96\ g/mol$$

$$LaCl_3.8H_2O\ Molecular\ weight = 371.37\ g/mol$$

$$2 \times 10^{-3} mol \times \frac{2.5}{100} DyCl_3.8H_2O \times \frac{376.96\ g}{1mol} = 18.8 \times 10^{-3}\ g\ DyCl_3.8H_2O$$

$$2 \times 10^{-3} mol \times \frac{97.5}{100} LaCl_3.8H_2O \times \frac{371.37\ g}{1mol} = 724.2 \times 10^{-3} g\ LaCl_3.8H_2O$$

Table 4: Calculation results of Dy doped $LaBO_3$

sample name	$LaCl_3.6H_2O$[mg]	$DyCl_3.6H_2O$[mg]	NaOH[mL]	H_3BO_3[mg]
2.5%Dy-$LaBO_3$	724.2	18.8	10	390
5%Dy-$LaBO_3$	705.6	37.7	10	390
7.5%Dy-$LaBO_3$	687.0	56.5	10	390
10%Dy-$LaBO_3$	668.5	75.4	10	390
12.5%Dy-$LaBO_3$	649.9	94.2	10	390
15%Dy-$LaBO_3$	631.3	113.1	10	390

Table 5: Calculation results of Dy doped $GdBO_3$

sample name	$GdCl_3.6H_2O$[mg]	$DyCl_3.6H_2O$[mg]	NaOH[mL]	H_3BO_3[mg]
2.5%Dy-$LaBO_3$	724.8	18.8	10	390
5%Dy-$LaBO_3$	706.2	37.7	10	390
7.5%Dy-$LaBO_3$	687.7	56.5	10	390
10%Dy-$LaBO_3$	669.1	75.4	10	390
12.5%Dy-$LaBO_3$	650.5	94.2	10	390
15%Dy-$LaBO_3$	631.9	113.1	10	390

Table 6: Calculation results of Tb doped $LaBO_3$

sample name	$LaCl_3.6H_2O$[mg]	$TbCl_3.6H_2O$[mg]	NaOH[mL]	H_3BO_3[mg]
2.5%Tb-$LaBO_3$	724.2	18.7	10	390
5%Tb-$LaBO_3$	705.6	37.3	10	390
7.5%Tb-$LaBO_3$	687.0	56.0	10	390
10%Tb-$LaBO_3$	668.5	74.7	10	390
12.5%Tb-$LaBO_3$	649.9	93.3	10	390
15%Tb-$LaBO_3$	631.3	112.0	10	390

Table 7: Calculation results of Tb doped $GdBO_3$

sample name	$GdCl_3.6H_2O$[mg]	$TbCl_3.6H_2O$[mg]	NaOH[mL]	H_3BO_3[mg]
2.5%Tb-$GdBO_3$	724.8	18.7	10	390
5%Tb-$GdBO_3$	706.2	37.3	10	390
7.5%Tb-$GdBO_3$	687.7	56.0	10	390
10%Tb-$GdBO_3$	669.1	74.7	10	390
12.5%Tb-$GdBO_3$	650.5	93.3	10	390
15%Tb-$GdBO_3$	631.9	112.0	10	390

Table 8: Calculation results of Sm doped $LaBO_3$

sample name	$LaCl_3.6H_2O$[mg]	Sm_2O_3[mg]	NaOH[mL]	H_3BO_3[mg]
2.5%Sm-$LaBO_3$	724.2	8.7	10	390
5%Sm-$LaBO_3$	705.6	17.4	10	390
7.5%Sm-$LaBO_3$	687.0	26.2	10	390
10%Sm-$LaBO_3$	668.5	34.9	10	390
12.5%Sm-$LaBO_3$	649.9	43.6	10	390
15%Sm-$LaBO_3$	631.3	52.3	10	390

Table 9: Calculation results of Sm doped $GdBO_3$

sample name	$GdCl_3.6H_2O$[mg]	Sm_2O_3[mg]	NaOH[mL]	H_3BO_3[mg]
2.5%Sm-$GdBO_3$	724.8	8.7	10	390
5%Sm-$GdBO_3$	706.2	17.4	10	390
7.5%Sm-$GdBO_3$	687.7	26.2	10	390
10%Sm-$GdBO_3$	669.1	34.9	10	390
12.5%Sm-$GdBO_3$	650.5	43.6	10	390
15%Sm-$GdBO_3$	631.9	52.3	10	390

2.3.1 Synthesis and assembly mechanism of Lanthanum Orthoborates

The procedure responsible for the formation and self-assembly of produced lanthanum orthoborates involves three reactions as follow;

$$LaCl_3 + 3NaOH \rightarrow La(OH)_3 + 3NaCl \quad \text{(I)}$$

$$H_3BO_3 \rightarrow BO_3^{3-} + 3H^+ \quad \text{(II)}$$

$$La(OH)_3 + BO_3^{3-} + 3H^+ \rightarrow La(BO)_3 + 3H_2O \quad \text{(III)}$$

Reaction 1 is very fast and produces $La(OH)_3$ hydroxide by adding NaOH solution to the mixture. In contrast, reaction 2 is slow to due to the weak acidity of H_3BO_3 and its ionization inside the water takes long time. As a result, conversion of $La(OH)_3$ hydroxides to $LaBO_3$ orthoborates takes place slowly.

At the same time, pH of the mixture also changes and it has significant impact on the self-assembly of the nano crystals. At the initial stage of the synthesis procedure when the pH of the mixture is basic, produced $La(OH)_3$ colloids possess negative charge on their surface. However pH of the reacting solution changes to acidic gradually, as the H_3BO_3 ionizes slowly. Formation of $LaBO_3$ nanocrystals take place at the acidic environment so they carry positive charge on their surface. The electrostatic attraction between negative charged $La(OH)_3$ colloids and positive charged $LaBO_3$ nanoparticles leads to combination of different nanocrystals which at the end results in self-assembled structures. It should be noted that the slow transformation from $La(OH)_3$ to $LaBO_3$ plays a key role in producing the assembled nanostructures [46]. **Figure 16** shows the schematic illustration of the growth and assembly mechanism of the $LaBO_3$ assemblies.

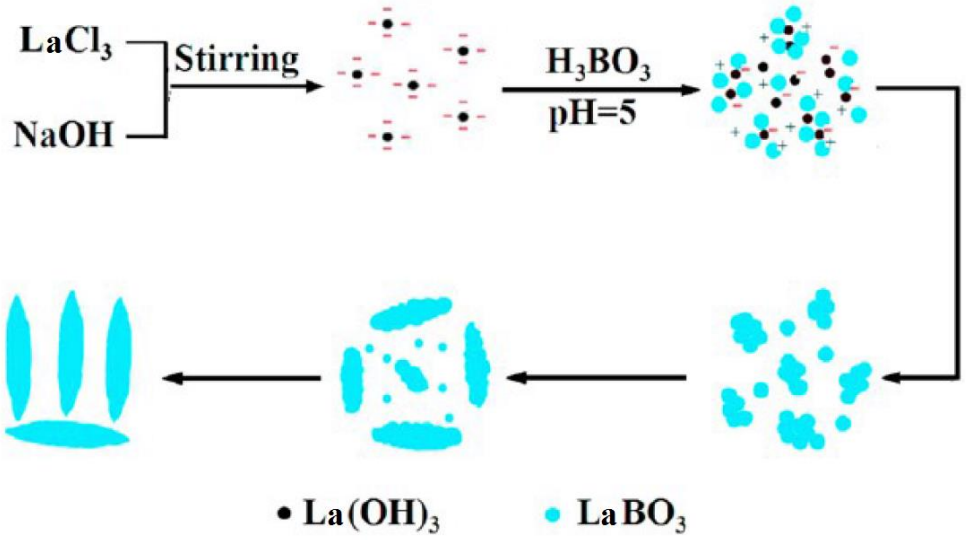

Figure 16. Self-assembly mechanism of growing crystals [46].

2.4 CIE colorimetric system

In 1931 in an effort to relate the observed wavelengths of visible spectrum to the real colors which are perceived by human eye, CIE XYZ color space was introduced by International Commission on Illumination also known as the CIE from its French title, the Commission Internationale de l´Eclairage. CIE XYZ color space has been based on the fundamental experiments [70,71] which have been conducted by William David Wrigh and John Guild in late 1920s. XYZ values which are called tristimulus values can be calculated from the following equations:

$$X = \int_{380}^{780} P(\lambda)\bar{x}(\lambda)d\,\lambda$$

$$Y = \int_{380}^{780} P(\lambda)\bar{z}(\lambda)d\,\lambda$$

$$Z = \int_{380}^{780} P(\lambda)\bar{z}(\lambda)d\,\lambda$$

And $\bar{x}(\lambda)$, $\bar{y}(\lambda)$, and $\bar{z}(\lambda)$ are the spectral stimulus values which can be determined empirically.

The values of the X, Y and Z are used to calculated x and y which are called chromaticity coordinates. Chromaticity coordinates can be obtained from following equations:

$$x = \frac{X}{X + Y + Z}$$

$$y = \frac{Y}{X + Y + Z}$$

Chromaticity coordinates (x,y) are used to specify the color of perceived light by human eye in the CIE chromaticity diagram (**Figure 17**).

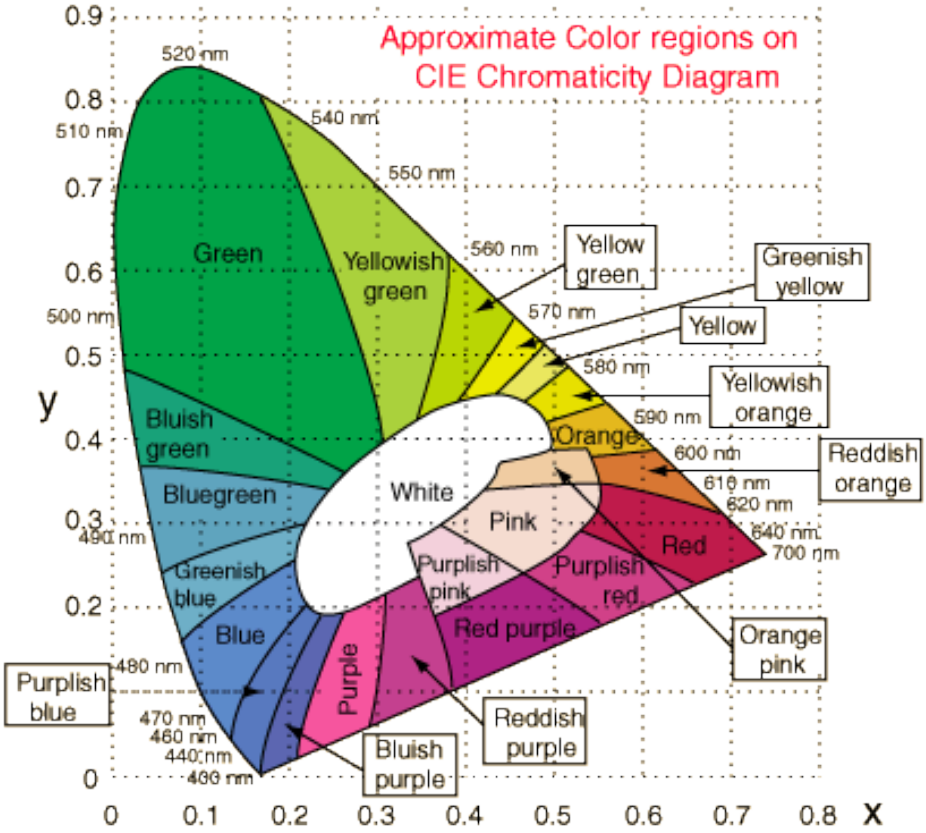

Figure 17. CIE Chromaticity Diagram [72].

CHAPTER 3

RESULT AND DISCUSSION

3.1 Powder X-Ray diffraction

3.1.1 XRD results of Dy, Tb and Sm doped LaBO3

Figure 18 demonstrates the powder x-ray diffraction patterns of Dy doped $LaBO_3$ samples. XRD patterns of undoped, 2.5% and 5% doped samples indicate single-phase crystalline materials .Their diffraction peaks match quite well with hkl values of orthorhombic $LaBO_3$ (JCPDS card no: 12-0762). The indexing procedure was conducted by doing search-match based on the diffraction date provided by the Joint Committee on Powder Diffraction Standards (JCPDS).

Moreover, the absence of any other peak indicates that incorporation of Dy^{3+} ions inside the host lattice of $LaBO_3$ has been implemented successfully. However, when the concentration of dopant (Dy) increases to 7.5% some new peaks appear in the XRD pattern. These extra peaks refer to the formation of impurities in the sample. XRD results of these samples have been presented in APPENDIX B.

The formation of impurity phases at high concentration of doping can be explained by the fact that, although both $DyBO_3$ and $LaBO_3$ compounds belong to orthoborate category of materials, borate structure is totally different in their crystals. While $LaBO_3$ favors trigonal planar borate structure (BO_3^{3-}), $DyBO_3$ favors tetrahedral ring structure of borate anion ($B_3O_9^{9-}$).

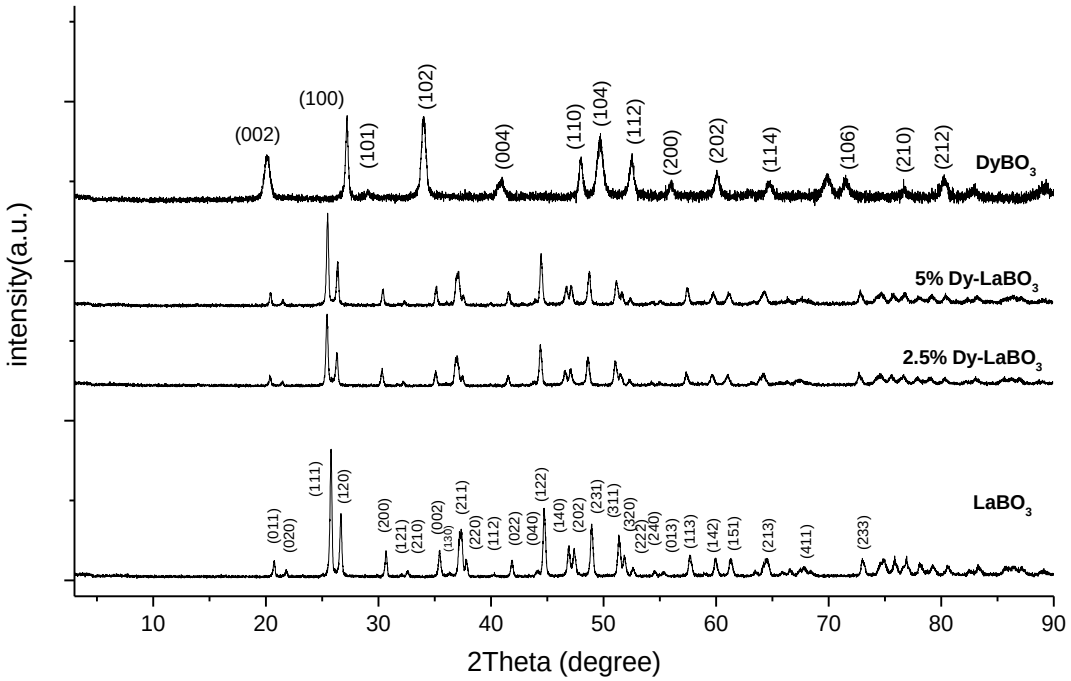

Figure 18. X-ray Diffraction pattern of undoped and Dy doped $LaBO_3$ orthoborates.

Figure 19 represents the XRD pattern of Tb doped $LaBO_3$ orthoborate samples. As it can be seen, undoped, 2.5, 5, 6 and 7% Tb doped samples exhibit diffraction patterns which can be indexed according to hkl values of orthorhombic $LaBO_3$ orthoborate (JCPDS card no: 12-0762). When doping concentration reaches to 7.5% some impurities appear in the sample. XRD results of those samples have been presented in APPENDIX B.

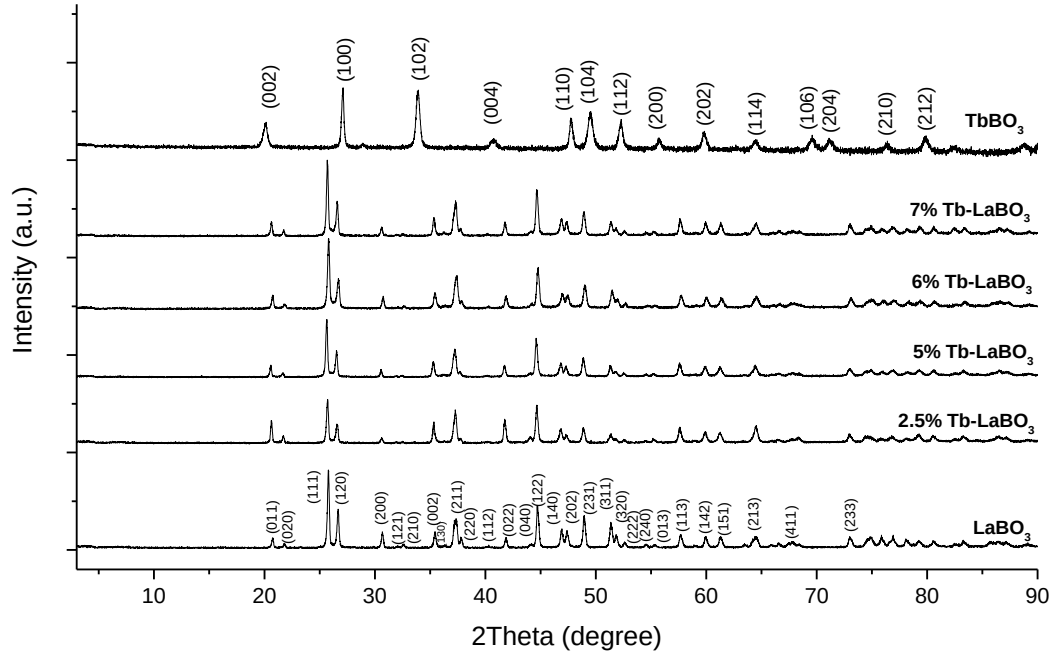

Figure 19. X-ray Diffraction pattern of undoped and Tb doped $LaBO_3$ orthoborates.

The results of X-ray diffraction analysis of Sm doped $LaBO_3$ samples is illustrated in **Figure 20**. based on XRD analysis it can be observed that undoped, 2.5%, 5% and 7.5% Sm doped samples were synthesized properly because their XRD pattern and assigned hkl values match well with the reference JCPDS card no: 12-0762. XRD analysis reveals the effect of doping on the crystal structure of produced materials. It can be seen that by increasing the amount of doping, XRD peaks of the materials have broadened. That is clearly obvious in the 7.5% doped sample. By exceeding the amount of doping beyond 7.5% the change becomes more significant. XRD results of those samples can be found in APPENDIX B. The different behavior of Sm doped samples in XRD analysis is due to usage of different material as the Sm socurse in the synthesis part. We used Sm_2O_3 as the Sm source while for Tb and Dy we used $TbCl_3$ and $DyCl_3$.

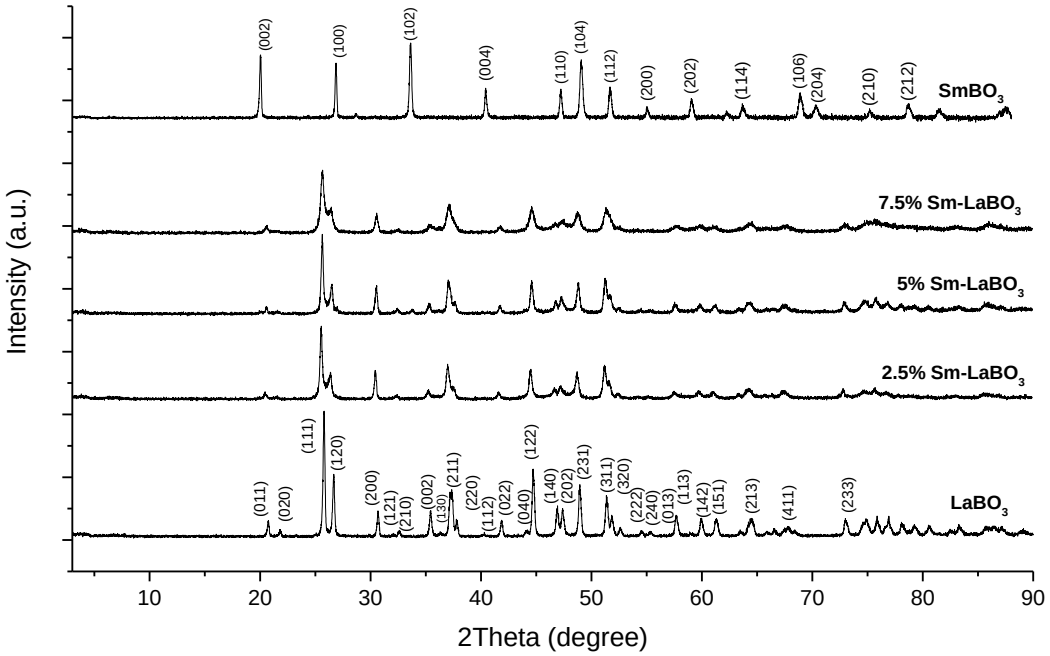

Figure 20. X-ray Diffraction pattern of undoped and Sm doped $LaBO_3$ orthoborates.

3.1.2 XRD results of Dy, Tb and Sm doped $GdBO_3$

Figure 21 represents XRD analysis of Dy doped $GdBO_3$ samples. As obviously can be seen from the XRD patterns, all prepared samples were produced properly because obtained diffraction peaks agree well with the pattern of hexagonal $GdBO_3$ (JCPDS card No:13-0483).

Moreover, in contrast with Dy doped $LaBO_3$ orthoborates where high concentration of dopant had resulted in crystal structure perturbation caused by impurity, in $GdBO_3$ case, as the XRD results show, by increasing the amount of dopant no significant change has been inspected in crystal structure of samples. The reason behind distinct behavior of $GdBO_3$ compared with $LaBO_3$ might be due to their different crystal system. $LaBO_3$ adapts orthorhombic crystal system while $GdBO_3$ has hexagonal crystal system. In addition, $DyBO_3$ has the same crystal system as $GdBO_3$; therefore, when Gd^{3+} ions are replaced by Dy^{3+} ions, the compatibility of two similar structure are much higher than two different structure.

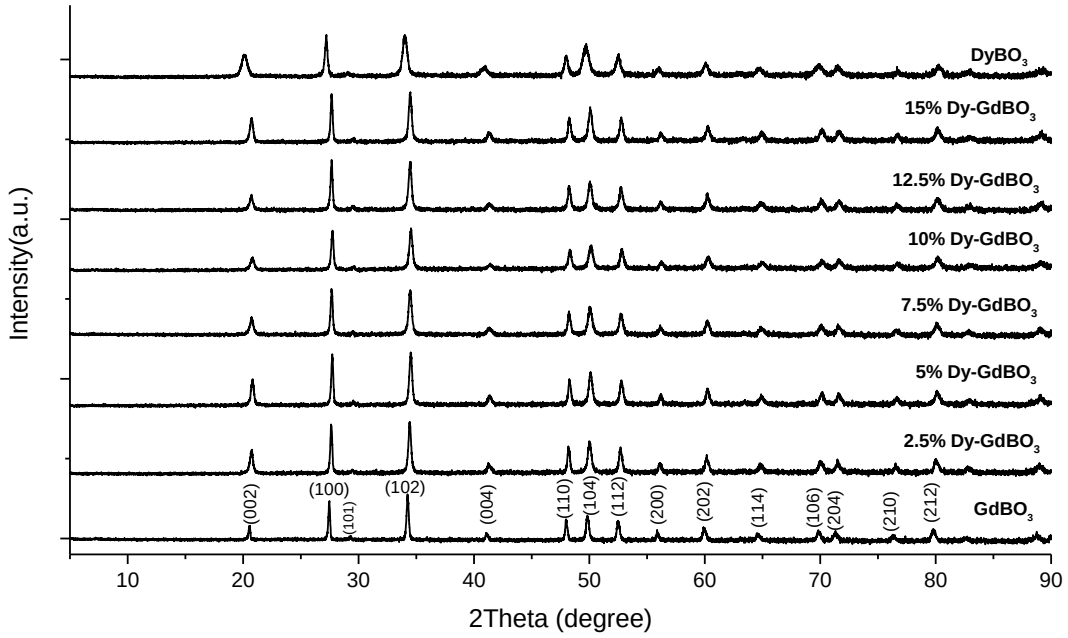

Figure 21. X-ray Diffraction pattern of undoped and Dy doped $GdBO_3$ orthoborates.

X-ray diffraction results of Tb doped $GdBO_3$ orthoborate samples are presented in **Figure 22**. As it obviously can be observed from the XRD patterns of prepared materials, doping procedure has not been caused any remarkable change on the crystal structure of the host $GdBO_3$. All of the observed diffraction peaks can be indexed according to hkl values of hexagonal GdBO3 orthoborate (JCPDS card No: 13-0483).Moreover, in contrast with Tb doped $LaBO_3$ orthoborates where high concentration of dopant caused structurale perturbation, in $GdBO_3$ case, as the XRD results show, by increasing the amount of dopant no significant change is inspected in the crystal structure of samples. The reason behind distinct behavior of $GdBO_3$ compared with $LaBO_3$ might be due to their different crystal system. $LaBO_3$ adapts orthorhombic crystal system while $GdBO_3$ has hexagonal crystal system. In addition, $TbBO_3$ has the same crystal system as $GdBO_3$; therefore, when Gd^{3+} ions are replaced by Tb^{3+} ions, the compatibility of two similar structure are much higher than two different structure.

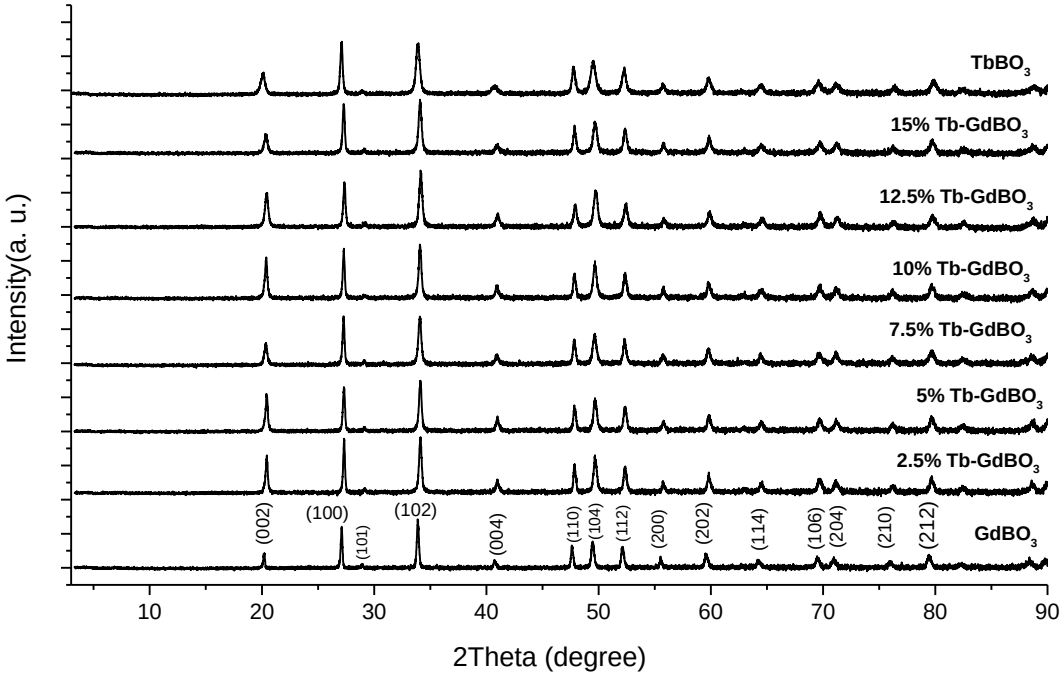

Figure 22. X-ray Diffraction pattern of undoped and Tb doped $GdBO_3$ orthoborates.

XRD analysis of Sm doped $GdBO_3$ orthoborates which is presented in the **Figure 23** shows that all prepared samples were produced properly as their obtained diffraction peaks are in good agreement with the JCPDS card No:13-0483. Additionally, contrary to Sm doped $LaBO_3$ orthoborates where high concentration of dopant caused formation of $La(OH)_3$ as impurity, in $GdBO_3$ case, as the XRD results show, by increasing the amount of dopant no significant change is inspected in the crystal structure of samples. The reason behind this distinct behavior of $GdBO_3$ compared with $LaBO_3$ might be due to their different crystal system. $LaBO_3$ has orthorhombic crystal system (aragonite-type structure) while $GdBO_3$ has hexagonal crystal system (vaterite-type phase). On the other hand, $SmBO_3$ has the same crystal system as $GdBO_3$ (both are vaterite-type phase); therefore, by doping Sm^{3+} ions in the GdBO3 host, two vaterite-type structure become compatible with each other.

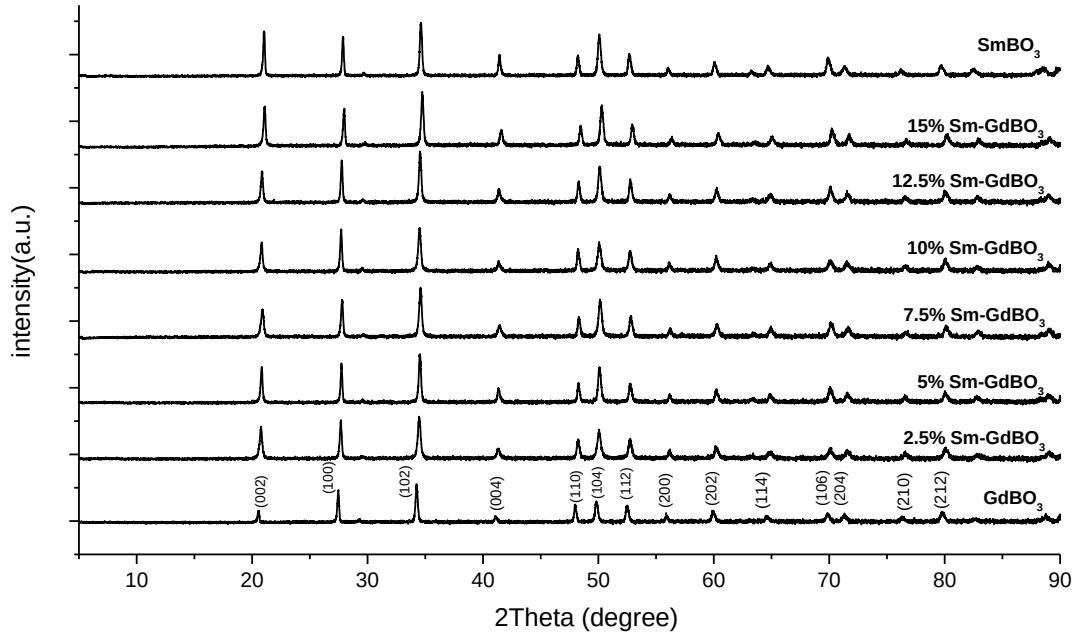

Figure 23. X-ray Diffraction pattern of undoped and Sm doped $GdBO_3$ orthoborates.

3.2 FT-IR

3.2.1 FT-IR results of Dy, Tb and Sm doped $LaBO_3$

IR spectra of Dy doped $LaBO_3$ samples are illustrated in **Figure 24**. ATR-IR spectroscopy of the 2.5 and 5% Dy doped $LaBO_3$ samples shows different stretching and bending modes of the borate anion. The broad band centered at around 1254 cm^{-1} can be assigned to asymmetric stretching of BO_3^{3-}. The peak at 939cm^{-1} originates from the symmetric stretching of BO_3^{3-} anion. The peaks at 698 cm^{-1} and 610 cm^{-1} are due to out-of-plane and in-plane bending of BO_3^3 anion, respectively. All peaks match well with characteristic absorption bands of trigonal planar borate anion; therefore, the results of IR analysis and XRD are in good correlation with each other.

IR spectra of prepared samples confirm that $La(OH)_3$, which were produced during the synthesis procedure, are completely converted to $LaBO_3$ because in the case of any presence of O-H bond, there would be a sharp peaks at 3600 cm^{-1} and 3400 cm^{-1}.

IR analysis also shows that by increasing the dopant concentration, absorption bands of once planar borate anion begin to deform. The 7.5% doped sample exhibits a hint

of distortion by a peak at 1178 cm^{-1}. Moreover, in 3500 cm^{-1} there is a band which can be ascribed to small amount of free and bonded O-H groups. This observation is correlated with the XRD analysis which indicates $La(OH)_3$ peaks as impurity in XRD pattern. By continuing the process of doping, trigonal planar borate anion structure totally disappears.

As it is obvious from the IR spectra there is a substantial difference between borate structure in $DyBO_3$ and $LaBO_3$. It is also shown that despite the distortion of planar structure of borate anion in high doping concentration, it never reaches the tetrahedral ring structure of borate prevailing in $DyBO_3$ compound.

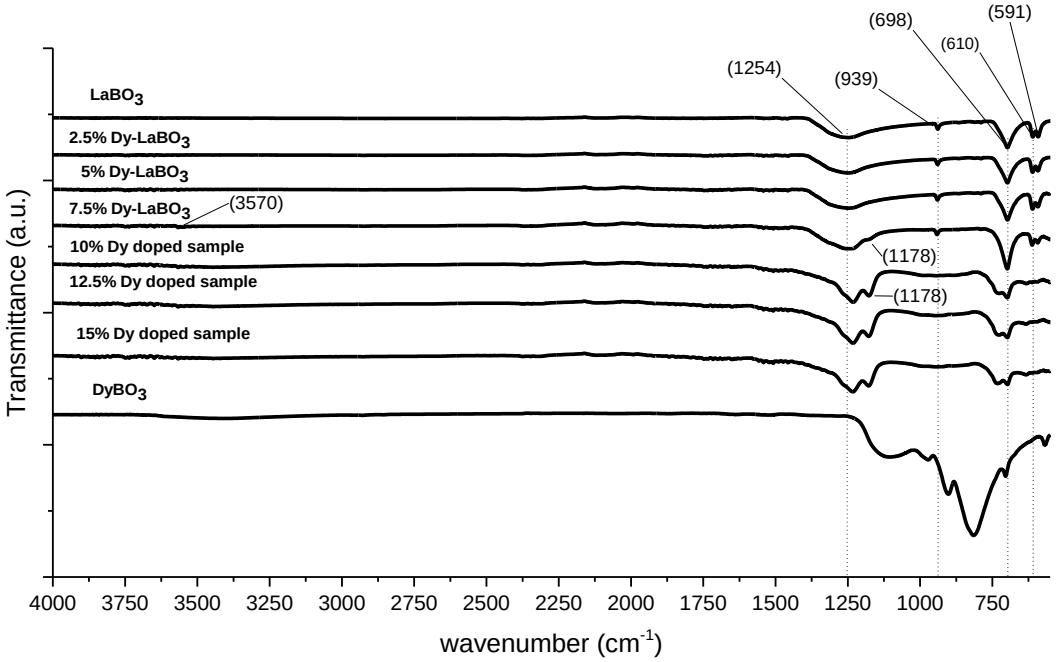

Figure 24. ATR-IR spectra of undoped and Dy doped $LaBO_3$ orthoborates.

Results of ATR-IR analysis of Tb doped samples are represented in **Figure 25**. IR spectra of as-obtained samples reveals the absorption band of various stretching and bending modes of trigonal planar borate. The broad band centered at around 1256 cm^{-1} can be attributed to asymmetric stretching of BO_3^{3-}. The peak at 940 cm^{-1} is related

to the symmetric stretching of BO_3^{3-} anion. The peaks at 700 cm^{-1} and 610 cm^{-1} are originated from out-of-plane and in-plane bending of BO_3^{3-} anion, respectively.

As it can be seen from the IR spectra of produced samples, when the concentration of doping reaches to 7.5%, trigonal planar structure of borate starts to change. The absorption peak at 1175 cm^{-1} is an indication of borate structure change. In addition to deformation of borate, there is a band at around 3556 cm^{-1}, originated from O-H bond of $La(OH)_3$, which shows the formation of impurities. These observations are quite in accordance with XRD results.

IR spectra of $TbBO_3$ illustrate the fundamental difference between its absorption bands and Tb doped $LaBO_3$ samples. It can also be seen that although high concentration doping (above 7.5-10%) causes trigonal planar borate to disappear, however, it never reaches the tetrahedral ring structure of $TbBO_3$.

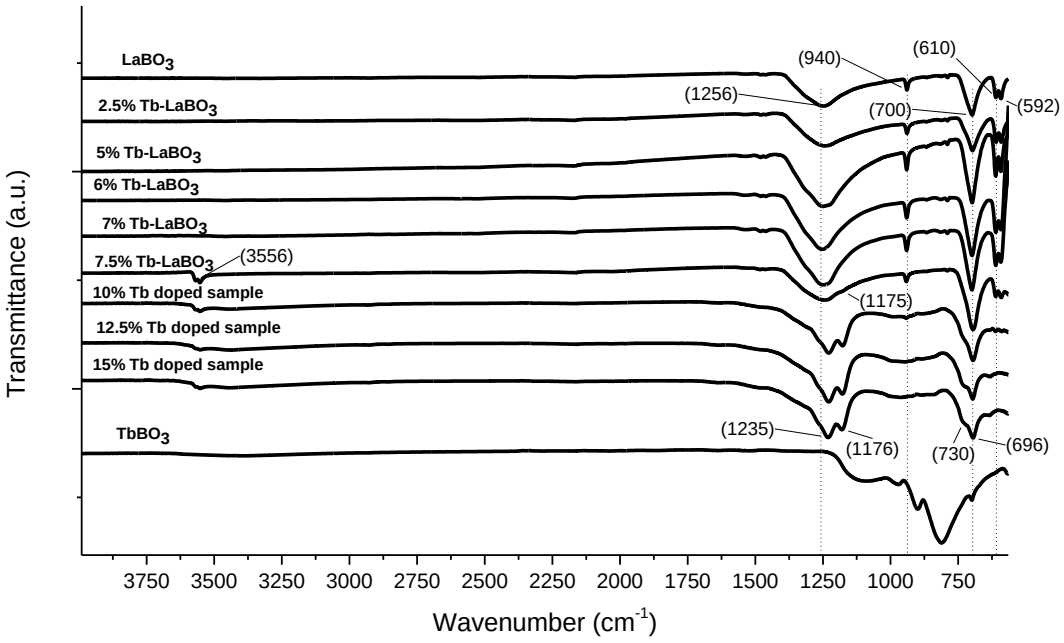

Figure 25. ATR-IR spectra of undoped and Tb doped LaBO3 orthoborates.

ATR-IR analysis of prepared Sm doped $LaBO_3$ samples exhibit typical absorption band of planar BO_3^{3-} group (**Figure 26**). All of these bands can be ascribed to stretching and bending mode of planar BO_3^{3-}. The broad band centered at around 1256

cm^{-1} can be assigned to asymmetric stretching of BO_3^{3-}. The peak at 940 cm^{-1} originates from the symmetric stretching of BO_3^{3-} anion. The peaks at 698cm^{-1} and 610 cm^{-1} are due to out-of-plane and in-plane bending of BO_3^{3-} anion, respectively.

In 12.5% and 15% doped samples there is a week peak at 3563 cm^{-1} which originates from O-H group. This peak confirms the existence of $La(OH)_3$ compound in the 12.5 % and 15% Sm doped samples and agrees well with the results of XRD analysis.

According to result obtained from IR analysis we can see that doping with Sm has preserved planar BO_3 in all doping concentration.

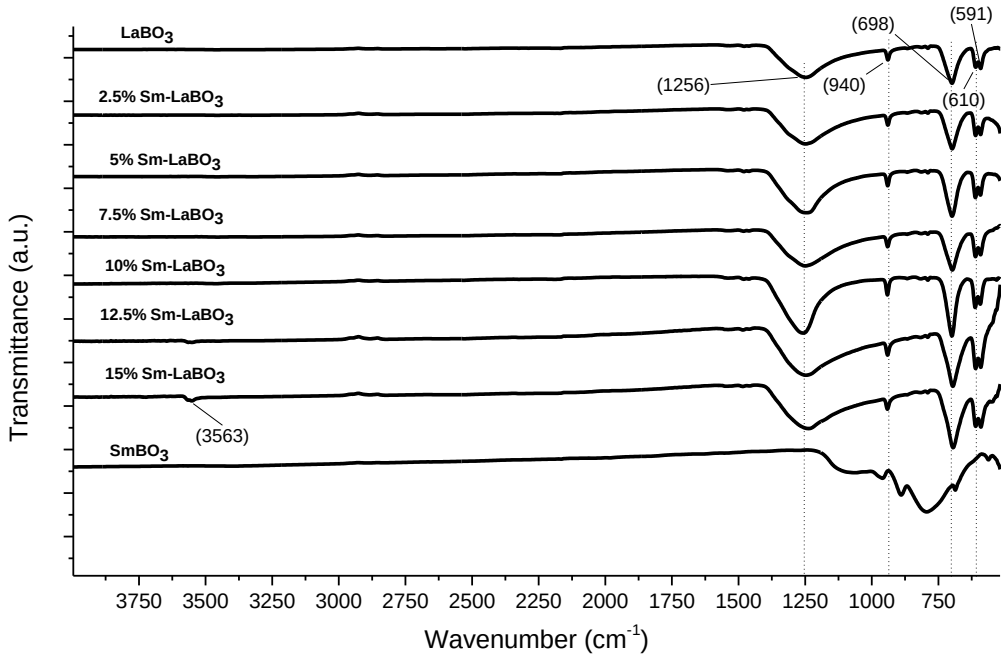

Figure 26. ATR-IR spectra of undoped and Sm doped LaBO3 orthoborates.

3.2.2 FT-IR results of Dy, Tb and Sm doped $GdBO_3$

ATR-IR analysis of Dy doped $GdBO_3$ samples (**Figure 27**) shows typical absorption bands of $B_3O_9^{9-}$ group. $B_3O_9^{9-}$ group, which is consist of BO_4 tetrahedral units, gives rise to six fundamental vibrational modes at 1105, 975, 906, 814, 704 and 568 cm^{-1}. The bands centered at 1105, 975, 906, 814 cm^{-1} originate from stretching mode of

$B_3O_9^{9-}$ groups. Bending modes of $B_3O_9^{9-}$ groups engender absorption bands centered at 704 and 568 cm^{-1}. FT-IR results also obviously confirm that borate structure in $GdBO_3$ and $DyBO_3$ is identical, because they have same absorption bands. Moreover, looking at the results of IR analysis, it can be seen that doping procedure is not resulted in any significant difference between undoped and doped materials. This observation is in good agreement with the results of XRD analysis, too.

According to IR analysis of Dy doped $GdBO_3$, $Gd(OH)_3$ colloids which were generated during first stage of synthesis, are completely converted to $GdBO_3$ orthoborate because there is no peak associable to O-H functional group. FT-IR results, in addition, agree pretty well with results of X-ray diffraction results.

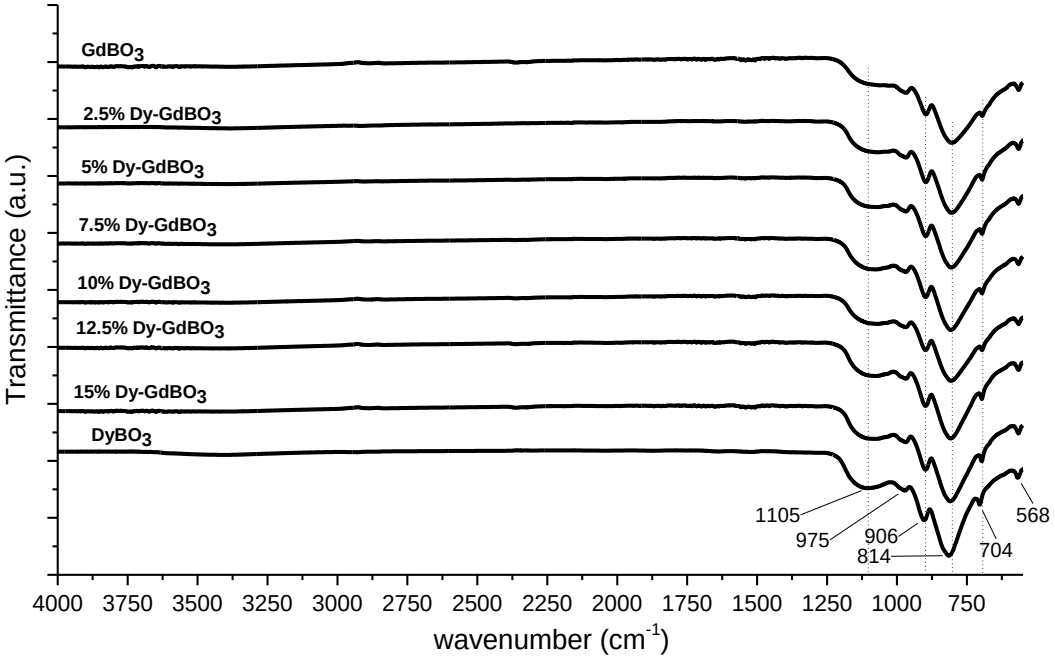

Figure 27. ATR-IR spectra of undoped and Dy doped $GdBO_3$ orthoborates.

Figure 28 demonstrates the IR spectra of Tb doped $GdBO_3$ samples. As it can be seen, there are six major absorption bands at 1140, 970, 900, 818, 697 and 566 cm^{-1} which all of them can be assigned to the vibrational modes of tetrahedral ring structure of borate ($B_3O_9^{9-}$). The bands centered at 1105, 974, 905, 818 cm^{-1} originate from

stretching mode of $B_3O_9^{9-}$ groups. The bands at 703 and 566 cm^{-1} can be attributed to the bending modes of $B_3O_9^{9-}$.

By comparing the IR spectra of Tb doped $GdBO_3$ samples and $TbBO_3$, it can be seen that there is not noticeable difference between them. This observation is correlated with the results of XRD analysis. FT-IR results also obviously confirm that borate structure in $GdBO_3$ and $TbBO_3$ is identical, because they have same absorption bands.

According to IR analysis, $Gd(OH)_3$ collides which were generated during first stage of synthesis, are completely converted to $GdBO_3$ orthoborate because there is not any peak assigned to O-H functional group.

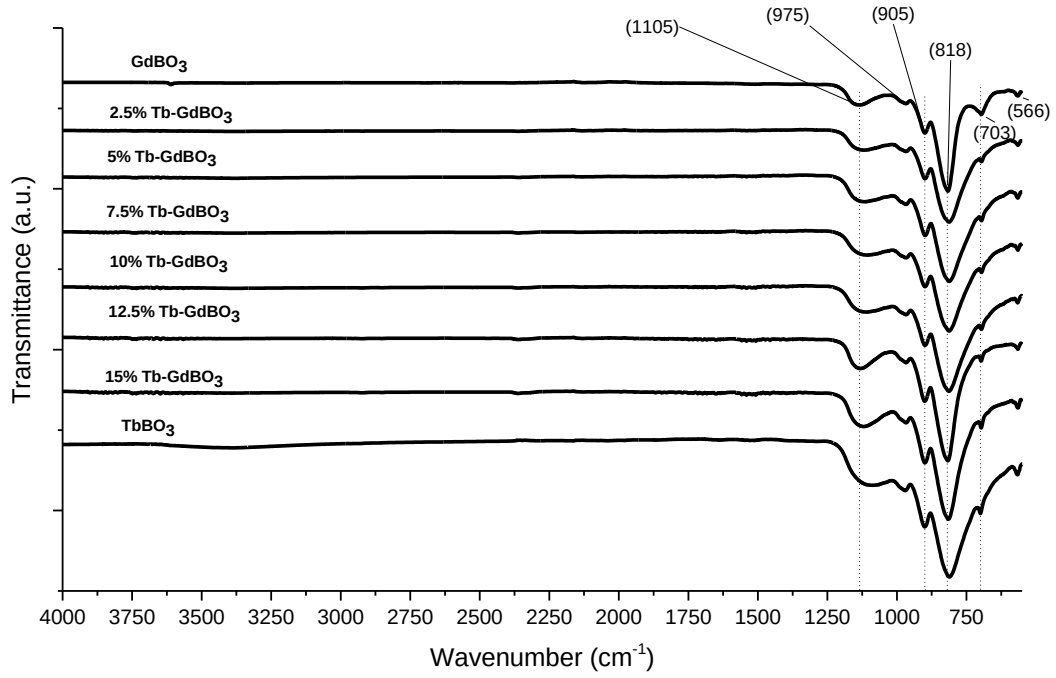

Figure 28. ATR-IR spectra of undoped and Tb doped $GdBO_3$ orthoborates.

Figure 29 shows the results of ATR-IR analysis of Sm doped $GdBO_3$ samples. As it can be seen there are six main absorption bands all of which can be attributed to the starching and bending modes of $B_3O_9^{9-}$ group which is made up of BO_4 tetrahedral units. The bands centered at 1105, 962, 886, 800 cm^{-1} originate from stretching mode

of $B_3O_9^{9-}$ groups. The bands at 687 and 564 cm^{-1} can be attributed to the bending modes of $B_3O_9^{9-}$.

FT-IR results also obviously confirm that borate structure in $GdBO_3$ and $SmBO_3$ is identical, as they show same absorbance bands.

According to IR analysis, $Gd(OH)_3$ colloids which were generated during first stage of synthesis, are completely converted to $GdBO_3$ orthoborate because there is not any peak assigned to O-H functional group. FT-IR results, in addition, agree well with results of X-ray diffraction results.

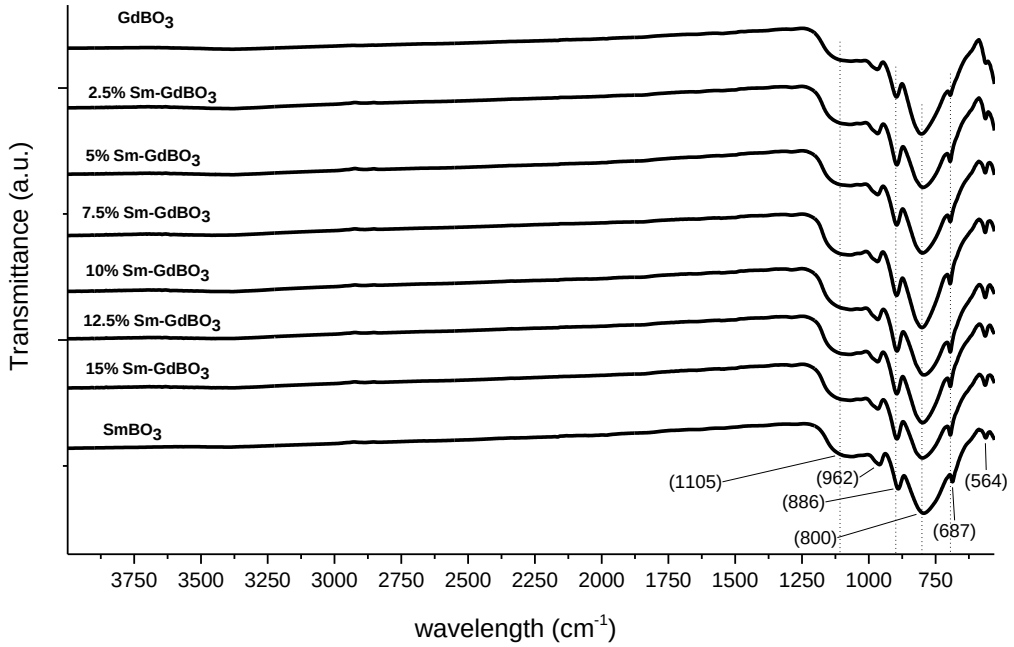

Figure 29. ATR-IR spectra of undoped and Sm doped $GdBO_3$ orthoborates.

3.3 FAR-IR

3.3.1 FAR-IR results of Dy, Tb and Sm doped $LaBO_3$

Far-IR spectroscopy is an effective technique in order to gain more insight into the material structure. According to literature, it is well stablished that in $LaBO_3$ crystals each La^{3+} ion is coordinated with nine oxygen atoms. In order to identify IR absorption bands of La-O bond, IR spectroscopy of La_2O_3 was conducted in Far-IR region (Appendix A). It is observed that there are strong absorption bands in 100-500 cm^{-1}

range, which can only be attributed to the La-O bonds. Furthermore, FAR-IR analysis of prepared Dy doped orthoborate materials indicate clear bands in that region, so it can be concluded that those distinct and noticeable bands at 300, 205 and 168 cm^{-1} might be assigned to the stretching and bending modes of La-O network structure. The peaks at 611 and 590 cm^{-1} rise from the in-plane bending mode of BO_3^{3-} anion which had been observed in ATR-IR, as well.

Moreover, it is possible to say that due to similarity of spectra of undoped, 2.5 and 5% doped samples, Dy^{3+} ions may preferentially acquire lattice points rather than residing in the holes. When dopant concentration reaches to 7.5% and beyond, IR spectra shows some hints of new absorption band (at 526, 427 and 140 cm^{-1}) and tendency toward new metal-oxygen structure, probably due to the distortions caused by the large interstitial Dy^{3+} ions.

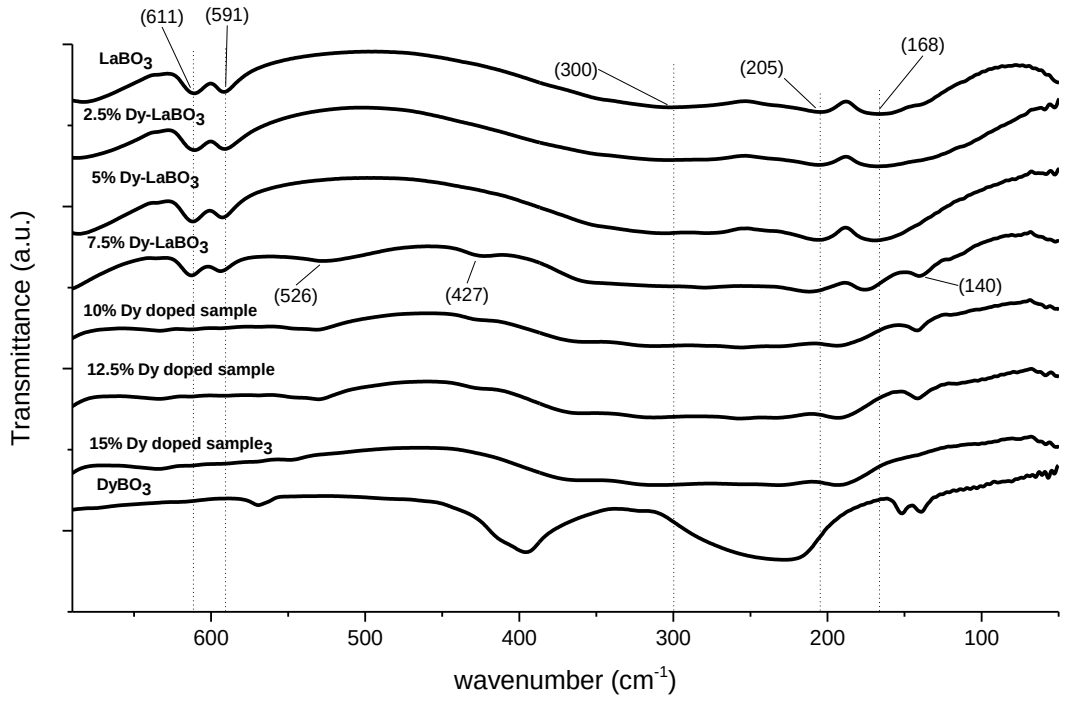

Figure 30. FAR-IR spectra of undoped and Dy doped $LaBO_3$ orthoborates.

Figure 31 shows the FAR-IR spectra of Tb doped $LaBO_3$ samples. As it has been explained in the Dy doped $LaBO_3$ section, the peaks at 302, 206 and 170 cm^{-1} can be

attributed to the bending and stretching modes of La-O network structure. The peaks centered at 612 and 591 cm^{-1} are due to the in-plane bending mode of BO_3^{3-} anion. These peaks had been observed in ATR-IR analysis, too.

FAR-IR spectra of undoped, 2.5 and 5% doped samples exhibit the same absorption bands suggesting that doped Tb^{3+} ions have been settled in the lattice points by replacing Dy^{3+} ions instead of residing in the holes. However when the concentration of doping reaches to 7.5% and more than that amount some new bands appear at the FAR-IR spectra (at 528, 428 and 142cm^{-1}) this might be due to the distortions caused by the large amount of interstitial Dy^{3+} ions.

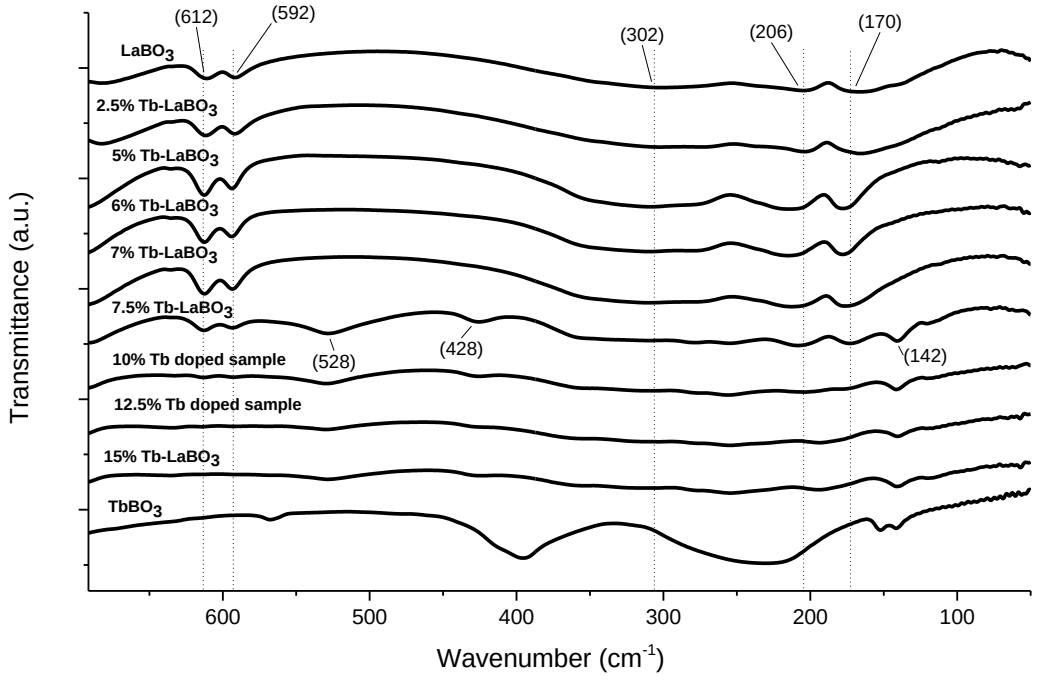

Figure 31. FAR-IR spectra of undoped and Tb doped LaBO3 orthoborates.

Figure 32 demonstrates the FAR-IR analysis of Sm doped $LaBO_3$ samples in the 50-690 cm^{-1} range. As it has been discussed in the Dy and Tb doped $LaBO_3$ section, the observed bands in 300, 205 and 170 cm^{-1} can be assigned to the streching and bending modes of La-O network structure. By looking at the different absorption bands of undoped, 2.5, 5 and 7.5% Sm doped $LaBO_3$, it can be seen that doping precedure leads to no significant change on the main absorption band of Sm doped $LaBO_3$ samples.

However when the doping concentration goes above 7.5%, some alterations can be observed. In 7.5, 10 and 15% Sm doepd $LaBO_3$ samples a broad sholder can be seen in the 400-600 cm^{-1} region. This can be a sign of formation of new metal-oxygen bond or structure in high doping concentration. The comparison of Sm doped $LaBO_3$ samples with Dy and Tb doped samples shows that when $LaBO_3$ is doped with Sm its La-O stucture is much less affected. This abservation also can be verifed by the XRD and FT-IR analysis.

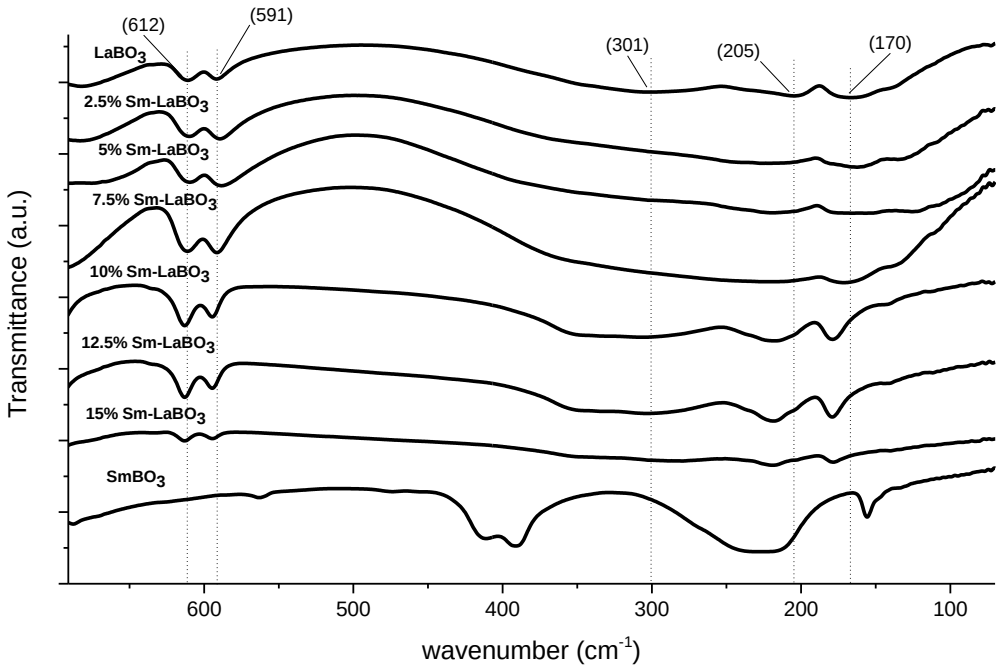

Figure 32. FAR-IR spectra of undoped and Sm doped $LaBO_3$ orthoborates.

3.3.2 FAR-IR results of Dy, Tb and Sm doped $GdBO_3$

FAR-IR spectroscopy of Dy doped $GdBO_3$ orthoborate samples is shown in **Figure 33.** FAR-IR spectra exhibits clear and distinct bands especially in the 600-100 cm^{-1} range. The band at 565 cm^{-1} can be ascribed to bending mode of tetrahedral BO_4 unit. The peaks centered at 394, 231 and 153 cm^{-1} might be attributed to bending and stretching modes of Gd-O network structure where each Gd^{3+} ion is coordinated with

eight Oxygen ions. FAR-IR analysis of Dy doped $GdBO_3$ samples reveals that doping procedure does not cause any noticeable change on the structure of doped samples.

The comparison of FAR-IR spectra of Dy doped $GbBO_3$ samples and $DyBO_3$ indicate that they have similar absorption bands. These observation are correlated with ATR-IR and XRD results, too.

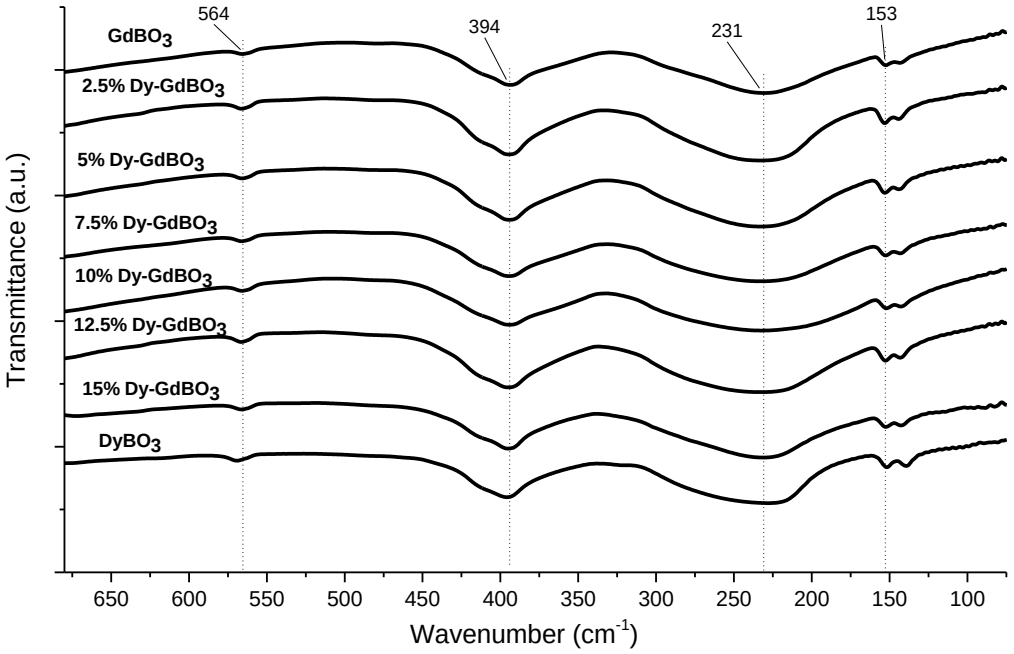

Figure 33. FAR-IR spectra of undoped and Dy doped $GdBO_3$ orthoborates.

Figure 34 illustrates the FAR-IR analysis of Tb doped $GdBO_3$ orthoborate samples. There are several absorption bands centered at 395, 232 and 152 cm^{-1}. The small band at 564 cm^{-1} can be assigned to the bending mode of tetrahedral BO_4 units. Other bands at 395, 232 and 152 cm^{-1}, as described in the Dy doped $GdBO_3$ part, originate from the stretching and bending modes of Gd-O network structure.

The comparison of spectra of undoped $GdBO_3$ with other samples doped by different amount of Tb indicates no remarkable variation between them suggesting that doping procedure does not lead to change on the structure of doped samples. Moreover, there is no significant difference between absorption bands of Tb doped samples and $TbBO_3$

orthoborate, too. This observation can be verified by the results of ATR-IR and XRD analysis.

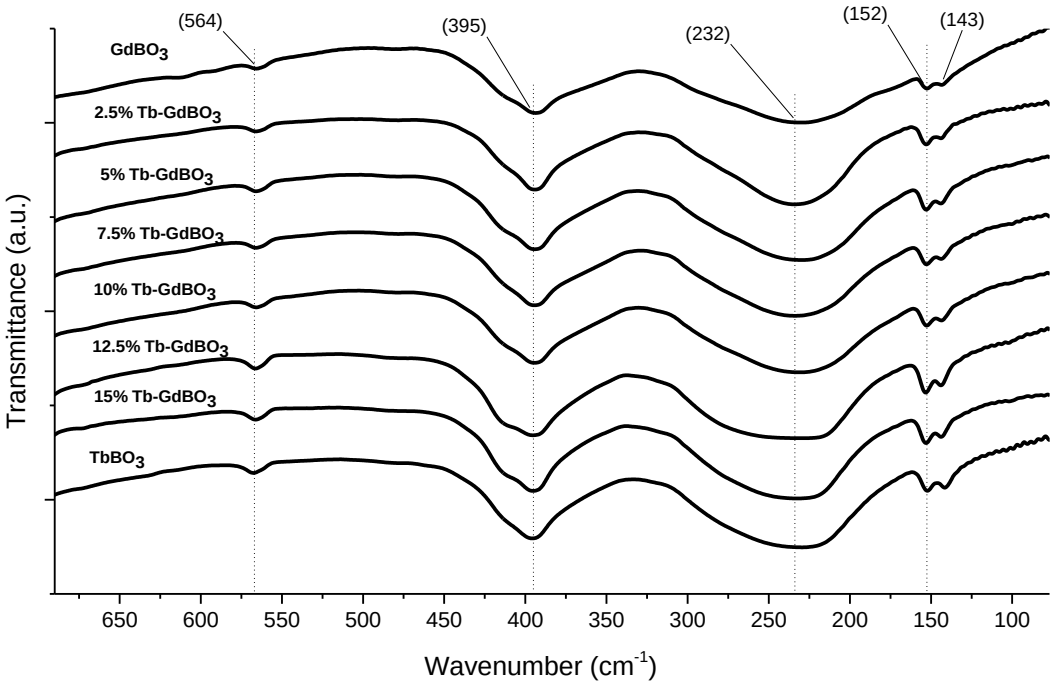

Figure 34. FAR-IR spectra of undoped and Tb doped $GdBO_3$ orthoborates.

Far-IR spectroscopy of Sm doped $GdBO_3$ samples are presented in **Figure 35**. As it can be obviously seen absorption bands of Sm doped samples in far IR region do not change remarkably. There are several broad bands at 395, 232, 152 and 142 cm^{-1} which can be assigned to various vibrational (stretching and bending) modes of Gd-O network structure as it has been discussed in Dy and Tb doped $GdBO_3$ section.

The comparison of FAR-IR spectra of Sm doped $GbBO_3$ and $SmBO_3$ samples show that they have similar absorption bands which indicates that Gd-O and Sm-O interactions are identical. These observations are correlated with ATR-IR and XRD results, too. In the ATR-IR analysis we observed that borate anion structure in the both Sm doped $GdBO_3$ samples and the $SmBO_3$ is in the form of $B_3O_9^{9-}$. XRD analysis, also, showed that diffraction patterns of Sm doped $GdBO_3$ samples and $SmBO_3$ are correspondent to vaterite-type structure.

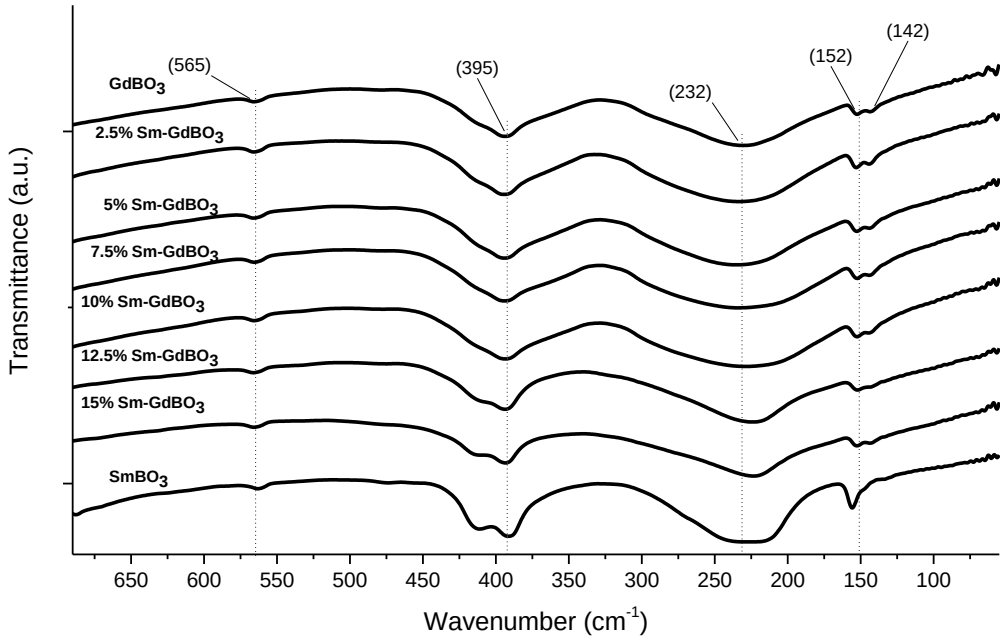

Figure 35. FAR-IR spectra of undoped and Sm doped $GdBO_3$ orthoborates.

3.4 Scanning Electron Microscopy (SEM) and EDX analysis

3.4.1 SEM and EDX results of Dy, Tb and Sm doped $LaBO_3$

In an effort to precisely investigate the shape and morphology of as-produced materials, SEM analysis of synthesized samples was carried out. SEM image (**Figure 36**) of $LaBO_3$, 5% Dy-$LaBO_3$ and 10% Dy-$LaBO_3$ clearly illustrate morphology of prepared samples. Undoped and 5% Dy doped samples show relatively large and easily definable geometric crystals. These particles are formed in the shape of self-assembled nano-bundles. SEM images show that particles of those samples have smooth surface with homogeneous distribution of particle size.

According to SEM images, the change in morphology of materials as a result of doping procedure, can be observed. While there is no significant change in the pariticle shape and morphology of 5% doped sample, 10% doped sample exhibits totally different morphology. It can be seen that 10% doped sample has lost the self-assembled nano bundle morphology which was highly preserved in 5% doped and undoped samples. Moreover, in contrast with undoped (**Figure 36a**) and 5% doped (**Figure 36b**) samples, 10% doped (**Figure 36c**) sample has rough surface. Based on XRD and IR

analysis, it was observed that 10% doped Dy sample has lost its crystal structure due to the high concentration of doping. SEM image also verifies the results obtained from XRD and IR analysis and agrees quiet well with them.

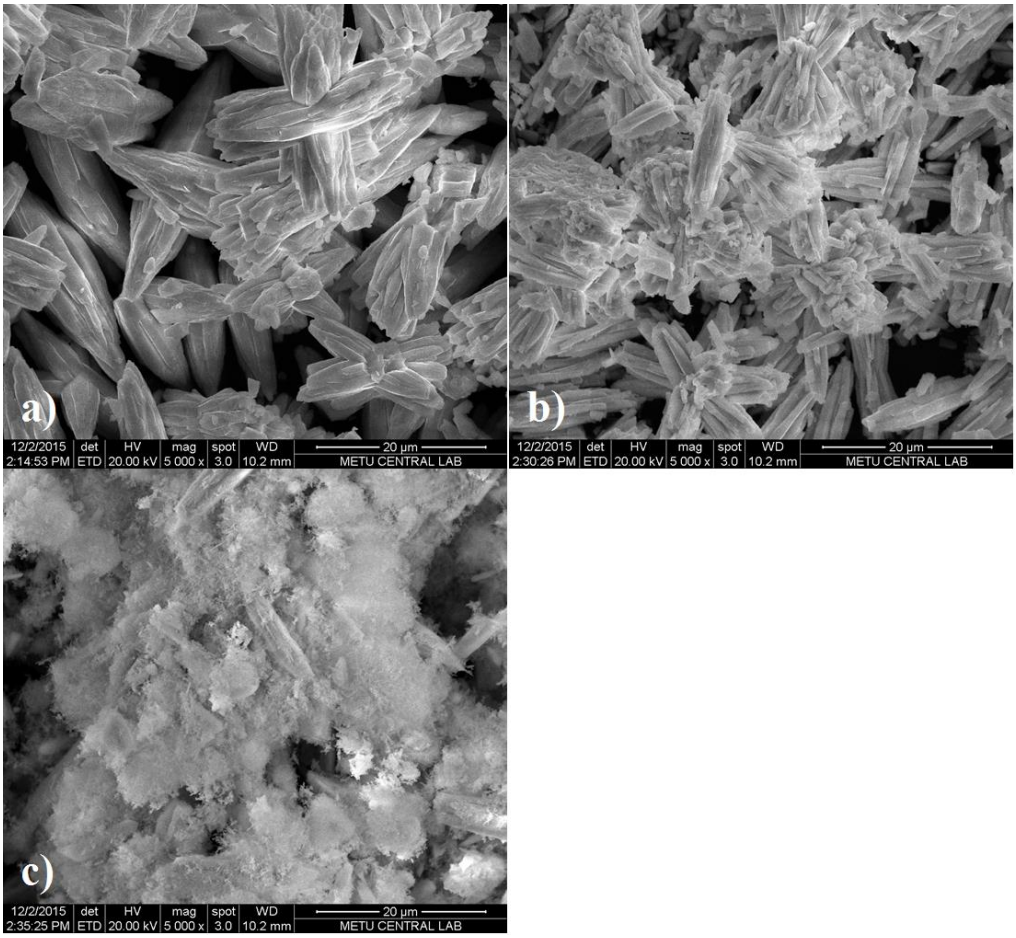

Figure 36. SEM images of a) undoped $LaBO_3$, b) 5% Dy doped $LaBO_3$, c) 10% Dy doped $LaBO_3$.

Figure 37 shows the results of EDX analysis of undoped, 5 and 10% Dy doped $LaBO_3$ samples. Existence of Dy in the 5 and 10% doped samples can be verified based on the EDX results. Moreover, EDX analysis of 10% Dy doped sample shows that there is a peak assigned to Cl element coming from the $LaCl_3$ and $DyCl_3$ impurities, which means that washing procedure in synthesis part was unsuccessful. In order to overcome

this we tried to wash samples with hot deionized water to remove those impurities however this approach did not work.

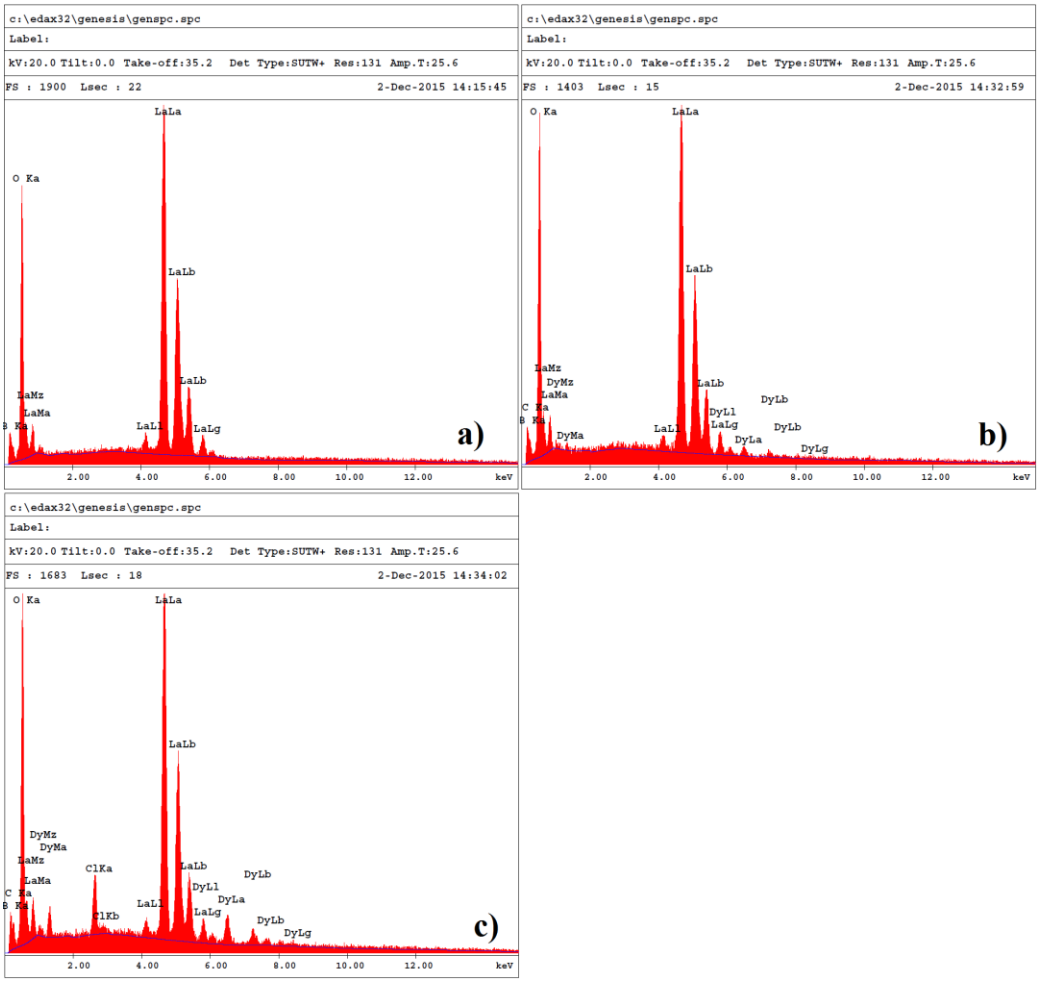

Figure 37. EDX spectra of a) undoped $LaBO_3$, b) 5% Dy doped $LaBO_3$, c) 10% Dy doped $LaBO_3$.

Figure 38 depicts the SEM analysis of Tb doped $LaBO_3$ samples. SEM images of 5 and 7.5 % Tb doped samples exhibit the same shape and geometry of particles. Moreover the comparison of Dy and Tb doped $LaBO_3$ samples shows that there is no remarkable difference between them. However when the amount of doping increases to 15% the morphology of the sample alters dramatically, it can be observed that the self-assembly structure of the particles totally fades out as it is shown in the XRD analysis.

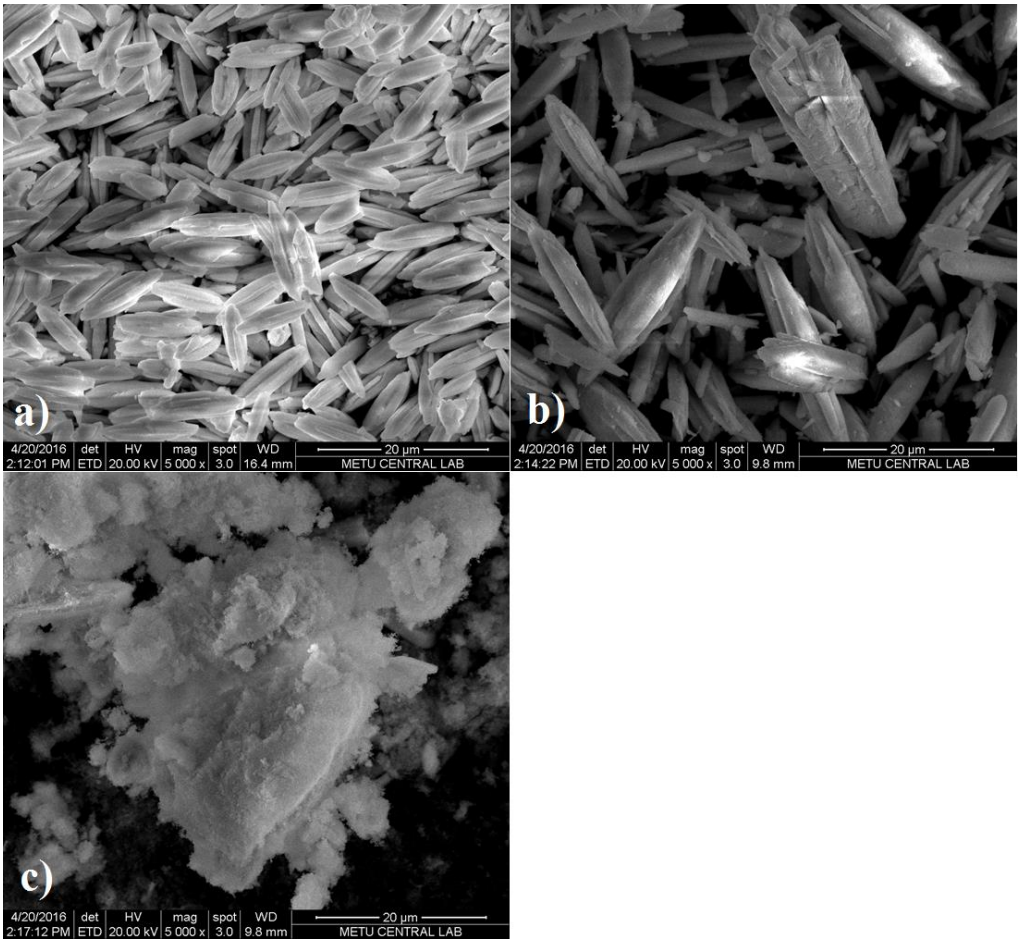

Figure 38. SEM images of a) 5% Tb doped $LaBO_3$, b) 7.5% Tb doped $LaBO_3$,c) 15% Tb doped $LaBO_3$.

EDX spectra of Tb doped $LaBO_3$ samples are presented in **Figure 39**. The peaks in the EDX spectra of 5, 7.5 and 15% Tb doped samples show the presence of Tb and La elements. Moreover, in 7.5 and 15% Tb doped samples, there is a peak assigned to the Cl element coming from the $LaCl_3$ and $TbCl_3$ impurities which is in accordance with the results of XRD analysis as well.

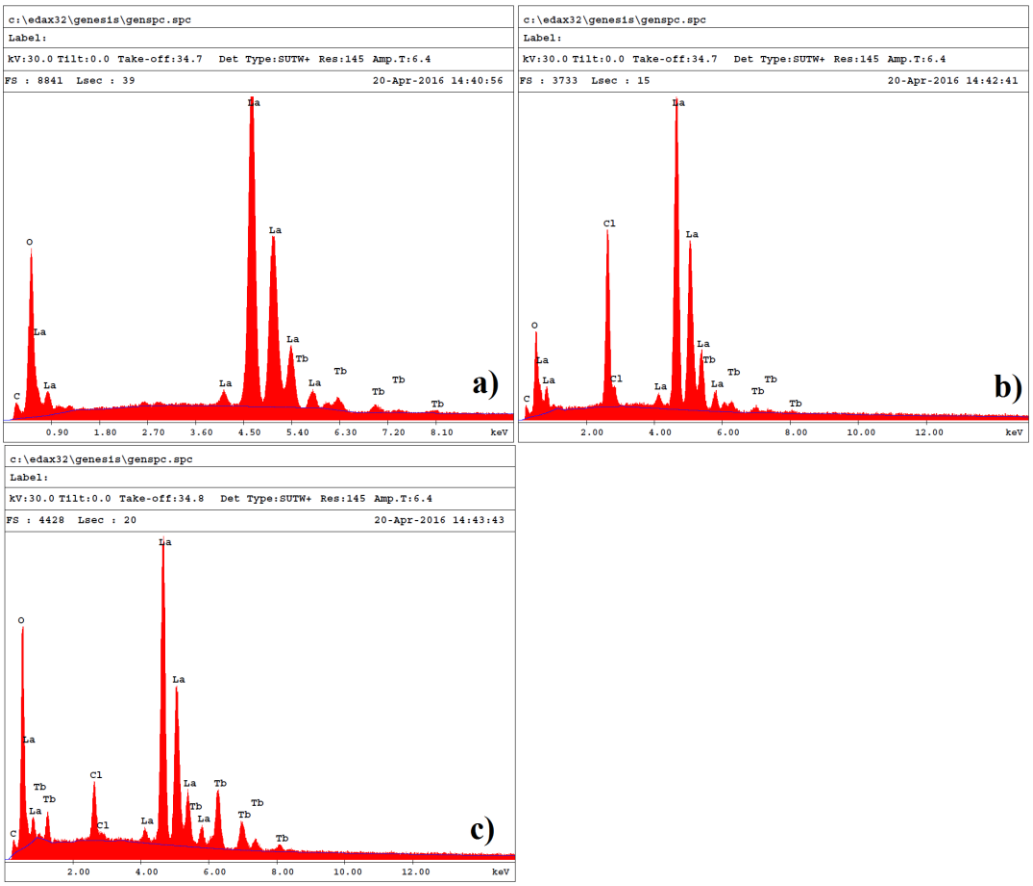

Figure 39. EDX spectra of a) 5% Tb doped $LaBO_3$, b) 7.5% Tb doped $LaBO_3$, c) 15% Tb doped $LaBO_3$.

Figure 40 illustrates the SEM images of $LaBO_3$ doped with various amounts of Sm. 5 and 7.5% Sm doped samples show quiet large and easily definable geometric crystals. These particles are formed in the cauliflower-like shapes consisted of self-assembled nano-bundles.

SEM images also show the change in morphology of materials as a result of doping procedure. While there is no significant difference between 5 and 7.5% doped samples, 10% doped sample exhibits totally different morphology. It can be seen that 10% doped sample has, completely, lost the morphology.

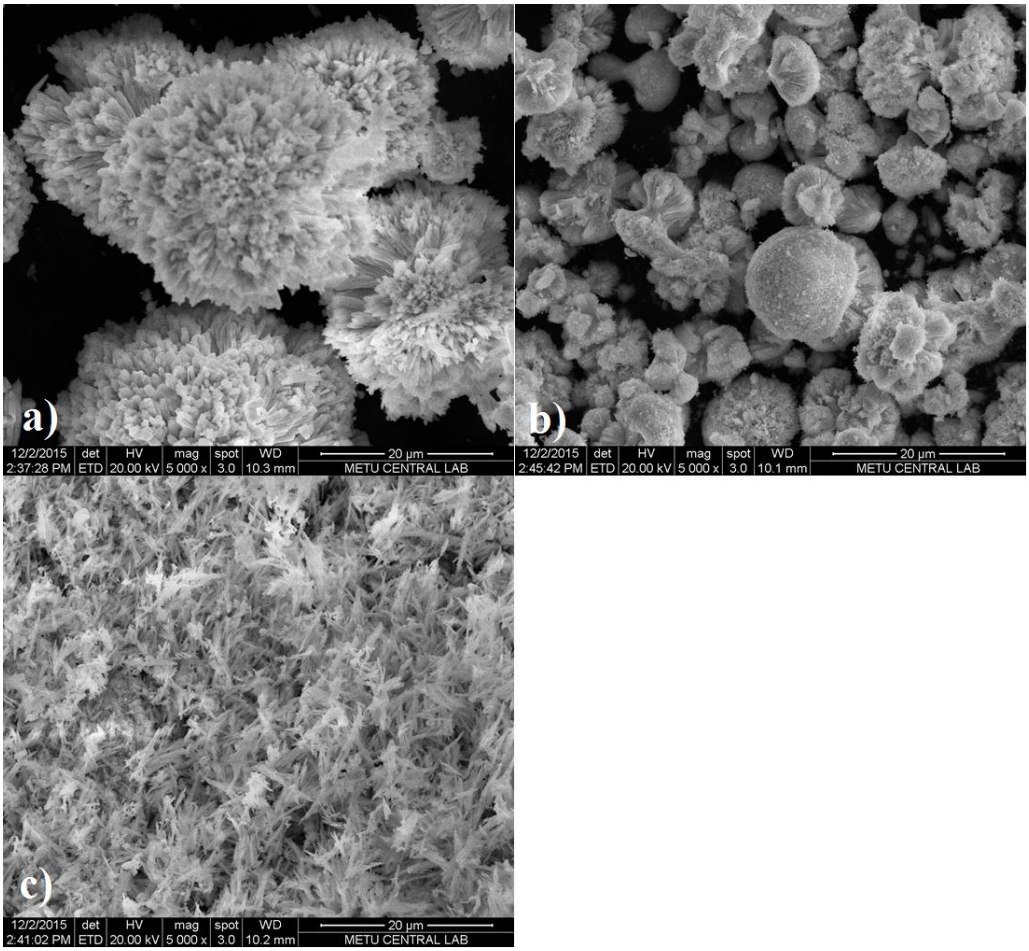

Figure 40. SEM images of a) 5% Sm doped $LaBO_3$, b) 7.5% Sm doped $LaBO_3$, c) 10% Sm doped $LaBO_3$.

EDX analysis results of Sm doped samples are presented in **Figure 41**. Based on the EDX results the presence of Sm and La elements can be confirmed.

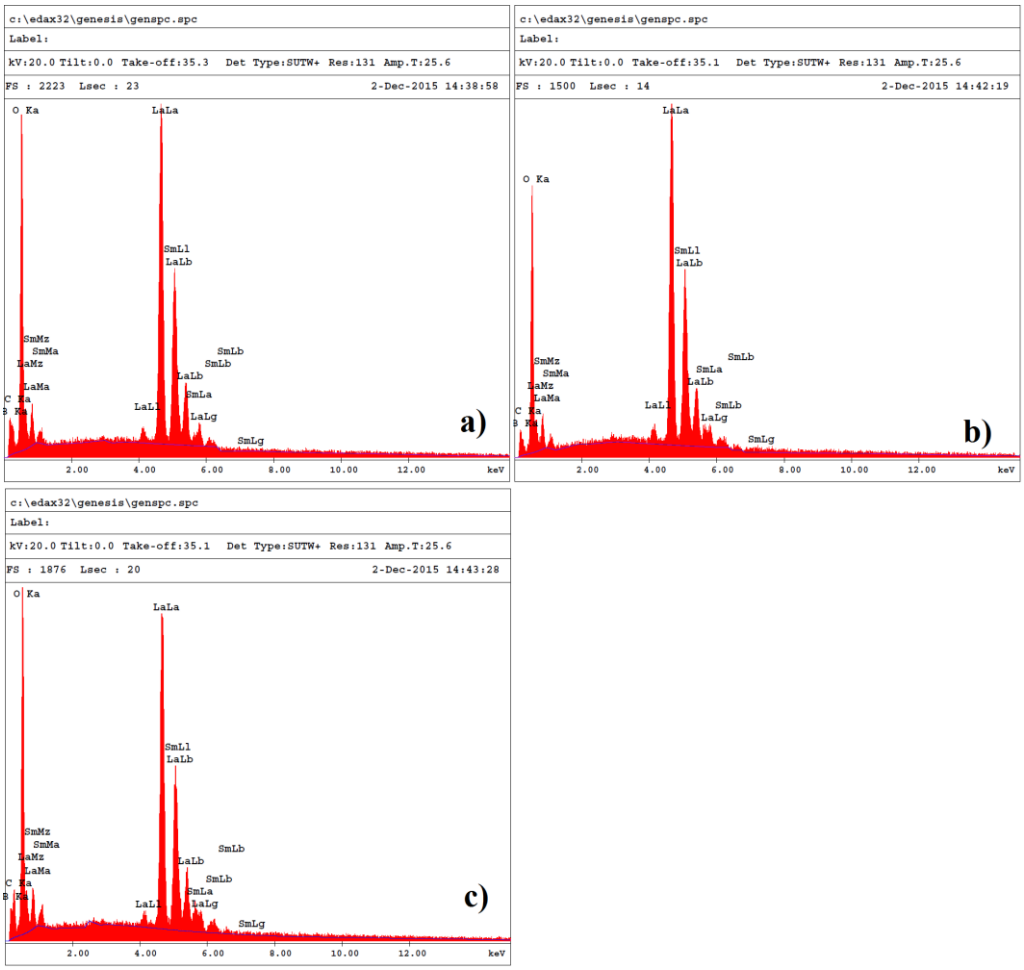

Figure 41. EDX spectra of a) 5% Sm doped $LaBO_3$, b) 7.5% Sm doped $LaBO_3$, c) 10% Sm doped $LaBO_3$.

3.4.2 SEM and EDX results of Dy, Tb and Sm doped $GdBO_3$

Figure 42 illustrates the SEM analysis of Dy doped $GdBO_3$ samples. It can be seen that the shape and geometry of Dy doped $GdBO_3$ particles are quite different from Dy doped $LaBO_3$ particles. Particles are in uniform and well-defined shapes formed as spherical self-assembled needles or plates. SEM images also show that doping process does not chang the shape and size of the obtained particles.

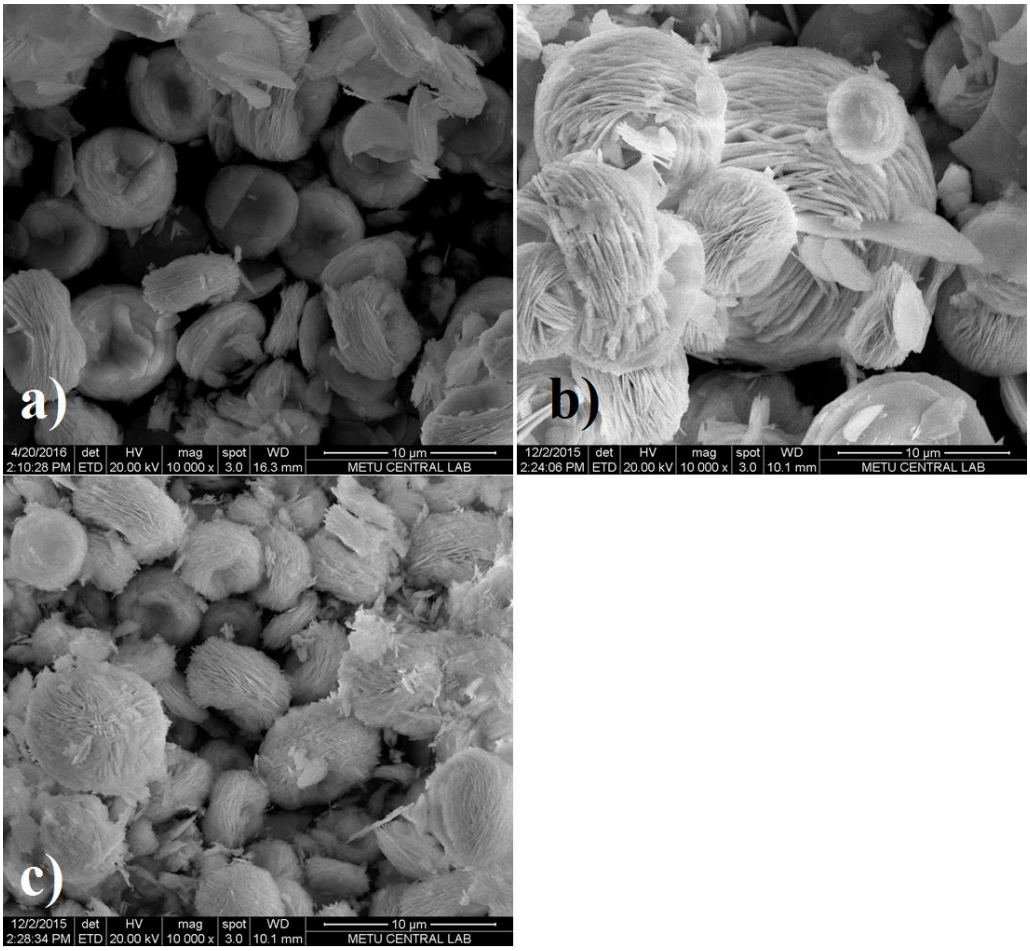

Figure 42. SEM images of a) undoped $GdBO_3$, b) 5% Dy doped $GdBO_3$, c) 7.5% Dy doped $GdBO_3$.

Figure 43 presents the results obtained from the EDX analysis of Dy doped $GdBO_3$ samples. According to the EDX spectra the presence of Dy and Gd elements can be confirmed.

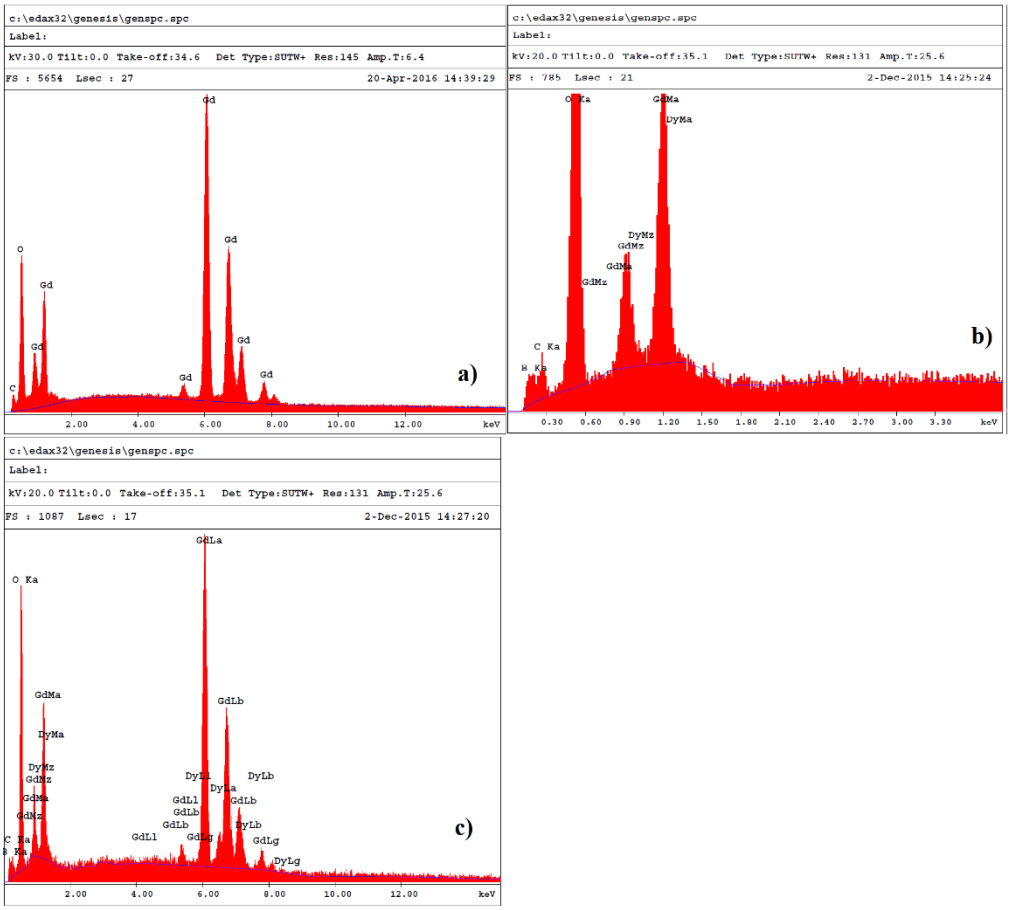

Figure 43. EDX spectra of a) undoped $GdBO_3$, b) 5% Dy doped $GdBO_3$, c) 7.5% Dy doped $GdBO_3$.

Figure 44 shows the SEM images of Tb doped $GdBO_3$ samples. According to SEM analysis the influence of doping on the shape of the materials can be observed. While 7.5 and 10% Tb doped samples exhibit spherical self-assembled particles, however, the sample with the 12.5 % Tb has lost its spherical shape.

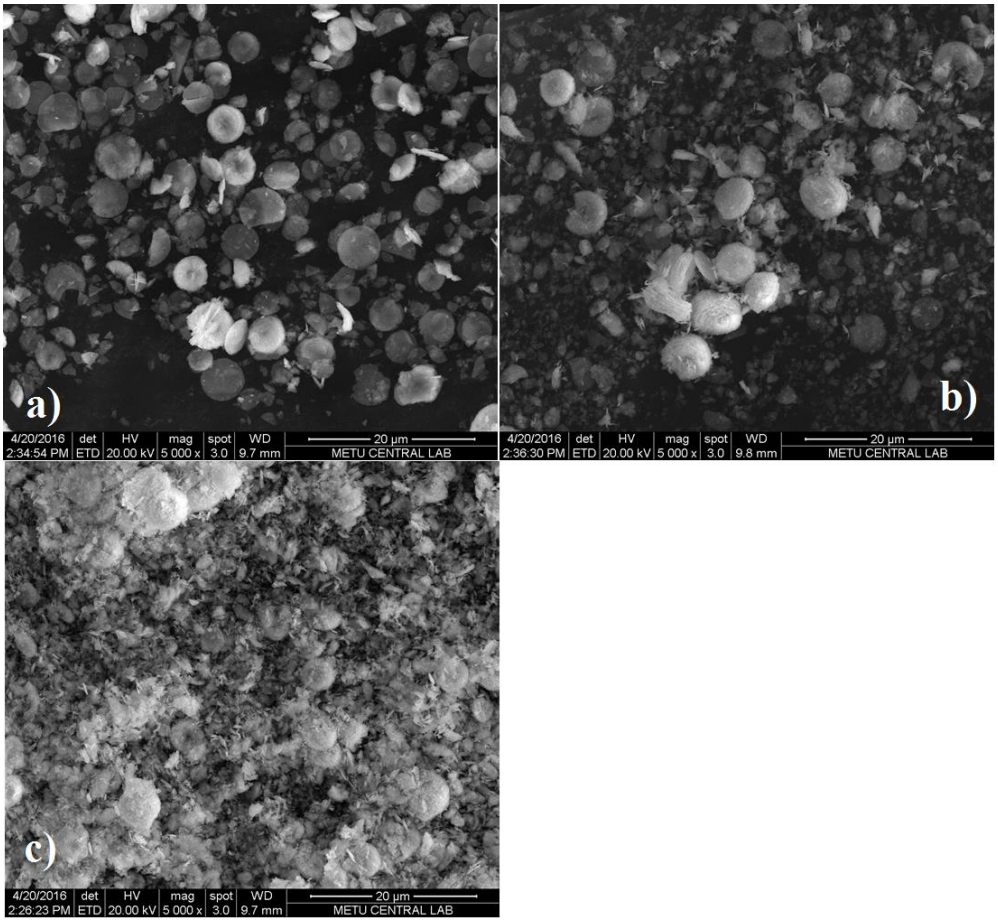

Figure 44. SEM images of a) 7.5% Tb doped $GdBO_3$, b) 10% Tb doped $GdBO_3$, c) 12.5% Tb doped $GdBO_3$.

EDX spectra of Tb doped $GdBO_3$ samples are presented in **Figure 45**. EDX analysis illustrates the presence of Tb and Gd elements in the produced samples.

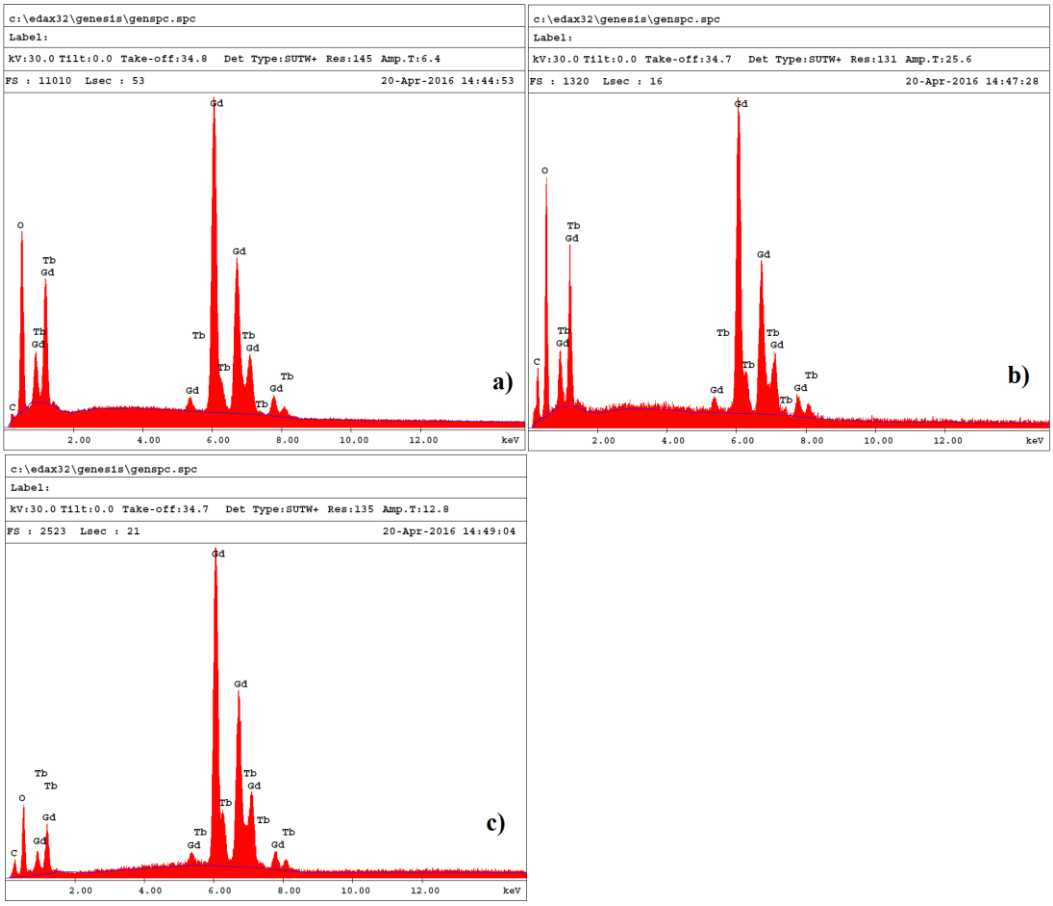

Figure 45. EDX spectra of a) 7.5% Tb doped $GdBO_3$, b) 10% Tb doped $GdBO_3$, c) 12.5% Tb doped $GdBO_3$.

The results obtained from the SEM analysis of the Sm doped $GdBO_3$ samples are shown in **Figure 46**. SEM images indicate that doping with various amount of Sm has led to almost no change in the particles shape and size. It can be seen that particles are formed in the shape of spherical crystals.

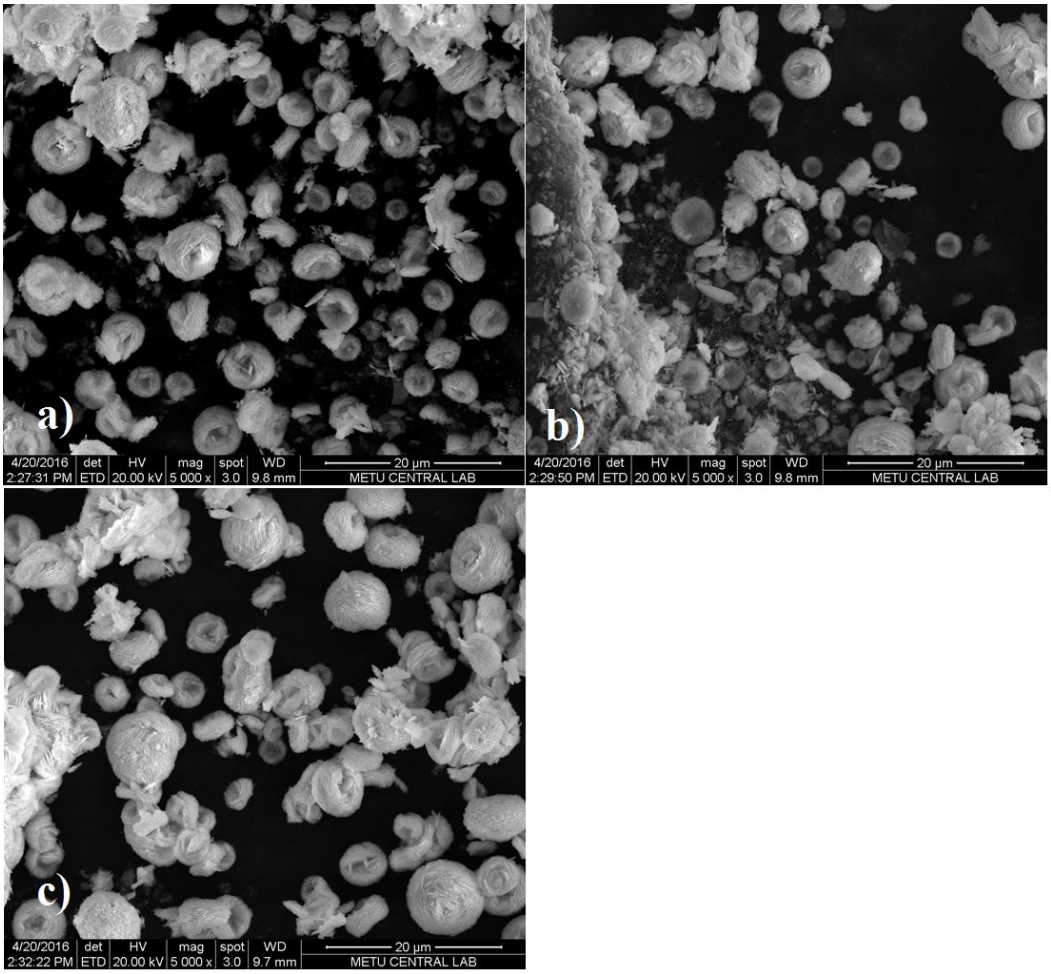

Figure 46. SEM images of a) 2.5% Sm doped $GdBO_3$, b) 5% Sm doped $GdBO_3$, c) 7.5% Sm doped $GdBO_3$.

As illustrated in **Figure 47**, the EDX spectra of Sm doped $GdBO_3$ samples indicate the presence of Sm and Gd elements in the prepared samples.

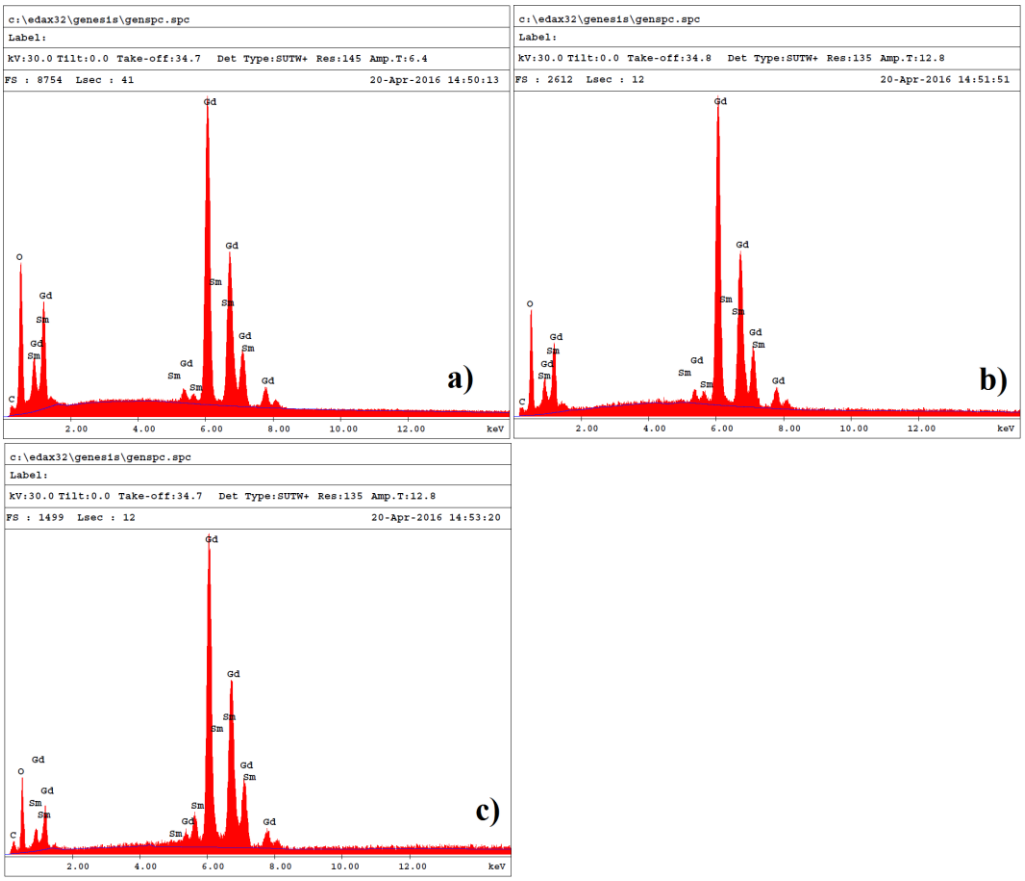

Figure 47. EDX spectra of a) 2.5% Sm doped $GdBO_3$, b) 5% Sm doped $GdBO_3$, c) 7.5% Sm doped $GdBO_3$.

3.5- Photoluminescence analysis

3.5.1 Photoluminescence results of Dy, Tb and Sm doped $LaBO_3$

Photoluminescence emission measurement of Dy^{3+} doped $LaBO_3$ orthoborate in the range of 450-700 nm was recorded by excitation at 351nm. As **Figure 48** illustrates, three simultaneous emission in blue (485 nm), yellow (575 nm) and red (665 nm) can be identified. According to luminescence performance it can inferred that Dy doped $LaBO_3$ is an advantageous candidate to be used in white LED's because it emits in all three main colors. The blue emission is due to $^4F_{9/2} \rightarrow {}^6H_{15/2}$ transition. The yellow emission originates from $^4F_{9/2} \rightarrow {}^6H_{13/2}$ transition and finally the weak emission of red comes from $^4F_{9/2} \rightarrow {}^6H_{11/2}$ transition. As it can be seen, yellow emission dominates the whole emission spectra with its' broad and highly intense peak at 575 nm. The sample

doped with 5% Dy^{3+} has the higher intensity which beyond that concentration luminescence of emitting center quenches. 5 mol% doping has been reported in the literature as the most effective doping concetration in order to get the highest emission intensity. Usually beyond that concentration light emission quenches. Because after 5 mol% doping, the emitted light is absorbed by the other ions of the same kind which are in lower energy levels.

The results of photoluminescence analysis clearly show the dependence ofphotoluminescence performance of Dy doped $LaBO_3$ samples to crystal structure of host lattice. When the crystal structure of the desired host material disappears, luminescence performance is affected adversely. However, there is not a correlation between X-ray diffraction intensity and light emission intensity.

The color of the light emitted from the phosphor is depending on the activator (doped ion). In order to get white light the combination of blue and yellow color is an option therefore our samples with Dy can be a good candidate.

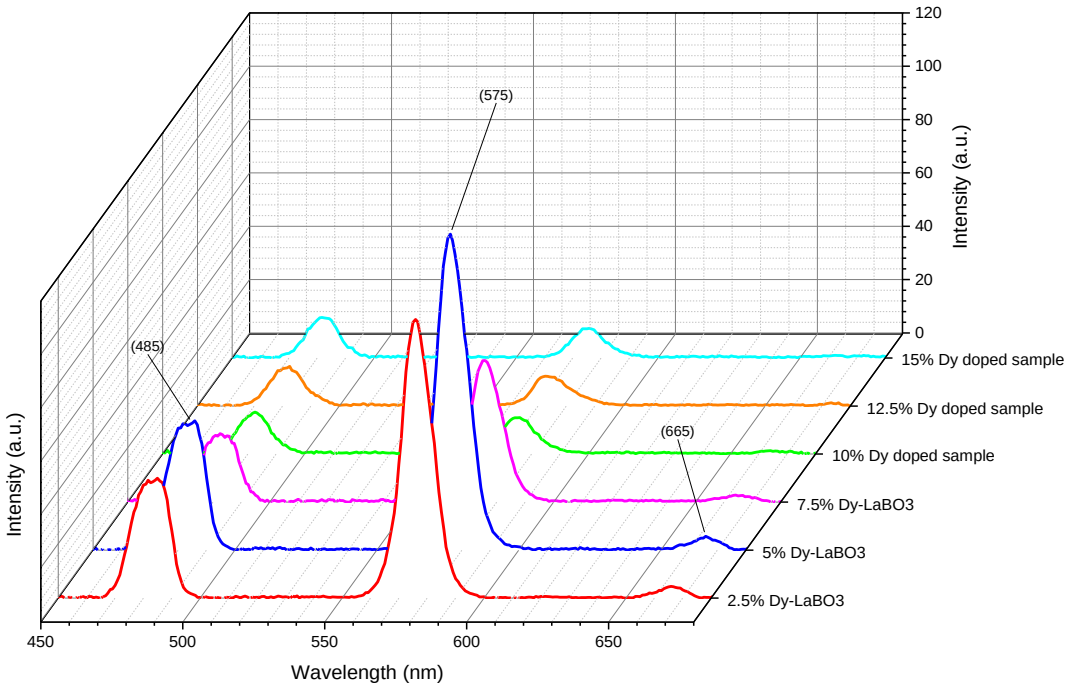

Figure 48. Photoluminescnce measurment of Dy doped $LaBO_3$ samples.

Figure 49 shows the CIE calculation of the 5% Dy doped $LaBO_3$ sample. The chromaticity coordinate of the sample is calculated as x=0.42 and y=0.44 which is located in the yellow region. The CIE calculation of samples doped with various amounts of Dy indicates that the effect of concentration on the light color is not significant. On the other hand concentration effects the intensity of emitted light.

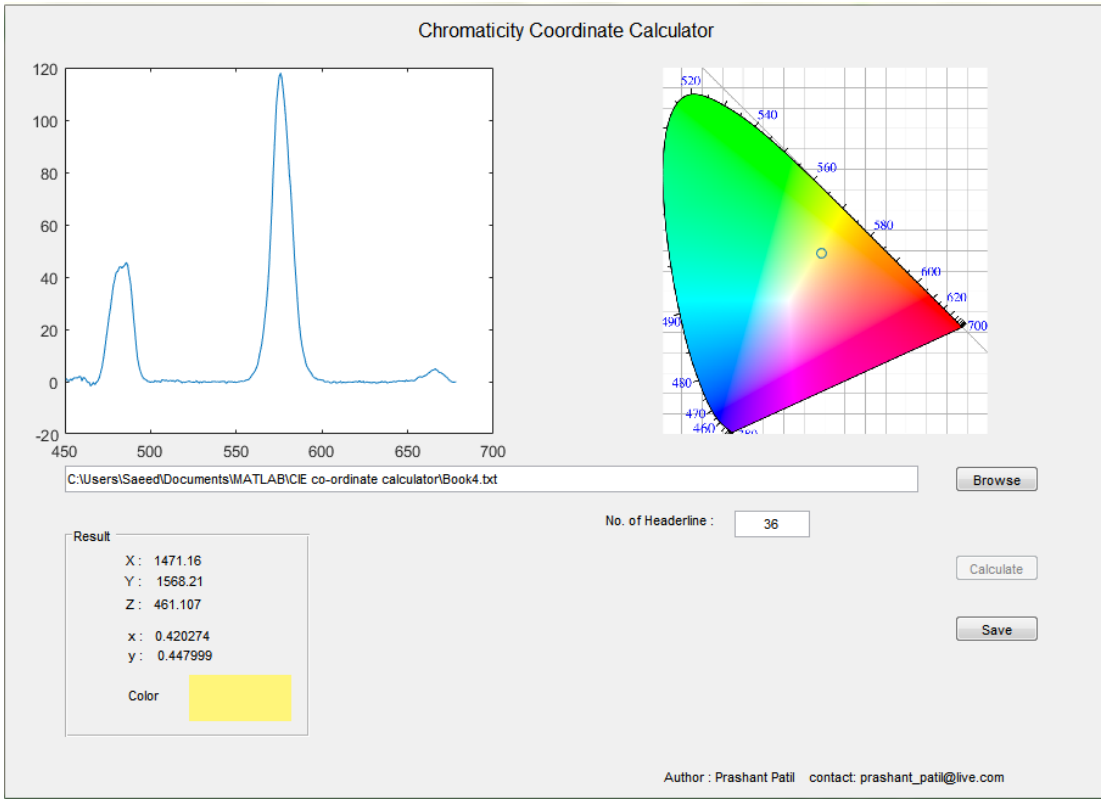

Figure 49. CIE calculation of 5% Dy doped $LaBO_3$ sample.

Figure 50 shows the photoluminescence spectra of Tb doped $LaBO_3$ orthoborates in various concentrations. The samples were excited by near UV light with 378 nm wave length. It can be observed that there are four emission peaks at 489, 544, 587 and 623 nm which can be related to different f-f transition of Tb^{3+} ions. The emissions can be assigned to $^5D_4 \rightarrow {}^7F_6$, $^5D_4 \rightarrow {}^7F_5$, $^5D_4 \rightarrow {}^7F_4$ and $^5D_4 \rightarrow {}^7F_3$ transitions, respectively. The sample with 7 % doped Tb concentration exhibit the best photoluminescence performance. When the concentration of doping exceeds 7%, the structure of samples change substantially. Particularly, borate structure of produced samples undergoes dramatic deformation as it can be observed in IR analysis results. As a result of borate structure deformation, photoluminescence emission of the material affects unfavorably

and its intensity falls. It can be seen that the emission intensity of samples increases by increasing the concentration of Tb up to the formation of impurities.

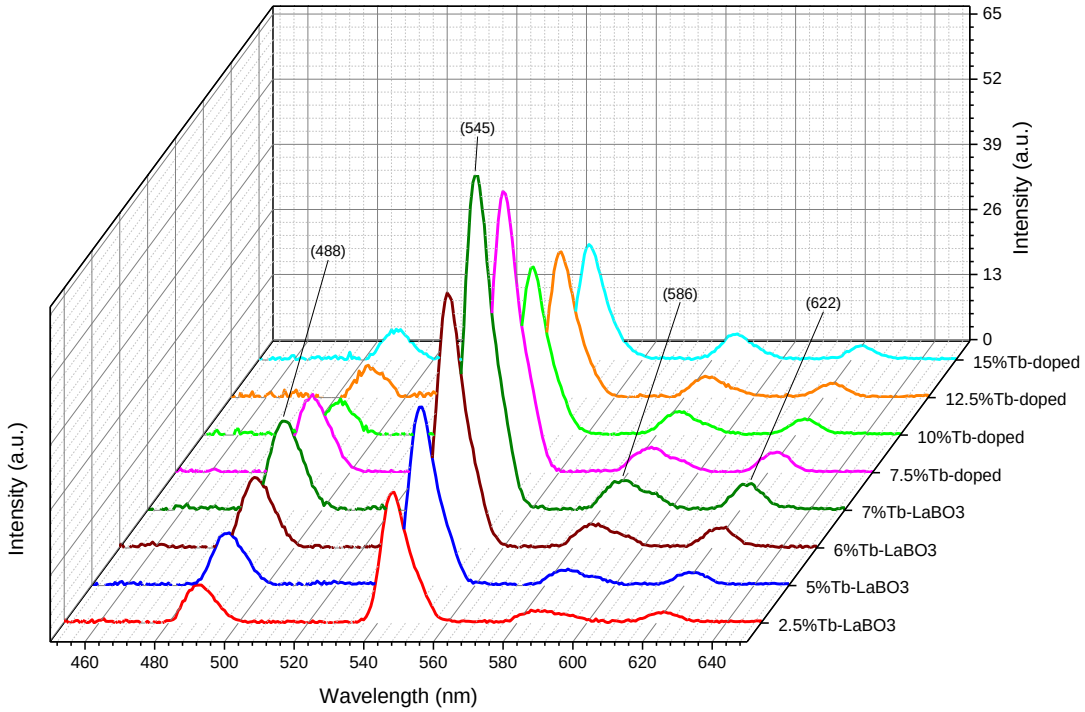

Figure 50. Photoluminescnce measurment of Tb doped $LaBO_3$ samples.

Figure 51 shows the CIE calculation of the 7% Tb doped $LaBO_3$ sample. The chromaticity coordinate of the sample is calculated as x=0.30 and y=0.61 which is located in the green region.

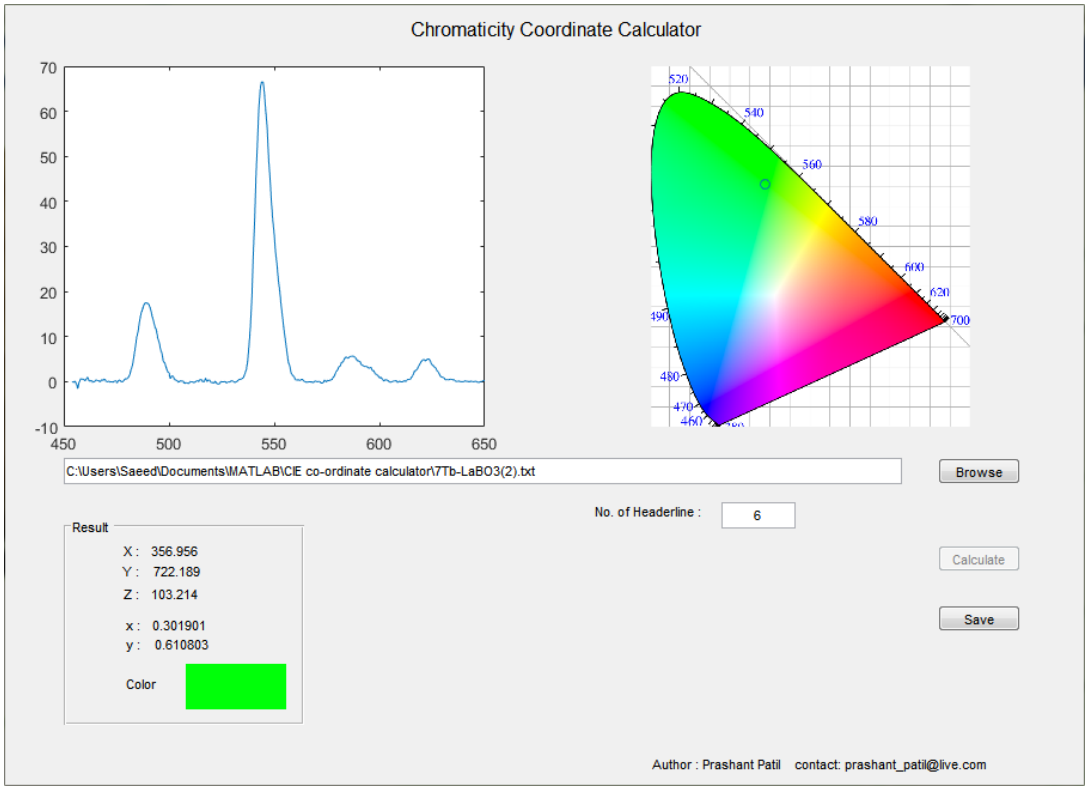

Figure 51. CIE calculation of 7% Tb doped $LaBO_3$ sample.

Figure 52 represents the photoluminescence measurements of Sm doped $LaBO_3$ samples. All the samples were excited by using UV light with 404 nm wavelength. It can be seen that there are three broad and intense emission peaks centered at 565, 601 and 646 nm. These emissions correspond to yellow, orange and red colors, respectively.

f-f transitions of Sm^{3+} are believed to be responsible for above mentioned emissions. The yellow emission is due to $^4G_{5/2} \rightarrow {}^6H_{5/2}$ transition. The orange emission originates from $^4G_{5/2} \rightarrow {}^6H_{7/2}$ transition and finally the broad emission of red comes from $^4G_{5/2} \rightarrow {}^6H_{9/2}$ transition. As it can be seen, orange emission dominates the whole emission spectra with its broad and highly intense peak at 601nm. Investigation of $LaBO_3$ samples doped with various amount of Sm indicates that the sample with 5% Sm has the most strong emission peaks at all transitions. However after 5% doping concentration emission intensity drops sharply.

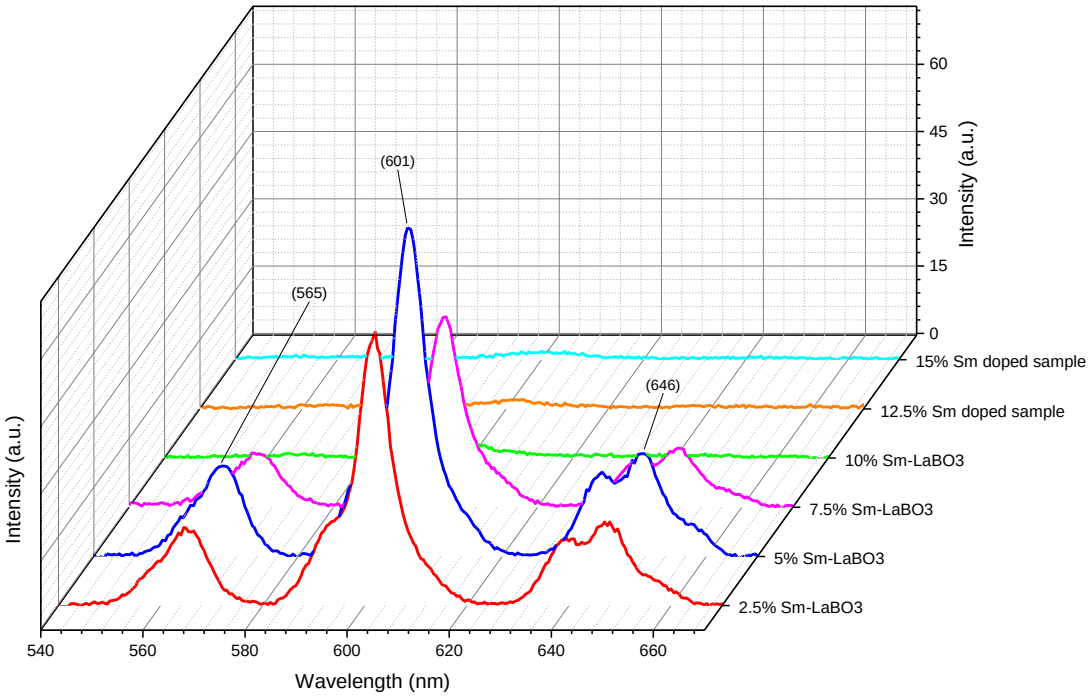

Figure 52. Photoluminescnce measurment of Sm doped $LaBO_3$ samples.

Figure 53 shows the CIE calculation of the 5% Sm doped $GdBO_3$ sample. The chromaticity coordinate of the sample is calculated as x=0.58 and y=0.40 which is located in the orange region.

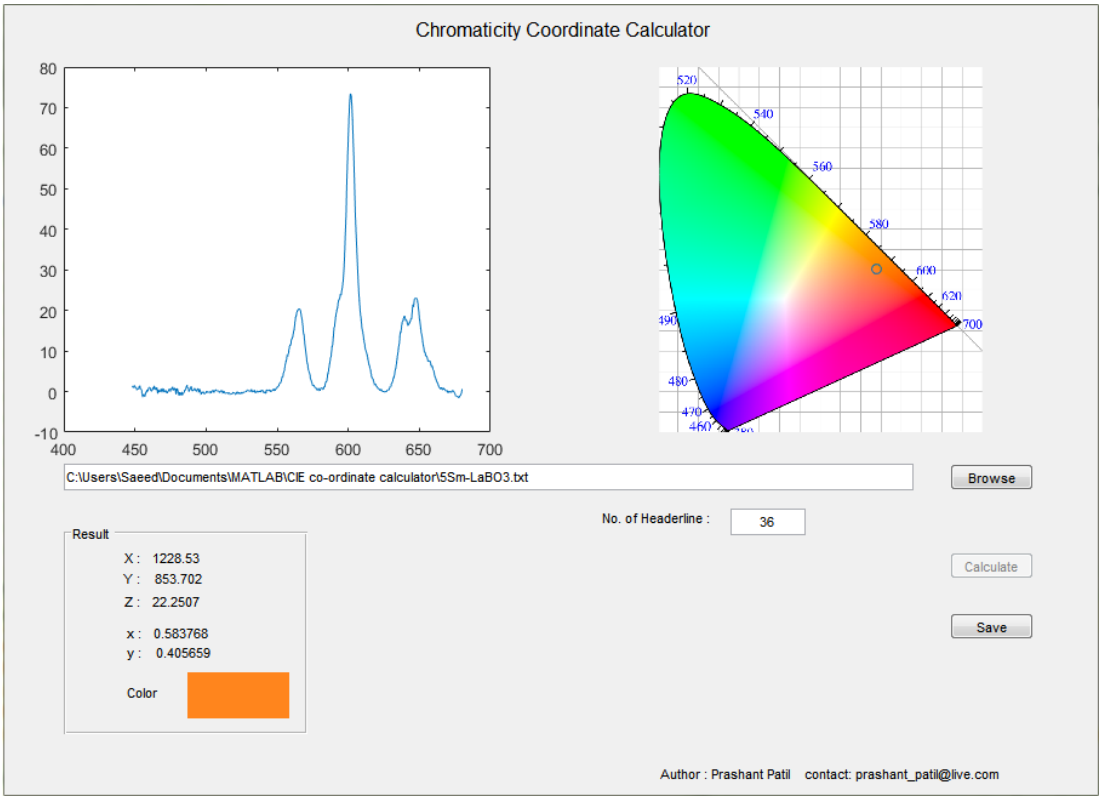

Figure 53. CIE calculation of 5% Sm doped $LaBO_3$ sample.

3.5.2 Photoluminescence results of Dy, Tb and Sm doped $GdBO_3$

Photoluminescence record of Dy doped $GdBO_3$ samples (**Figure 54)** excited at 351nm shows two emission peaks at blue (480 nm) and yellow (578 nm) region. These emissions can be attributed to f-f transitions of Dy^{3+} ions. The emission centered at 480 nm and 578 nm are due to $^4F_{9/2} \rightarrow {}^6H_{15/2}$ and $^4F_{9/2} \rightarrow {}^6H_{13/2}$ transition, respectively. As it can be seen, yellow emission dominates the whole emission spectra with its broad and highly intense peak at 575 nm. The emission originating from $^4F_{9/2} \rightarrow {}^6H_{11/2}$ transition which was well detectable in $LaBO_3$ host is extremely week in $GdBO_3$ host material. The sample doped with 7.5% Dy^{3+} has the highest intensity in whole set. When the concentration of dopant increases to above 7.5%, the intensity of light emission decreases dramatically.

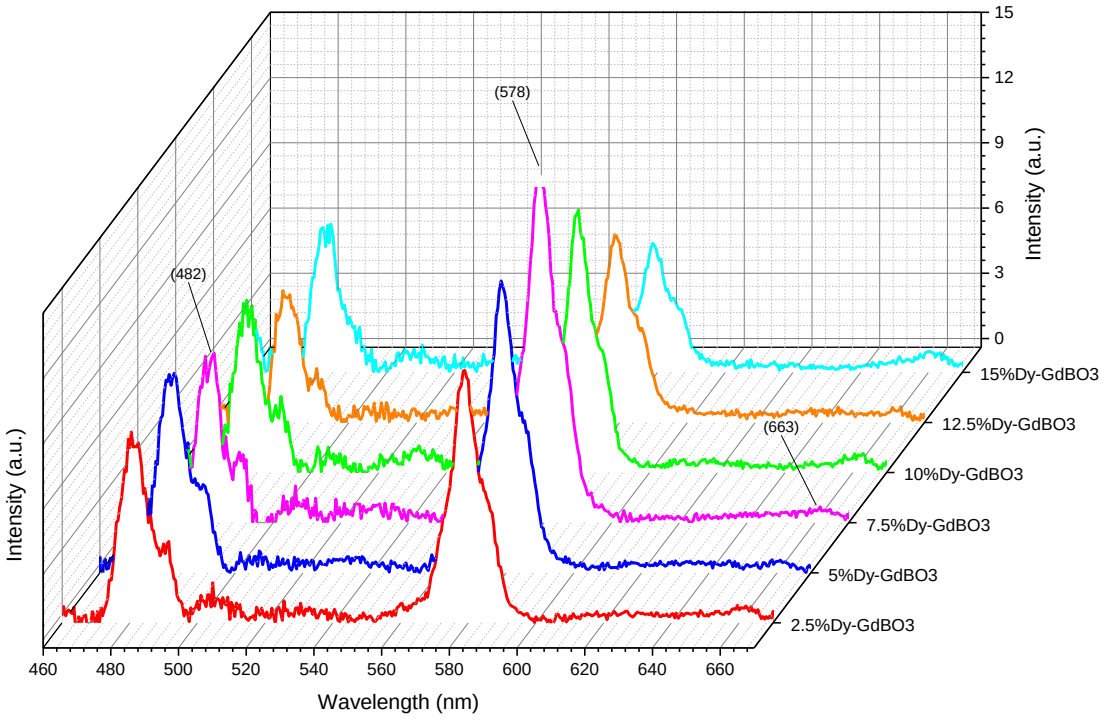

Figure 54. Photoluminescnce measurment of Dy doped $GdBO_3$ samples.

Figure 55 shows the CIE calculation of the 7.5% Dy doped $GdBO_3$ sample. The chromaticity coordinate of the sample is calculated as x=0.44 and y=0.45 which is located in the yellow region.

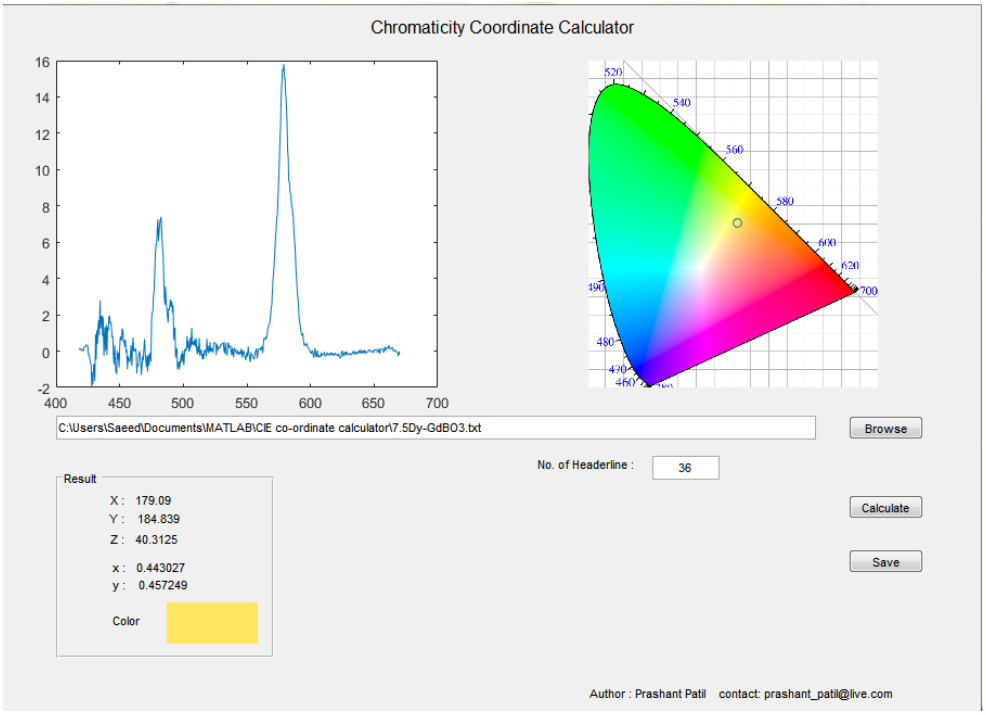

Figure 55. CIE calculation of 7.5% Dy doped $GdBO_3$ sample.

Photoluminescence measurements of Tb doped $GdBO_3$ samples are illustrated in **Figure 56**. As-obtained materials were excited by sing a light with 378 nm wavelength. The spectra resulted from the emission recording of the samples represents typical emission peaks of Tb^{3+} ion which, as were mentioned in the Tb doped $LaBO_3$ section, are originated from the f-f electronic transitions. However there is a point that worth the attention, the intensity of emission peaks of Tb in $GdBO_3$ host is much lower than those with $LaBO_3$ host. It can be observed that there are four emission peaks at 490, 545, 586 and 624 nm which can be assigned to $^5D_4 \rightarrow {}^7F_6$, $^5D_4 \rightarrow {}^7F_5$, $^5D_4 \rightarrow {}^7F_4$ and $^5D_4 \rightarrow {}^7F_3$ transitions, respectively. The sample with 10% doped Tb concentration exhibits the best photoluminescence performance. When the concentration of Tb increases to above 10% luminescent emission of samples decreases.

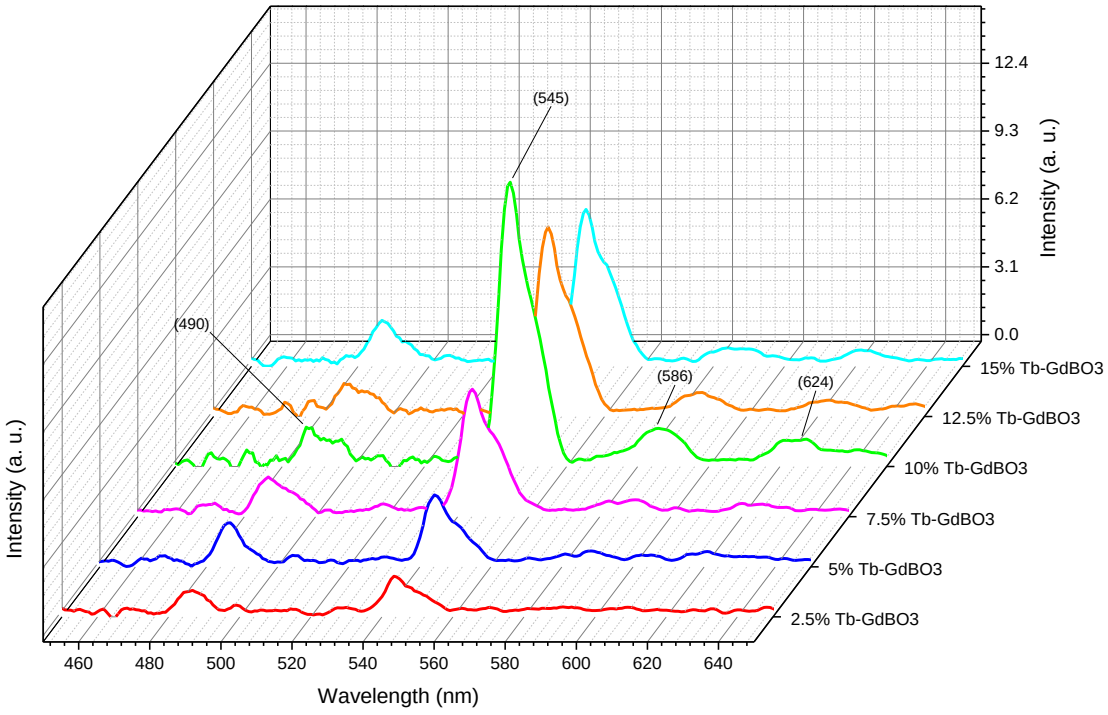

Figure 56. Photoluminescnce measurment of Tb doped $GdBO_3$ samples.

Figure 57 shows the CIE calculation of the 10% Tb doped $GdBO_3$ sample. The chromaticity coordinate of the sample is calculated as x=0.31 and y=0.62 which is located in the green region.

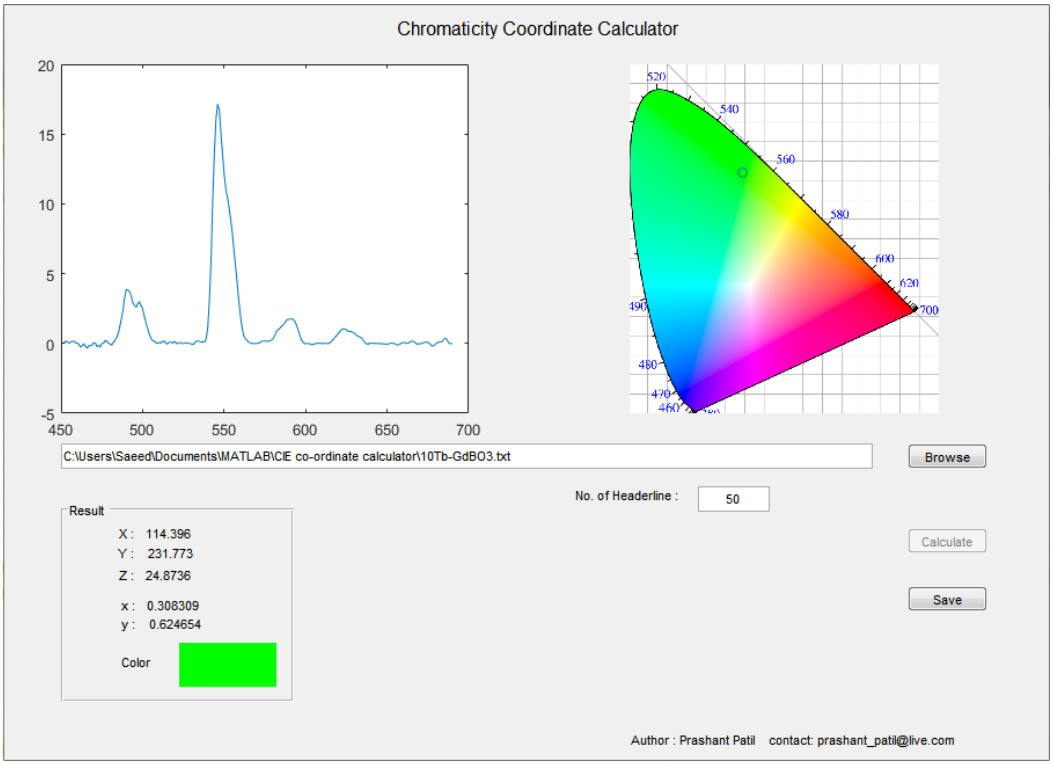

Figure 57. CIE calculation of 10% Tb doped $GdBO_3$ sample.

Figure 58 displays the photoluminescence measurements of $GdBO_3$ host materials doped with various amounts of Sm as emitting activator. The spectra shows that there are three emission peaks at 570, 608 and 654 nm which correspond to yellow, orange and red colors, respectively. All the emission peaks can be related to f-f transitions of Sm^{3+} ions; $^4G_{5/2} \rightarrow {}^6H_{5/2}$, $^4G_{5/2} \rightarrow {}^6H_{7/2}$ and $^4G_{5/2} \rightarrow {}^6H_{9/2}$ transitions give rise to emissions with 570, 608 and 654 nm wavelength, respectively. The investigation of photoluminescence properties of Sm doped $GdBO_3$ samples shows that emission intensity of produced materials are heavily dependent on the concentration of doping.

As shown in **Figure 58**, first the photoluminescence intensity of samples increases as the amount of doping increases reaching its pinnacle at 5%, and then decline with a further increase in the amount of doping. It is well known that the reduction of the emission intensity is due to concentration quenching of emitting centers (i.e. Sm^{3+} ions) .

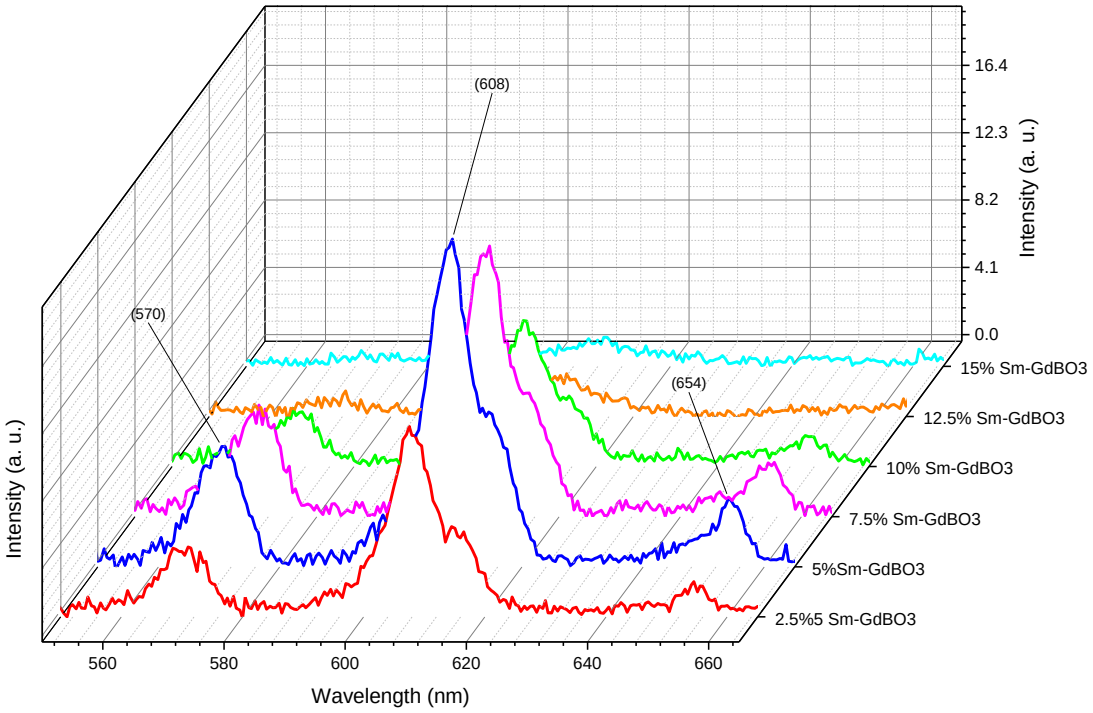

Figure 58. Photoluminescnce measurment of Sm doped $GdBO_3$ samples.

Figure 59 shows the CIE calculation of the 5% Sm doped $GdBO_3$ sample. The chromaticity coordinate of the sample is calculated as x=0.60 and y=0.39 which is located in the orange region.

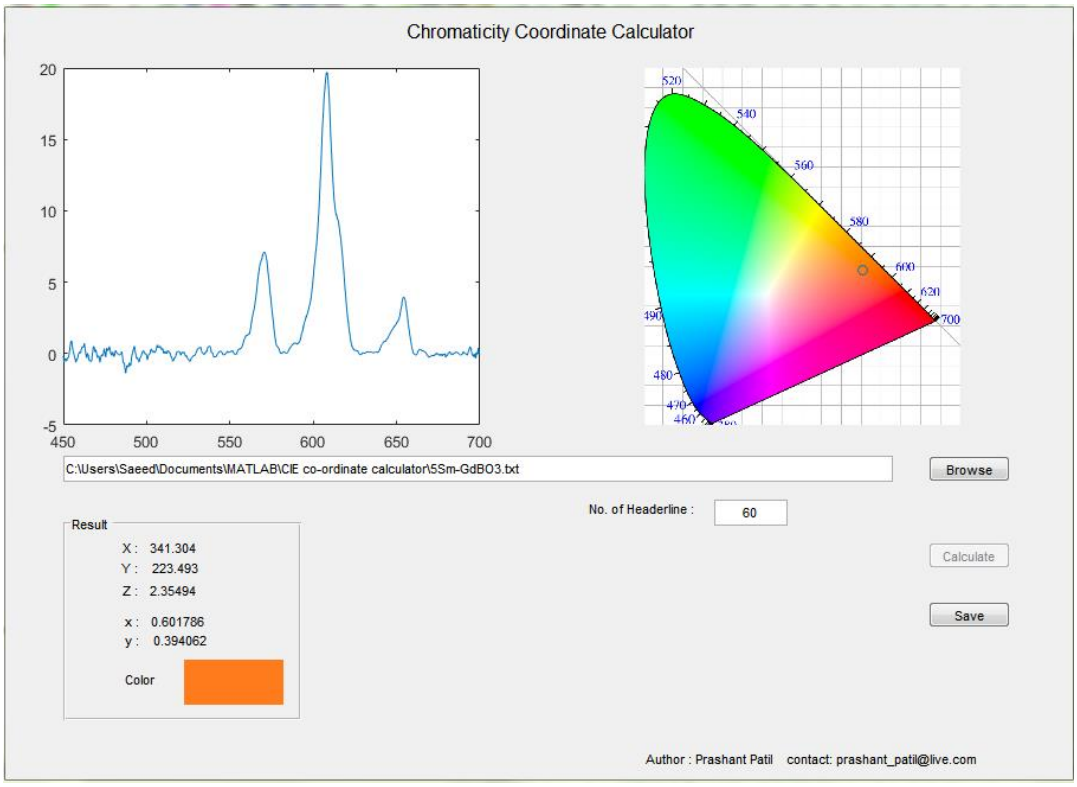

Figure 59. CIE calculation of 5% Sm doped $GdBO_3$ sample.

CHAPTER 4

CONCLUSION

Dy, Tb and Sm doped $LaBO_3$ and $GdBO_3$ orthoborate samples were synthesized successfully by employing hydrothermal synthesis method. When $LaBO_3$ orthoborates were doped with different amount of rare earth elements (i.e. Dy, Tb and Sm), it observed that after certain doping concentration, crystal structure of the host material substantially changes. The critical concentration for doping with Dy is 7.5 mol%, for Tb is 7.5 mol% and for Sm is 12.5 mol%. Unlike $LaBO_3$ when $GdBO_3$ orthoborates doped with Dy, Tb and Sm, the structure of the host material has been preserved largely regardless of the doping concentration.

Based on the IR analysis, is is found that borate structure in $GdBO_3$, $DyBO_3$, $TbBO_3$ and $SmBO_3$ is identical. Borate structure in those compounds consist of tetrahedral BO_4 units which together form $B_3O_9^{9-}$ ring structure. Tetrahedral borate anion has stretching and bending modes with absorption bands at around 1105, 975, 906, 814, 704 and 568 cm^{-1} which makes it detectable by IR analysis.

Borate structure in $LaBO_3$ is quite different from those in $GdBO_3$, $DyBO_3$, $TbBO_3$ and $SmBO_3$. Borates of $LaBO_3$ compound are made up of trigonal planar BO_3^{3-} units and give rise to asymmetric stretching at around 1250 cm^{-1} and symmetric stretching at about 940 cm^{-1} and out-of-plane and in-plane bending vibrational modes at 698 and 610 cm^{-1}, respectively. The difference between the borate structure of the host and dopant material is the main reason of structural disruption when $LaBO_3$ was doped with high concentration of Dy, Tb and Sm.

Far-infrared analysis of prepared samples shows the vibrational modes of metal-oxygen network structure, therefore; it is used to specify whether the doping process occurs in substitutional form or in interstitial form. In the case of Dy, Tb and Sm doped $LaBO_3$, the resemblance of spectrum of undoped and doped in low doping concentrations suggests that the doping takes place substitutionally. However in high doping concentrations, formation of new absorption bands can be an indication of interstitial doping process.

In the case of Dy, Tb and Sm doped $GdBO_3$ samples, there is no remarkable difference between the FAR-IR spectrum of undoped and doped samples which means that the elements have been substitutionally doped.

It is specified that the optimum doping concentration for the best photoluminescence performance for Dy doped $LaBO_3$ samples is 5 mol%. The optimum concentration for Tb and Sm doped $LaBO_3$ samples is 7 mol% and 5 mol%, respectively. In the case of Dy, Tb and Sm doped $GdBO_3$ it is found that doping with 7.5% Dy, 10% Tb and 5% Sm results in most favorable luminescence performance.

By comparing the photoluminescence performance of Dy, Tb and Sm doped $LaBO_3$ with Dy, Tb and Sm doped $GdBO_3$ samples, it is observed that for each of the rare earth doping elements the intensity of light emission from the sample with $LaBO_3$ as the host material is by far superior to the sample with $GdBO_3$ as the host material. It can be concluded that the host lattice which consists of planar BO_3^{3-} borate anions is more favorable for luminescence emission.

According to SEM images of prepared materials it can be understood that by applying hydrothermal synthesis method, the morphology of obtained particles is more homogeneous compared with traditional solid state method. Moreover the shape of produced particles, which are composed of self-assembled micro crystals, is definable from geometric point of view.

CIE calculations show that Dy doped $LaBO_3$ and $GdBO_3$ samples offer overall light emission in yellow region of visible spectrum. Moreover Tb doped $LaBO_3$ and $GdBO_3$

materials exhibit green color based on CIE calculation. Finally Sm doped $LaBO_3$ and $GdBO_3$ samples show orange color.

REFERENCES

[1] M. Lastusaari, T. Laamanen, M. Malkamäki, K. O. Eskola, A. Kotlov, S. Carlson, E. Welter, H. F. Brito, M. Bettinelli, H. Jungner, and J. Hölsä, "The Bologna Stone: history's first persistent luminescent material," *Eur. J. Mineral.*, vol. 24, no. 5, pp. 885–890, Oct. 2012.

[2] W. M. Yen, S. Shionoya, and H. Yamamoto, *Phosphor handbook*, vol. 23, no. 1. 2007.

[3] R. Hilsch, "Alkali-halide phosphors containing heavy metals," *Proc. Phys. Soc.*, vol. 49, no. 4S, pp. 40–45, 1937.

[4] C. R. Ronda, *Luminescence: From Theory to Applications*. Weinheim, Germany: Wiley-VCH Verlag GmbH & Co. KGaA, 2007.

[5] P. Bamfield and P. Bamfield, *Chromic Phenomena*. Cambridge: Royal Society of Chemistry, 2010.

[6] K. N. Shinde, S. J. Dhoble, H. C. Swart, and K. Park, "Phosphate Phosphors for Solid-State Lighting," vol. 174, pp. 41–60, 2012.

[7] J. Ribas Gispert, *Coordination chemistry*. Wiley-VCH, 2008.

[8] J. and L. E. Karl A. Gschneidner, "Handbook on the Physics and Chemistry of Rare Earths (V1 Metals)," *Energy*, vol. 10, pp. 1–894, 1978.

[9] G. H. Dieke, "Spectra and Energy Levels of Rare Earth Ions in Crystals," *Am. J. Phys.*, vol. 38, no. 3, p. 399, 1970.

[10] K. Lemański and P. J. Dereń, "Luminescent properties of dysprosium(III) ions in $LaAlO_3$ nanocrystallites," *J. Rare Earths*, vol. 29, no. 12, pp. 1195–1197,

Dec. 2011.

[11] C. Madhukar Reddy, G. R. Dillip, and B. Deva Prasad Raju, "Spectroscopic and photoluminescence characteristics of Dy^{3+} ions in lead containing sodium fluoroborate glasses for laser materials," *J. Phys. Chem. Solids*, vol. 72, no. 12, pp. 1436–1441, 2011.

[12] I. P. Sahu, P. Chandrakar, R. N. Baghel, D. P. Bisen, N. Brahme, and R. K. Tamrakar, "Luminescence properties of dysprosium doped calcium magnesium silicate phosphor by solid state reaction method," *J. Alloys Compd.*, vol. 649, pp. 1329–1338, Nov. 2015.

[13] G. Bertrand-Chadeyron, M. El-Ghozzi, D. Boyer, R. Mahiou, and J. C. Cousseins, "Orthoborates processed by soft routes: Correlation luminescence structure," *J. Alloys Compd.*, vol. 317–318, pp. 183–185, 2001.

[14] N. Rakov, W. L. B, E. L. Falcão-filho, R. B. Guimarães, G. S. Maciel, and C. B. De Araújo, "Three- and four-photon excited upconversion luminescence in terbium doped lutetium silicate powders by femtosecond laser irradiation," vol. 3, no. 11, pp. 413–419, 2013.

[15] A. J. Silversmith, D. M. Boye, K. S. Brewer, C. E. Gillespie, Y. Lu, and D. L. Campbell, "$^5D_3 \rightarrow {}^7F_J$ emission in terbium-doped sol–gel glasses," *J. Lumin.*, vol. 121, no. 1, pp. 14–20, 2006.

[16] R. Velchuri, B. V. Kumar, V. R. Devi, G. Prasad, D. J. Prakash, and M. Vithal, "Preparation and characterization of rare earth orthoborates, $LnBO_3$ (Ln=Tb, La, Pr, Nd, Sm, Eu, Gd, Dy, Y) and $LaBO_3$:Gd, Tb, Eu by metathesis reaction: ESR of $LaBO_3$:Gd and luminescence of $LaBO_3$:Tb, Eu," *Mater. Res. Bull.*, vol. 46, no. 8, pp. 1219–1226, Aug. 2011.

[17] J. Zmojda, M. Kochanowicz, P. Miluski, and D. Dorosz, "Side-Detecting Optical Fiber Doped with Tb^{3+} for Ultraviolet Sensor Application," *Fibers*, vol. 2, no. 2, pp. 150–157, Apr. 2014.

[18] a K. Bedyal, V. Kumar, O. M. Ntwaeaborwa, and H. C. Swart, "A promising orange-red emitting nanocrystalline $NaCaBO_3:Sm^{3+}$ phosphor for solid state lightning," *Mater. Res. Express*, vol. 1, no. 1, p. 015006, 2014.

[19] Y. Cao, Z. Zhao, J. Yi, C. Ma, D. Zhou, R. Wang, C. Li, and J. Qiu, "Luminescence properties of Sm^{3+}-doped TiO_2 nanoparticles: Synthesis, characterization, and mechanism," *J. Alloys Compd.*, vol. 554, pp. 12–20, 2013.

[20] D. Huang, Y. Zhou, W. Xu, Z. Yang, Z. Liu, M. Hong, Y. Lin, and J. Yu, "Photoluminescence properties of M^{3+} (M^{3+}=Bi^{3+}, Sm^{3+}) activated $Na_5Eu(WO_4)_4$ red-emitting phosphors for white LEDs," *J. Alloys Compd.*, vol. 554, pp. 312–318, 2013.

[21] C. H. R. B. Kistler, C., *Industrial Minerals and Rocks*, 6th ed. Littleton, Colerado: Published by Society for Mining and Metallurgy and Exploration Inc., 1994.

[22] ETİ MADEN, *BOR SEKTÖR RAPORU*. 2013.

[23] E. Fitzer, I. Lefever, N. V. S. A. Bekaert, J. Hubert, S. G. L. C. Gmbh, and G. Chap, "Fibers , 5 . Synthetic Inorganic," 2008.

[24] A. W. Weimer, Ed., *Carbide, Nitride and Boride Materials Synthesis and Processing*. Dordrecht: Springer Netherlands, 1996.

[25] G. S. May and C. J. Spanos, *Fundamentals of semiconductor manufacturing and process control*. IEEE, 2006.

[26] R. S. R. and J. B. M. Ernest M. Levin, "Polymorphism of ABO_3 type rare earth borates," *Am. Mineral.*, vol. 46, no. 1954, pp. 1030–1055, 1961.

[27] Y. Li, J. Zhang, X. Zhang, Y. Luo, S. Lu, X. Ren, X. Wang, L. Sun, and C. Yan, "Luminescent Properties in Relation to Controllable Phase and Morphology of $LuBO_3:Eu^{3+}$ Nano/Microcrystals Synthesized by Hydrothermal Approach," *Chem. Mater.*, vol. 21, no. 3, pp. 468–475, Feb. 2009.

[28] J. P. R. De Villiers, “Crystal structures of aragonite , strontianite , and witherite,” *Am. Mineral.*, vol. 56, pp. 758–767, 1971.

[29] G. Chadeyron, M. El-Ghozzi, R. Mahiou, a Arbus, and J. C. Cousseins, “Revised Structure of the Orthoborate YBO_3,” *J. Solid State Chem.*, vol. 128, no. 128, pp. 261–266, 1997.

[30] J. R. Cox and D. a. Keszler, “$InBO_3$,” *Acta Crystallogr. Sect. C Cryst. Struct. Commun.*, vol. 50, no. 12, pp. 1857–1859, 1994.

[31] H. G. Giesber, J. Ballato, W. T. Pennington, and J. W. Kolis, “Synthesis and characterization of optically nonlinear and light emitting lanthanide borates,” in *Information Sciences*, vol. 149, no. 1–3, pp. 61–68 , 2003.

[32] A. Pitscheider, R. Kaindl, O. Oeckler, and H. Huppertz, “The crystal structure of π-$ErBO_3$: New single-crystal data for an old problem,” *J. Solid State Chem.*, vol. 184, no. 1, pp. 149–153, 2011.

[33] J. Lin, D. Sheptyakov, Y. Wang, and P. Allenspach, “Structures and Phase Transition of Vaterite-Type Rare Earth Orthoborates: A Neutron Diffraction Study,” *Chem. Mater.*, vol. 16, no. 12, pp. 2418–2424, Jun. 2004.

[34] E. Hertel, “Crystal structures, von Ralph W. G. Wyckoff. Interscience Publishers, Inc., New York, 1951. Vol. II. 253 S.,” *Angew. Chemie*, vol. 65, no. 9, pp. 247–247, May 1953.

[35] A. Nakatsuka, O. Ohtaka, H. Arima, N. Nakayama, and T. Mizota, “Aragonite-type lanthanum orthoborate, $LaBO_3$,” *Acta Crystallogr. Sect. E Struct. Reports Online*, vol. 62, no. 4, pp. i103–i105, Mar. 2006.

[36] J. Thakur, D. P. Dutta, H. Bagla, and A. K. Tyagi, “Effect of Host Structure and Concentration on the Luminescence of Eu^{3+} and Tb^{3+} in Borate Phosphors,” *J. Am. Ceram. Soc.*, vol. 95, no. 2, pp. 696–704, Feb. 2012.

[37] G. Jia, C. Zhang, C. Wang, L. Liu, C. Huang, and S. Ding, “Uniform and well-

dispersed $LaBO_3$ hierarchical architectures: synthesis, formation, and luminescence properties," *CrystEngComm*, vol. 14, no. 2, pp. 579–584, Dec. 2012.

[38] S. SEYYİDOĞLU, "SYNTHESIS AND CHARACTERIZATION OF NOVEL RARE EARTH PHOSPHATES AND RIETVELD STRUCTURAL ANALYSIS OF RARE EARTH ORTHOBORATES," Middle East Technical University, 2009.

[39] Z. Leng, Y. Liu, N. Zhang, L. Li, and S. Gan, "Controlled synthesis and luminescent properties of different morphologies $GdBO_3:Eu^{3+}$ phosphors self-assembled of nanoparticles," *Colloids Surfaces A Physicochem. Eng. Asp.*, vol. 472, pp. 109–116, May 2015.

[40] M. Ren, J. H. Lin, Y. Dong, L. Q. Yang, M. Z. Su, and L. P. You, "Structure and Phase Transition of $GdBO_3$," *Chem. Mater.*, vol. 11, no. 6, pp. 1576–1580, Jun. 1999.

[41] C. E. Weir and E. R. Lippincott, "Infrared studies of aragonite, calcite, and vaterite type structures in the borates, carbonates, and nitrates," *J. Res. Natl. Bur. Stand. Sect. A Phys. Chem.*, vol. 65A, no. 3, p. 173, 1961.

[42] Z. Wei and L. Sun, "Size-dependent chromaticity in YBO_3:Eu nanocrystals: Correlation with microstructure and site symmetry," *J. Phys. Chem. B*, vol. 106, no. 41, pp. 10610–10617, 2002.

[43] S. Shi and J. Hwang, "Plasma spray fabrication of near-net-shape ceramic objects," vol. 2, no. 2, pp. 145–150, 2003.

[44] A. C. Pierre, *Introduction to Sol-Gel Processing*, vol. 1. Boston, MA: Springer US, 1998.

[45] C. BADAN, "MICROWAVE ASSISTED SYNTHESIS OF RARE EARTH IONS DOPED LANTHANUM ORTHOBORATE, THEIR CHARACTERIZATIONS AND INVESTIGATIONS OF LUMINESCENCE

PROPERTIES," Middle East Technical University, 2012.

[46] Y. Zeng, Z. Li, Y. Liang, X. Gan, and M. Zheng, "A general approach to spindle-assembled lanthanide borate nanocrystals and their photoluminescence upon Eu^{3+}/Tb^{3+} doping.," *Inorg. Chem.*, vol. 52, no. 16, pp. 9590–6, Aug. 2013.

[47] L. M. Liz-Marzán, "Tailoring surface plasmons through the morphology and assembly of metal nanoparticles," *Langmuir*, vol. 22, no. 1, pp. 32–41, 2006.

[48] Y. Xia, Y. Xiong, B. Lim, and S. E. Skrabalak, "Shape-Controlled Synthesis of Metal Nanocrystals: Simple Chemistry Meets Complex Physics?," *Angew. Chemie Int. Ed.*, vol. 48, no. 1, pp. 60–103, Jan. 2009.

[49] C. R. Bealing, W. J. Baumgardner, J. J. Choi, T. Hanrath, and R. G. Hennig, "Predicting nanocrystal shape through consideration of surface-ligand interactions," *ACS Nano*, vol. 6, no. 3, pp. 2118–2127, 2012.

[50] K. An and T. Hyeon, "Synthesis and biomedical applications of hollow nanostructures," *Nano Today*, vol. 4, no. 4, pp. 359–373, 2009.

[51] Q. He and J. Shi, "Mesoporous silica nanoparticle based nano drug delivery systems: synthesis, controlled drug release and delivery, pharmacokinetics and biocompatibility," *J. Mater. Chem.*, vol. 21, no. 16, p. 5845, 2011.

[52] Y. Xia, P. Yang, Y. Sun, Y. Wu, B. Mayers, B. Gates, Y. Yin, F. Kim, and H. Yan, "One-Dimensional Nanostructures: Synthesis, Characterization, and Applications," *Adv. Mater.*, vol. 15, no. 5, pp. 353–389, 2003.

[53] J. Zhang and J. Lin, "Vaterite-type YBO_3:Eu^{3+} crystals: Hydrothermal synthesis, morphology and photoluminescence properties," *J. Cryst. Growth*, vol. 271, no. 1–2, pp. 207–215, 2004.

[54] X.-C. Jiang, L.-D. Sun, and C.-H. Yan, "Ordered Nanosheet-Based YBO_3:Eu^{3+} Assemblies: Synthesis and Tunable Luminescent Properties," *J. Phys. Chem. B*, vol. 108, no. 11, pp. 3387–3390, 2004.

[55] C. Lin, D. Kong, X. Liu, H. Wang, M. Yu, and J. Lin, “Monodisperse and Core−Shell-Structured SiO2@ YBO_3: Eu^{3+} Spherical Particles: …,” *Inorg. Chem*, vol. 46, no. 7, pp. 2674–2681, 2007.

[56] G. Pan, H. Song, L. Yu, Z. Liu, X. Bai, Y. Lei, and L. Fan, “Luminescent properties of YBO_3:Eu^{3+} nanosheets and microstructural materials consisting of nanounits,” *J. Lumin.*, vol. 122–123, no. 1–2, pp. 882–885, 2007.

[57] F. J. Avella, O. J. Sovers, and C. S. Wiggins, “Rare Earth Cathodoluminescence in $InBO_3$ and Related Orthoborates,” *J. Electrochem. Soc.*, vol. 114, no. 6, p. 613, 1967.

[58] Y. Wang, K. Uheda, H. Takizawa, and T. Endo, “$GdBO_3$:Eu Phosphor Particles with Uniform Size, Plate Morphology, and Non-Aggregation.,” *Chem. Lett.*, no. 3, pp. 206–207, 2001.

[59] J. Hölsä, “Luminescence of Eu^{3+} ion as a structural probe in high temperature phase transformations in lutetium orthoborates,” *Inorganica Chim. Acta*, vol. 139, no. 1–2, pp. 257–259, Dec. 1987.

[60] C. Badan, O. Esenturk, and A. Yılmaz, “Microwave-assisted synthesis of Eu^{3+} doped lanthanum orthoborates, their characterizations and luminescent properties,” *Solid State Sci.*, vol. 14, no. 11, pp. 1710–1716, 2012.

[61] C. Mansuy, J. M. Nedelec, C. Dujardin, and R. Mahiou, “Concentration effect on the scintillation properties of sol-gel derived $LuBO_3$ doped with Eu^{3+} and Tb3+,” *Opt. Mater. (Amst).*, vol. 29, no. 6, pp. 697–702, 2007.

[62] D. Boyer, G. Bertrand-Chadeyron, R. Mahiou, L. Lou, A. Brioude, and J. Mugnier, “Spectral properties of $LuBO_3$ powders and thin films processed by the sol-gel technique,” *Opt. Mater. (Amst).*, vol. 16, no. 1–2, pp. 21–27, 2001.

[63] N. V. Klassen, S. Z. Shmurak, I. M. Shmyt’Ko, G. K. Strukova, S. E. Derenzo, and M. J. Weber, “Structure and luminescence spectra of lutetium and yttrium borates synthesized from ammonium nitrate melt,” in *Nuclear Instruments and*

Methods in Physics Research, Section A: Accelerators, Spectrometers, Detectors and Associated Equipment, 2005, vol. 537, no. 1–2 SPEC. ISS., pp. 144–148.

[64] V. N. Kurlov, N. V. Klassen, A. M. Dodonov, S. Z. Shmurak, G. K. Strukova, I. M. Shmyt'Ko, S. E. Derenzo, and M. J. Weber, "Growth of YAG:Re^{3+} (Re=Ce, Eu)-shaped crystals by the EFG/Stepanov technique," in *Nuclear Instruments and Methods in Physics Research, Section A: Accelerators, Spectrometers, Detectors and Associated Equipment*, 2005, vol. 537, no. 1–2 SPEC. ISS., pp. 197–199.

[65] H. C. Zeng, "Synthesis and self-assembly of complex hollow materials," *J. Mater. Chem.*, vol. 21, no. 21, p. 7511, 2011.

[66] Z. Lu and Y. Yin, "Colloidal nanoparticle clusters: functional materials by design," *Chem. Soc. Rev.*, vol. 41, no. 21, p. 6874, 2012.

[67] Q. Zhang, S.-J. Liu, and S.-H. Yu, "Recent advances in oriented attachment growth and synthesis of functional materials: concept, evidence, mechanism, and future," *J. Mater. Chem.*, vol. 19, no. 2, p. 191, 2009.

[68] E. Bash, *Solid State Chemistry, an introduction*, vol. 1. CRC Press, 2015.

[69] M. Subramanian, "STANDARD OPERATING PROCEDURE: Use of Autoclaves for Hydrothermal Experiments," *Oregon State University*, 2011. [Online]. Available: http://chemsafety.chem.oregonstate.edu/content/osp-autoclave-hydrothermal-experiments.

[70] W. D. Wright, "A re-determination of the trichromatic coefficients of the spectral colours," *Trans. Opt. Soc.*, vol. 30, no. 4, pp. 141–164, Mar. 1929.

[71] J. Guild, "The Colorimetric Properties of the Spectrum," *Philos. Trans. R. Soc. A Math. Phys. Eng. Sci.*, vol. 230, no. 681–693, pp. 149–187, Jan. 1932.

[72] R. Nave, "The C.I.E. Color Space," *Georgia State University*, 2016. [Online].

Available: http://hyperphysics.phy-astr.gsu.edu/hbase/vision/cie.html.

APPENDICES

APPENDIX A

Far infrared spectroscopy of La_2O_3 and Gd_2O_3

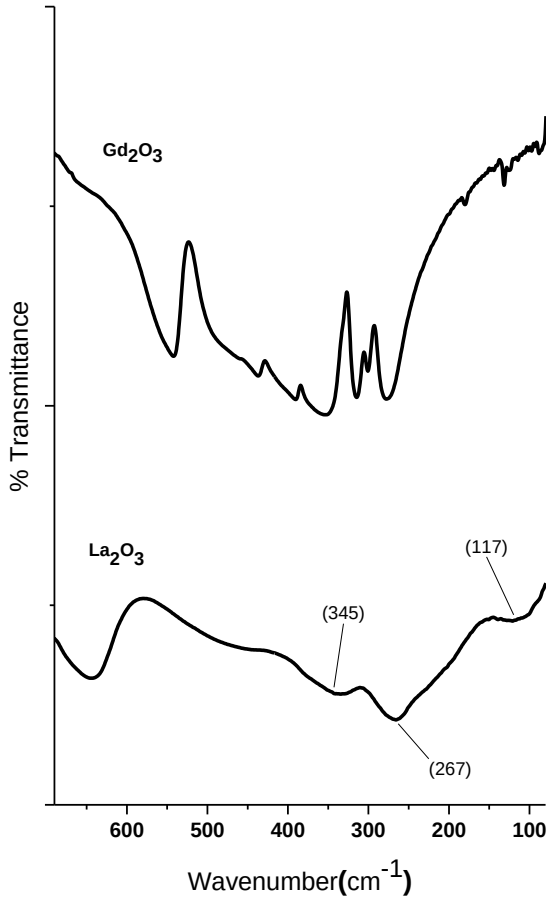

APPENDIX B

XRD results of samples doped with Dy, Tb and Sm in high concentration

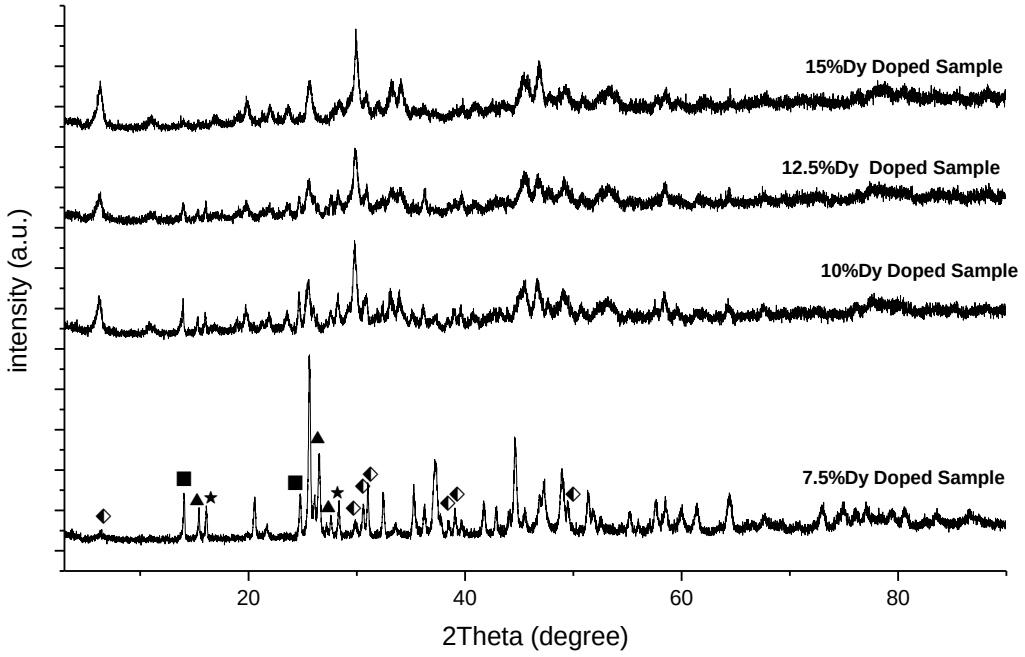

▲: $DyCl_3$ (JCPDS card no: 35-1416), ■: $LaCl_3$ (JCPDS card no: 12-0605)

★: $La(OH)_3$ (JCPDS card no:36-1481), ⬖: unidentified peaks

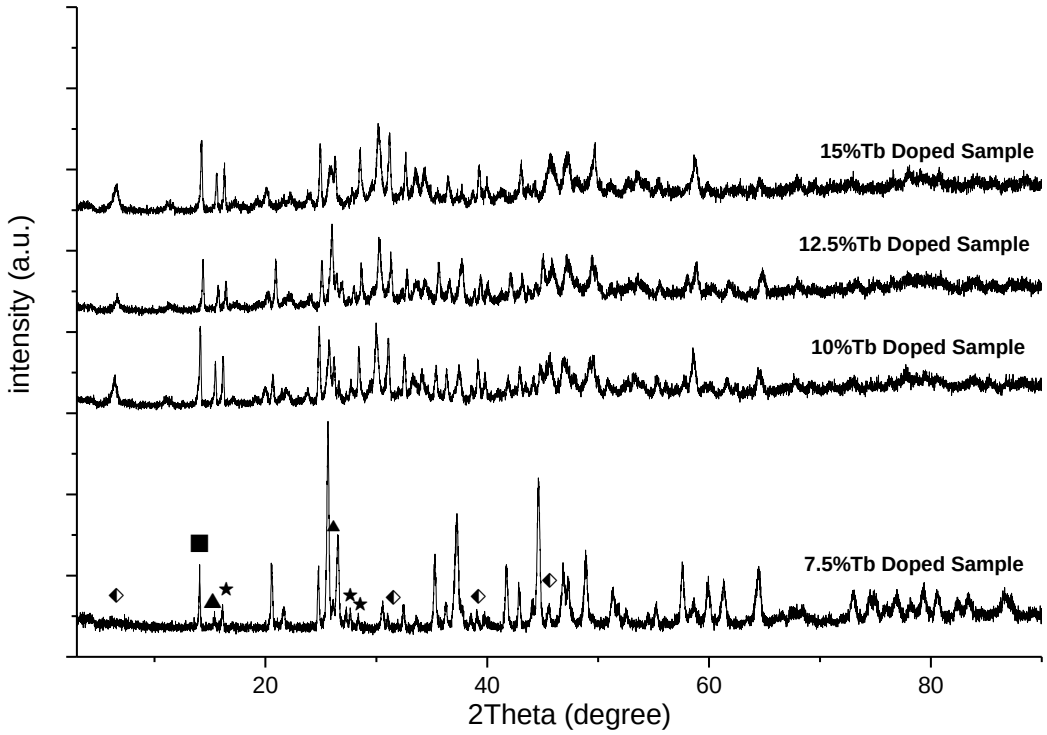

▲: $TbCl_3$ (JCPDS card no: 88-1819), ■: $LaCl_3$ (JCPDS card no: 12-0605)

★: $La(OH)_3$ (JCPDS card no: 36-1481)

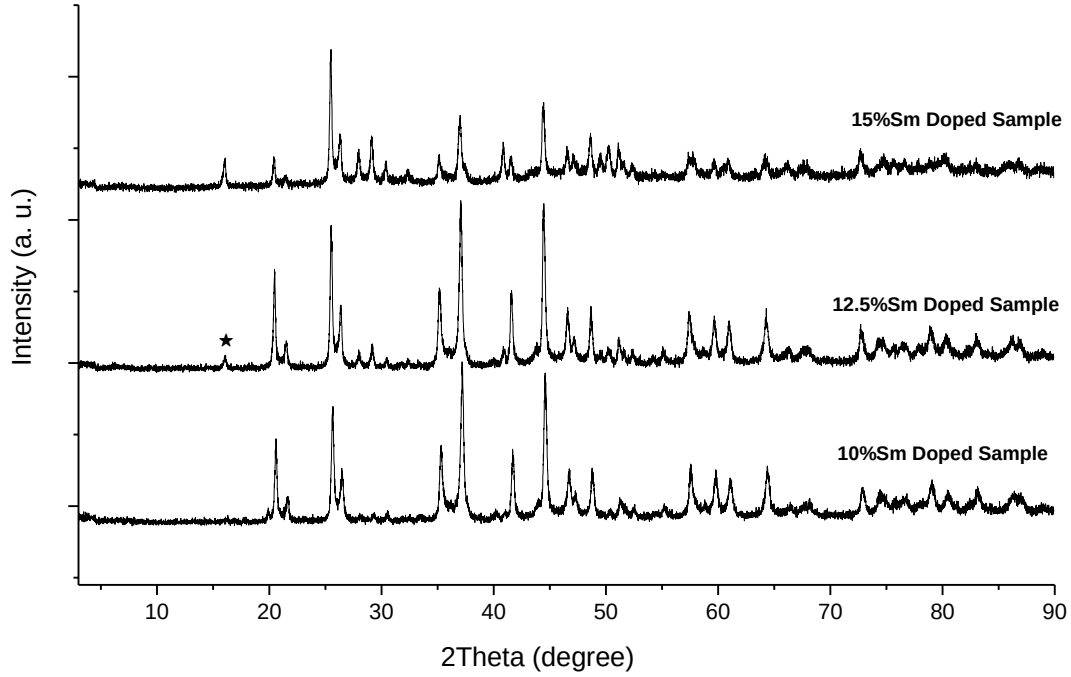

★: $La(OH)_3$ (JCPDS card no: 36-1481)

APPENDIX C

Dy doped $LaBO_3$

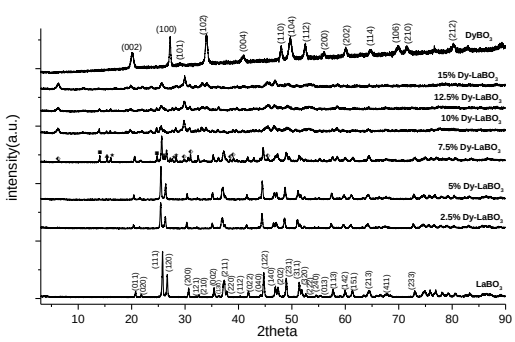

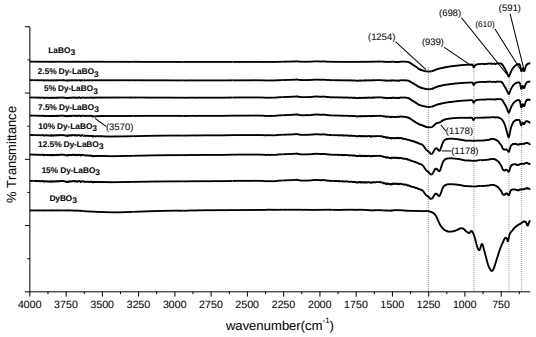

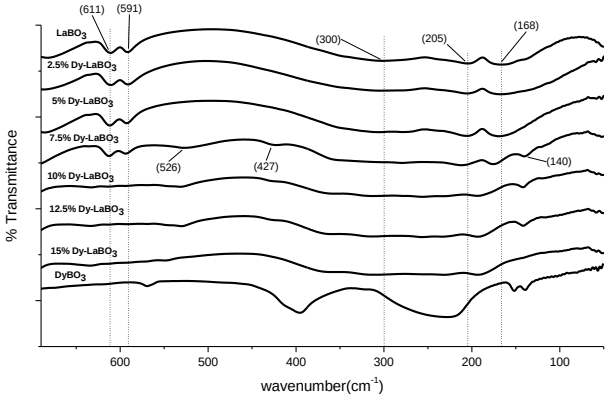

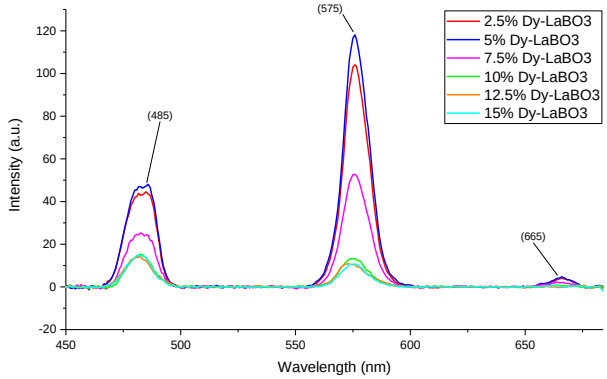

Tb doped $LaBO_3$

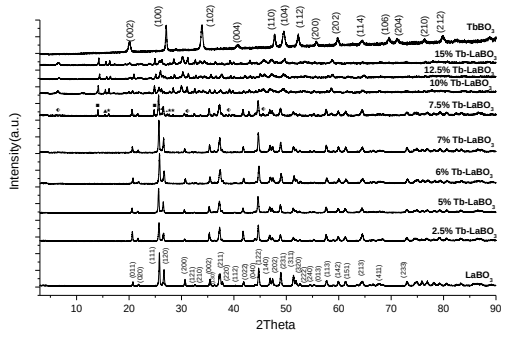

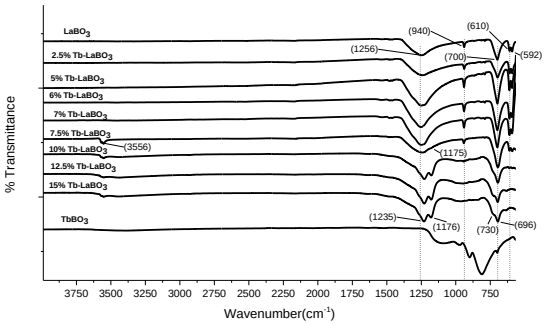

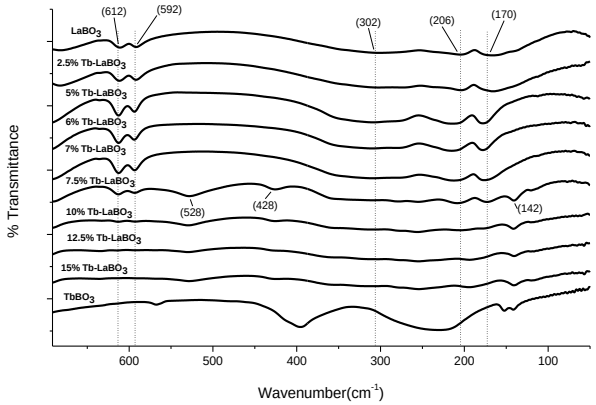

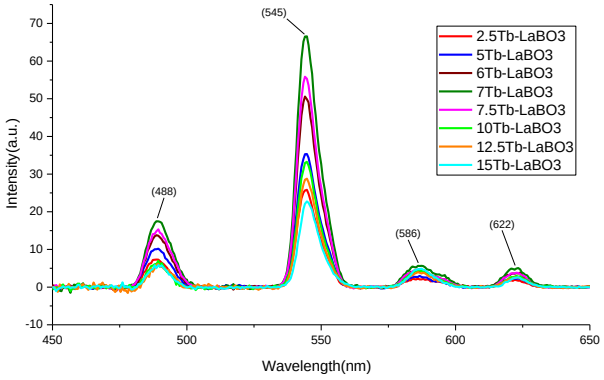

Sm doped $LaBO_3$

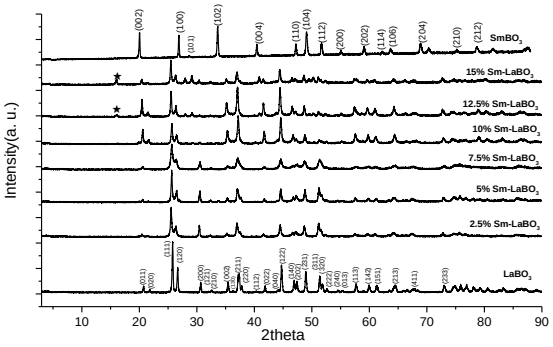

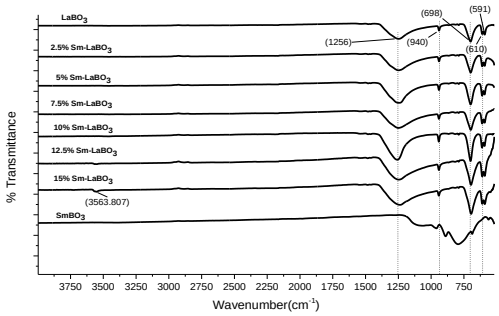

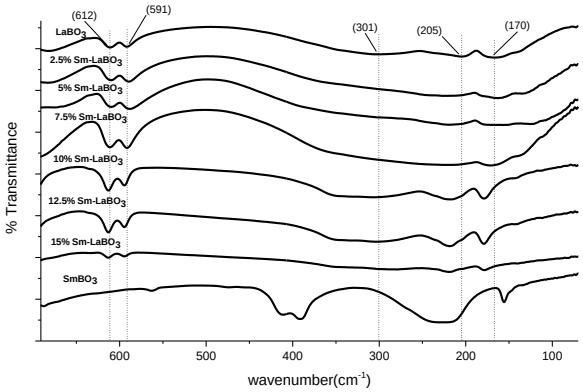

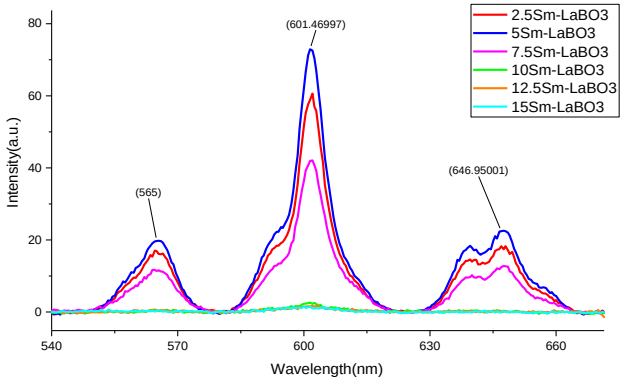

Dy doped $GdBO_3$

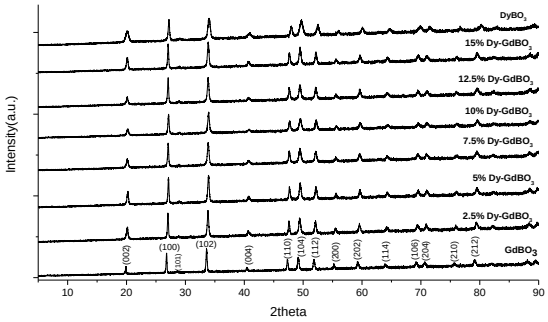

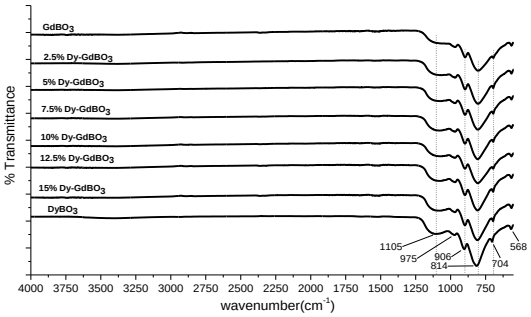

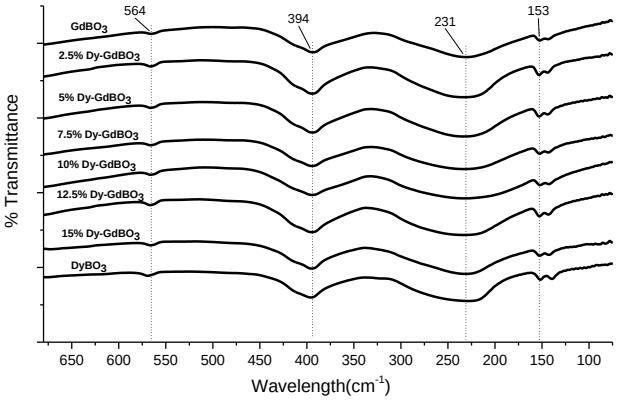

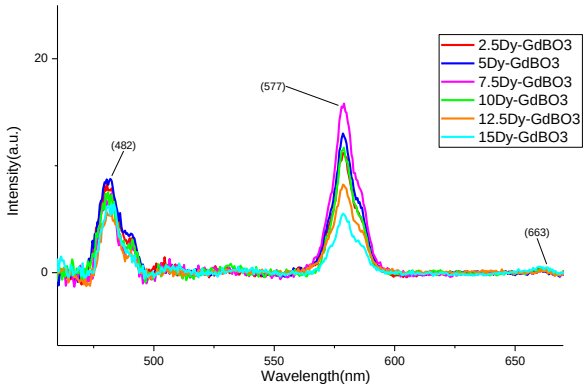

Tb doped $GdBO_3$

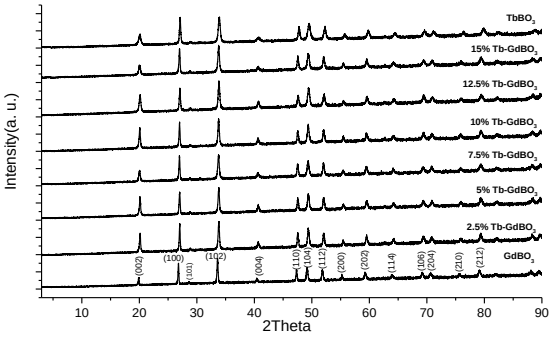

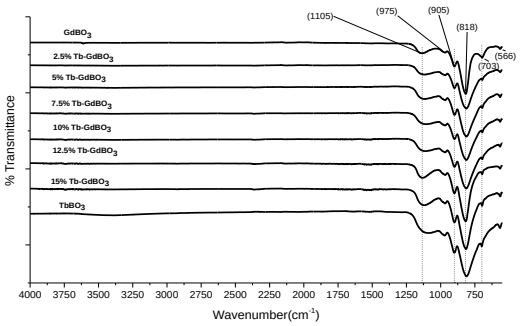

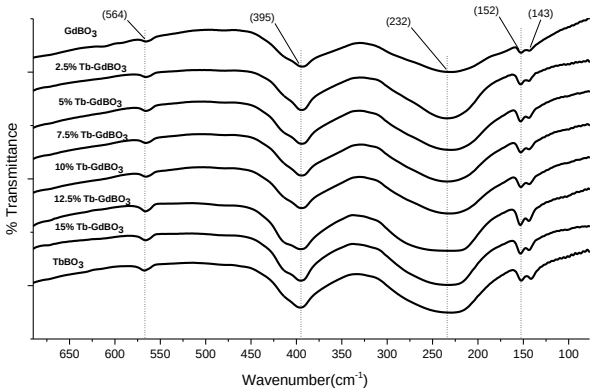

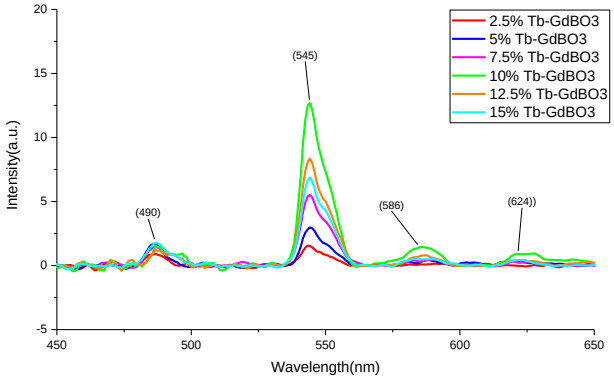

Sm doped $GdBO_3$